Title

The effect of dipole model misspecification on the bias and variance of evoked potential amplitude and amplitude ratio estimate

Author

Cardenas, Valerie A.

Publication Date

1994

Peer reviewed|Thesis/dissertation

The Effect of Dipole Model Misspecification on the Bias and Variance of Evoked Potential Amplitude and Amplitude Ratio Estimates

by

Valerie A. Cardenas

DISSERTATION

Submitted in partial satisfaction of the requirements for the degree of

DOCTOR OF PHILOSOPHY

in

Bioengineering

in the

GRADUATE DIVISION

of the

UNIVERSITY OF CALIFORNIA

San Francisco

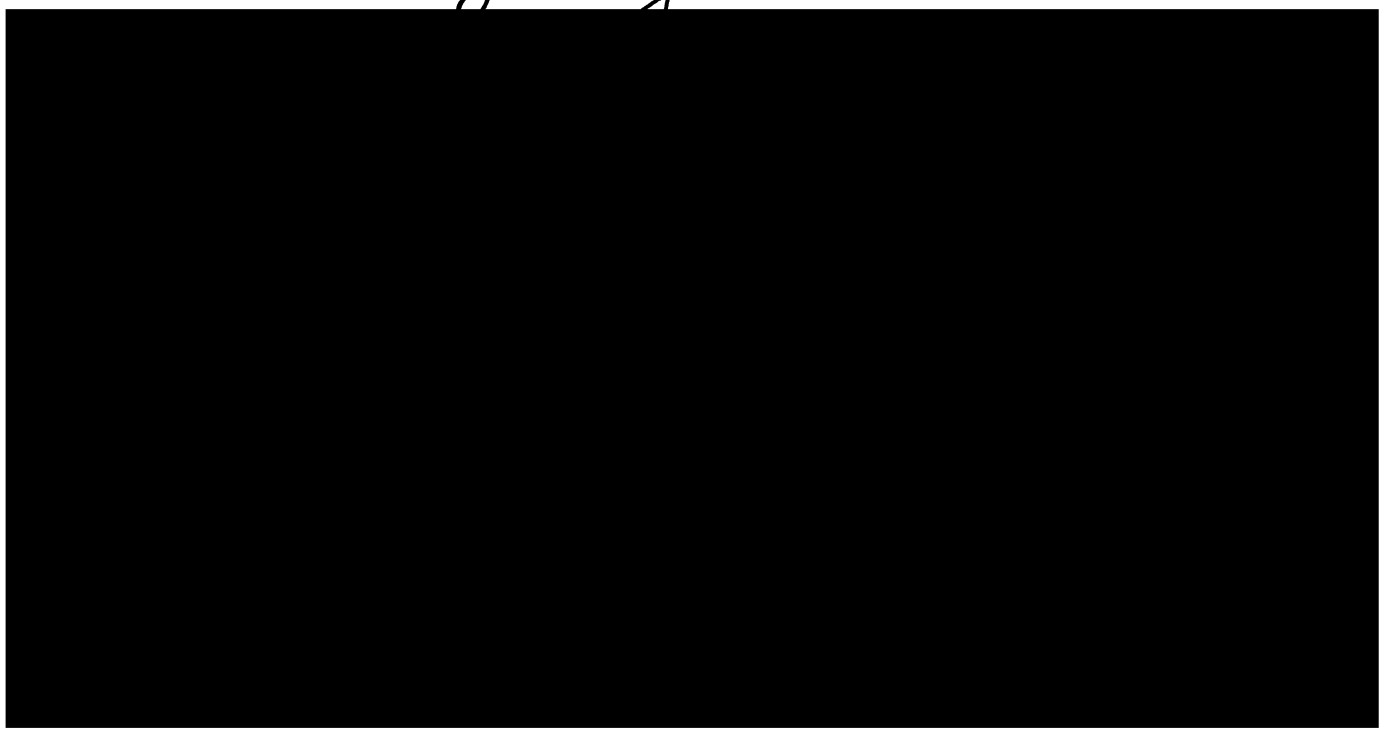

For my parents Cesar and Patricia Cardenas
and husband Edward Nicolson

Preface

This dissertation is the result of a long course of study and research in the Ph.D. program of the Joint Graduate Group in Bioengineering at the University of California, San Francisco and Berkeley. The Bioengineering Joint Graduate Group is a collection of faculty members with primary appointments in engineering or the biological sciences, who advise and guide the graduate careers of students like me– students interested in applying their engineering expertise to problems in biology and medicine.

The co-chairmen of my dissertation committee, Dr. Charles Yingling and Dr. Don Jewett, are both members of the Bioengineering Graduate Group and are deserving of special thanks. Chuck got me "hooked" on evoked potentials, guided me through my qualifying exam, and has provided much assistance with the physiological aspects and interpretations of this work. DJ provided financial support for two years, provided the computer resources of Abratech Corporation, and has always been a careful and critical reader of my work. I would also like to thank the two other readers of my dissertation, Dr. George Fein and Dr. Edward Keller. George provided financial support, an office, and computer resources while I completed my dissertation, and has provided expert guidance and support during all phases of this research. The Dipole Components Model (DCM) was developed in George's laboratory, and he not only suggested the experiment described in Chapter 2, but he also provided me with working DCM software and the auditory P50 data so that I could complete the research in a timely fashion. Ed was the engineer on my committee, and I appreciated his expertise and constructive criticism. Dr. Jack Gerson was a non-reading dissertation committee member. Jack provided invaluable statistical advice, and taught me all I know about simulated annealing.

Several other people made contributions to this work. I would like to thank Dr. Zhi Zhang and Dr. Avner Amir of Abratech Corporation for many helpful discussions. John helped me work through the ideas that became Chapter 3, and Avner encouraged me to pursue a model-free amplitude estimation method, which became Chapter 5. I bounced ideas off of Dan Fletcher for two years while we shared

an office at Abratech Corporation. A fellow graduate student in bioengineering, Dan provided the skull shape weights used in Chapter 4, and I thank him for all his help and advice. I thank Dr. Christie Biggins for peak-picking the auditory P50 data in Chapter 2. I also thank Margie Harrington, a fellow graduate student, former office mate, and friend who knows the evoked potential literature better than anyone I know, for always giving me papers that I should read. Dr. Jonathan Raz taught me time-series analysis from a statistical point of view, and helped me understand the consequences of using a small noise data set to create simulated averages (see Chapter 4). I am grateful for all his advice. My parents and family have always cheered for me, and their support gave me the determination to finish my Ph.D.

Last, but not least, I am deeply grateful for the support and encouragement given me throughout this process by my husband, Edward Nicolson. A fellow Ph.D. student in electrical engineering, we have endured many of the same trials and enjoyed many of the same triumphs during our graduate careers. I thank him for the gift of his patience and understanding.

The Effect of Dipole Model Misspecification on the Bias and Variance of Evoked Potential Amplitude and Amplitude Ratio Estimates

Valerie A. Cardenas

Abstract

In dipole modeling, the generators of evoked potentials (EPs) are modeled as dipoles inside a misspecified model of the head. Most research studies EP changes as a function of stimulus characteristics, disease states, or other differences between data sets. The Dipole Components Model (DCM) is a dipole modeling algorithm that can be applied to multiple data sets gathered under different experimental conditions, and can be used to estimate effects on the amplitude of the equivalent generators (amplitude estimates).

The DCM was applied to auditory evoked P50 EPs for comparison of the reliability (measured by the intraclass correlation coefficient) of P50 suppression estimated using dipole modeling vs. peak-picking. The DCM fit P50 using a homogeneous sphere head model, a decaying sinusoid magnitude function, and a single dipole. Conditioning and testing amplitude parameters were fit, and P50 suppression was measured by dividing the testing amplitude by the conditioning amplitude (amplitude ratio). The DCM improved amplitude ratio but not amplitude reliability over peak-picking, an apparent paradox. It was proposed that the estimation of amplitude and amplitude ratios might be differentially affected in a noisy, misspecified dipole model.

Using the theory of linear least squares fitting, it was shown that dipole model misspecification led to biased amplitudes and unbiased amplitude ratios for three generator cases: (1) single dipole, (2) equal amplitude multiple dipoles, and (3) multiple dipoles with equal amplitude ratios across data sets. The variance of amplitudes and amplitude ratios could not be shown theoretically, so P50 was simulated by generating potentials due to dipoles in a boundary element skull model and adding

EEG noise. Modeling of the simulated P50 using a homogeneous sphere showed that model misspecification and noise led to more variation in amplitude estimates than derived amplitude ratios.

It was proposed that improved amplitude estimation might be achieved by discarding the model. A model-free amplitude estimation method using singular value decomposition (SVD) was developed and tested using simulated and real P50 data. The SVD method estimated reliable amplitudes and ratios when the data were generated by one of the three cases above.

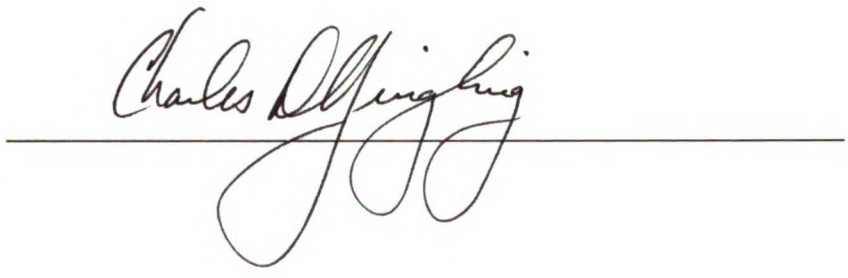

Contents

List of Tables x

List of Figures xi

Glossary of Abbreviations and Symbols xii

1 Introduction 1
- 1.1 Evoked Potentials . . . 6
- 1.2 Neural Generators of Evoked Potentials . . . 8
- 1.3 Dipole Modeling . . . 10
  - 1.3.1 Describing Equation . . . 11
  - 1.3.2 Linear Solutions . . . 15
  - 1.3.3 Nonlinear Solutions . . . 19
  - 1.3.4 Estimation of Covariate Effects . . . 25
- 1.4 Intraclass Correlation Coefficient . . . 30
- 1.5 Summary . . . 32

2 The Reliability of Auditory P50 Suppression as Measured by the Conditioning-Testing Ratio is Improved by Dipole Modeling 34
- 2.1 Introduction . . . 34
- 2.2 Theory . . . 37
  - 2.2.1 Analytic . . . 37
  - 2.2.2 Simulation . . . 38
- 2.3 Methods . . . 39
  - 2.3.1 Overview . . . 39
  - 2.3.2 Subjects . . . 39
  - 2.3.3 Recording Methods . . . 39
  - 2.3.4 Auditory Stimulation . . . 40
  - 2.3.5 EP Waveform Analysis-Peak Picking . . . 41
  - 2.3.6 EP Waveform Analysis-Dipole Modeling . . . 43
  - 2.3.7 EP Waveform Analysis-Decaying Sinusoid Modeling . . . 44
- 2.4 Results . . . 45

2.5 Discussion 50

3 Theoretical considerations **55**
3.1 Introduction 55
3.2 Proofs 57
3.2.1 Single time point, single dipole 57
3.2.2 Multiple time points, single dipole 61
3.2.3 Misspecification of number of dipoles 65
3.2.4 Multiple dipoles 69
3.2.5 Reliability 73

4 Simulations **80**
4.1 Introduction 80
4.2 Methods 82
4.3 Results 98
4.4 Discussion 107

5 Using Singular Value Decomposition for Amplitude and Amplitude Ratio Estimation **116**
5.1 Singular Value Decomposition 117
5.2 The SVD Method 118
5.3 Application to Simulated Data 121
5.4 Application to Real P50 Data 128
5.5 Discussion 130

6 Summary and Conclusions **135**

Bibliography **140**

List of Tables

1.1 Analysis of variance for a reliability model 32

4.1 Simulated Neural Generators 83
4.2 Electrode Locations 83
4.3 Electrode Locations: locations adjusted for skull shape 84
4.4 Data Sets Simulated 86
4.5 Combinations of SNR and C-T ratio for the Data Sets Simulated . . 88
4.6 Data Set 1, Generator 1 99
4.7 Data Set 2, Generator 3 100
4.8 Data Set 3, Generator 5 100
4.9 Data Set 4, Generators 1 and 2 modeled by a single dipole 101
4.10 Data Set 5, Generators 3 and 4 modeled by a single dipole 101
4.11 Data Set 6, Generators 5 and 6 modeled by a single dipole 102
4.12 Data Set 4, Generators 1 and 2 modeled by two dipoles 103
4.13 Data Set 5, Generators 3 and 4 modeled by two dipoles 104
4.14 Data Set 6, Generators 5 and 6 modeled by two dipoles 105

5.1 Data Set 1, Generator 1 analyzed by the SVD Method 123
5.2 Data Set 2, Generator 3 analyzed by the SVD Method 123
5.3 Data Set 3, Generator 5 analyzed by the SVD Method 124
5.4 Data Set 4, Generators 1 and 2 analyzed by the SVD Method 124
5.5 Data Set 5, Generators 3 and 4 analyzed by the SVD Method 125
5.6 Data Set 6, Generators 5 and 6 analyzed by the SVD Method 125

List of Figures

1.1 How overlapping generators can fool peak picking 9
1.2 Coordinate system used. 13

2.1 Electrode locations used for P50 study. 41
2.2 Frequency response of the 10-50 Hz digital bandpass filter. 42
2.3 P50 Response to the Conditioning-Testing Paradigm 46
2.4 P50 Response to the Conditioning-Testing Paradigm: Excluded Subject 47
2.5 Dipole Modeling of P50 Response 49

4.1 Planar projection of the electrode locations for simulations 85
4.2 Simulated data sets for generators 1, 3, and 5 89
4.3 Simulated data sets for generators 1 & 2, 3 & 4, and 5 & 6 90
4.4 Conditioning and testing responses at high and low SNR 91
4.5 Penalty functions for the bilateral constraint 95
4.6 Parameter error norms for Data Sets 1-3 111
4.7 Parameter error norms for Data Sets 4-6, modeled by one dipole . . . 112
4.8 Parameter error norms for Data Sets 4-6, modeled by two dipoles . . 113

Glossary of Abbreviations and Symbols

Notation: Bold-faced letters indicate vectors, bold-faced script letters indicate matrices, and normal-faced italic letters indicate scalars. Unit vectors (vectors of length 1) are indicated by a $\hat{}$.

SNR	signal to noise ratio
DCM	Dipole Components Model
C	conditioning response
T	testing response
C-T ratio	conditioning-testing ratio
CTR	conditioning-testing ratio
$\bar{x}$	estimated mean of x, defined as $\frac{1}{N}\sum_i^N x_i$
SD	standard deviation
COV	coefficient of variation, defined as $\bar{x}/SD$
EEG	electroencephalogram
EMG	electromyogram
EP	evoked potential

ERP	event related potential
EOG	electrooculogram
SVD	singular value decomposition
ICC	intraclass correlation coefficient
SRSS	scaled residual sum of squares
dpen	penalty added to the SRSS when dipole locations deviate from perfect bilateral symmetry
orpen	penalty added to the SRSS when dipole orientations deviate from perfect bilateral symmetry
tpen	penalty added to the SRSS when dipole time-varying magnitudes deviate from perfect synchrony
$\forall$	for all
$\| \mathbf{x} \|_2$	L_2 norm of vector $\mathbf{x}$, defined as $\sqrt{\sum_i^N x_i^2}$
$\| \mathbf{x} \|_\infty$	L_∞ norm of vector $\mathbf{x}$, defined as max $\|x_i\| \; \forall \; i$
$\Re$	The real numbers.
$\Re^k$	The k-tuples of real numbers.
n	number of electrodes, indexed by k
l	number of dipoles, indexed by j
u	number of time points, indexed by t
v	number of subjects or number of experimental conditions, indexed by s or e, respectively
k	index for electrodes

j	index for dipoles
t	index for time points
V_{kt}	the voltage recorded at time t from electrode k
$\boldsymbol{\theta}$	vector of dipole location in Cartesian coordinates, $(\theta_1, \theta_2, \theta_3)^T$
$f_{kd}(\boldsymbol{\theta})$	homogeneous sphere weight for electrode k in coordinate direction d due to dipole at location $\boldsymbol{\theta}$
$\boldsymbol{\phi}$	vector of dipole orientation in spherical coordinates, $(\phi_1, \phi_2)^T$
$f_k(\boldsymbol{\theta}, \boldsymbol{\phi})$	homogeneous sphere weight for electrode k due to a dipole at location $\boldsymbol{\theta}$ with orientation $\boldsymbol{\phi}$
$\boldsymbol{\xi}_t$	vector of dipole moments in Cartesian coordinates, $(\xi_1, \xi_2, \xi_3)^T$
$\boldsymbol{\eta}_k$	vector of electrode location in Cartesian coordinates, $(\eta_1, \eta_2, \eta_3)^T$
p_t	dipole magnitude at time t, defined as $\| \boldsymbol{\xi}_t \|_2$
f_{kj}	$f_{kj}(\boldsymbol{\theta}_j, \boldsymbol{\phi}_j)$, the homogeneous sphere weight for electrode k due to dipole j at location $\boldsymbol{\theta}_j$ and orientation $\boldsymbol{\phi}_j$
f_{kdj}	$f_{kdj}(\boldsymbol{\theta}_j)$, the homogeneous sphere weight for electrode k due to dipole j at location $\boldsymbol{\theta}_j$
ξ_{tdj}	dipole moment for dipole j at time t in Cartesian coordinate direction d
p_{jt}	dipole magnitude for dipole j at time t
α	amplitude of a decaying sinusoid
d^a	amplitude parameter scaling the decaying sinusoid (or other magnitude function) for data set a
λ	wavelength or period of a decaying sinusoid

τ	onset latency of a decaying sinusoid
τ^a	latency parameter adjusting the onset latency of the decaying sinusoid (or other magnitude function) for data set a
p_t^a	dipole magnitude for data set a at time t, defined as $d^a p_t$
β	decay parameter of a decaying sinusoid
$\mathbf{z}$	vector of covariates
$\gamma_{\mathcal{F}}$	Fourier frequency $2\pi\mathcal{F}/u$
$\mathbf{V}_{i\mathcal{F}}$	discrete Fourier transform at Fourier frequency $\gamma_{\mathcal{F}}$ for $\mathbf{V}_i(t)$, the $n \times 1$ vector of voltages recorded at time t for single trial i
$P_{\mathcal{F}j}$	discrete Fourier transform at Fourier frequency $\gamma_{\mathcal{F}}$ for $p_j(t)$, the magnitude at time t for dipole j
$\mathbf{E}_{i\mathcal{F}}$	discrete Fourier transform at Fourier frequency $\gamma_{\mathcal{F}}$ for $\mathbf{e}_i(t)$, the $n \times 1$ vector of noise at time t on single trial j
w	the number of Fourier frequencies included in the analysis
m	the number of single trials in an average
$\mathbf{V}_{gt}^a$	$n \times 1$ vector of given voltages (i.e., recorded voltages at n electrodes) at time t for data set a, also column t of $\mathcal{V}_g^a$
c^a	amplitude for the given generator of data set a
q_t	magnitude of the given generator at time t
$\mathbf{g}(\boldsymbol{\theta}_g, \boldsymbol{\phi}_g)$	$n \times 1$ vector of true weighting functions for the n electrodes due to the given generator at location $\boldsymbol{\theta}_g$ and orientation $\boldsymbol{\phi}_g$
g_m	magnitude of $\mathbf{g}(\boldsymbol{\theta}_g, \boldsymbol{\phi}_g)$, such that $\mathbf{g}(\boldsymbol{\theta}_g, \boldsymbol{\phi}_g) = g_m \hat{\mathbf{g}}$

$\hat{\mathbf{g}}$ unit vector describing the direction of $\mathbf{g}(\boldsymbol{\theta}_g, \boldsymbol{\phi}_g)$, such that $\mathbf{g}(\boldsymbol{\theta}_g, \boldsymbol{\phi}_g) = g_m \hat{\mathbf{g}}$

$q_t(\boldsymbol{\chi})$ magnitude of the given generator as a function of parameter vector $\boldsymbol{\chi}$ at time t

$\mathbf{V}_{ot}^a$ $n \times 1$ vector of unscaled fitted voltages (i.e., fitted voltages at n electrodes that have not yet been scaled by d^a) at time t for data set a, also column t of $\mathcal{V}_o^a$

$\mathbf{V}_{ft}^a$ $\mathbf{V}_{ft}^a = d^a \mathbf{V}_{ot}^a$, $n \times 1$ vector of fitted voltages (i.e., fitted voltages at n electrodes) at time t for data set a, also column t of $\mathcal{V}_f^a$

$\mathbf{f}(\boldsymbol{\theta}_f, \boldsymbol{\phi}_f)$ $n \times 1$ vector of homogeneous sphere weights for the n electrodes due to the fitted generator at location $\boldsymbol{\theta}_f$ and orientation $\boldsymbol{\phi}_f$, $(f_1(\boldsymbol{\theta}_f, \boldsymbol{\phi}_f), f_2(\boldsymbol{\theta}_f, \boldsymbol{\phi}_f), \ldots, f_n(\boldsymbol{\theta}_f, \boldsymbol{\phi}_f))^T$

f_m magnitude of $\mathbf{f}(\boldsymbol{\theta}_f, \boldsymbol{\phi}_f)$, such that $\mathbf{f}(\boldsymbol{\theta}_f, \boldsymbol{\phi}_f) = f_m \hat{\mathbf{f}}$

$\hat{\mathbf{f}}$ unit vector describing the direction of $\mathbf{f}(\boldsymbol{\theta}_f, \boldsymbol{\phi}_f)$, such that $\mathbf{f}(\boldsymbol{\theta}_f, \boldsymbol{\phi}_f) = f_m \hat{\mathbf{f}}$

$p_t(\boldsymbol{\psi})$ fitted magnitude of the dipole generator as a function of parameter vector $\boldsymbol{\psi}$ at time t

$\mathcal{V}_g^a$ $n \times u$ matrix of given voltages (i.e., recorded voltages at n electrodes over u time points) for data set a, such that the columns of $\mathcal{V}_g^a$ are $\mathbf{V}_{gt}^a$ for $t = 1, \ldots, u$

$\mathcal{V}_o^a$ $n \times u$ matrix of unscaled fitted voltages (i.e., fitted voltages at n electrodes over u time points) for data set a, that have not yet been scaled by amplitude parameter d^a, such that the columns of $\mathcal{V}_o^a$ are $\mathbf{V}_{ot}^a$ for $t = 1, \ldots, u$

$\mathcal{V}_f^a$	$\mathcal{V}_f^a = d^a \mathcal{V}_o^a$, $n \times u$ matrix of fitted voltages (i.e., fitted voltages at n electrodes over u time points) for data set a, such that the columns of $\mathcal{V}_f^a$ are $\mathbf{V}_{ft}^a$ for $t = 1, \ldots, u$
$\mathcal{A}$	$nu \times l$ matrix, map from dipole amplitude to potentials at the electrodes for multiple dipoles
$\mathbf{y}_j^T$	row j of the $l \times nu$ matrix $(\mathcal{A}^T\mathcal{A})^{-1}\mathcal{A}^T$, where $\mathbf{y}_j$ is an $nu \times 1$ vector
$\mathbf{e}_g$	$n \times 1$ vector of noise on the given potentials (i.e., the noise at the n electrodes)
$\mathbf{f}'(\boldsymbol{\theta}'_f, \boldsymbol{\phi}'_f)$	the homogeneous sphere dipole weights computed when $\boldsymbol{\theta}'_f$ and $\boldsymbol{\phi}'_f$ are estimated on noisy data
$\mathbf{e}_f$	$n \times 1$ vector of noise on the fitted electrode weights, such that $\mathbf{e}_f = \mathbf{f}(\boldsymbol{\theta}_f, \boldsymbol{\phi}_f) - \mathbf{f}'(\boldsymbol{\theta}'_f, \boldsymbol{\phi}'_f)$
σ_{bc}^2	variance between classes
σ_{wc}^2	variance within classes
$\hat{\sigma}_N^2$	estimated noise power
$\hat{\sigma}_S^2$	estimated signal power
$\hat{\sigma}_V^2$	estimated total power
$\mathbf{COV}_a$	vector of COVs belonging to group a
$\mathbf{COV}_b$	vector of COVs belonging to group b
$\mathbf{COV}_{r_1}$	random permutation of $\mathbf{COV}_a$ and $\mathbf{COV}_b$, such that group membership is not preserved
$\mathbf{COV}_{r_2}$	random permutation of $\mathbf{COV}_a$ and $\mathbf{COV}_b$, such that group membership is not preserved

δ_o	the mean observed difference between $\mathbf{COV}_a$ and $\mathbf{COV}_b$
δ_r	the mean difference between the randomly permuted vectors $\mathbf{COV}_{r_1}$ and $\mathbf{COV}_{r_2}$
$\boldsymbol{\Delta}$	normalized vector of differences in dipole parameters fit on a noise-free and noisy model
sv	singular value
$\mathcal{H}$	$u \times 2n$ matrix of recorded potentials, where the first n columns of $\mathcal{H}$ are the first data set, and the second n columns of $\mathcal{H}$ are the second data set
$\mathcal{U}$	$u \times u$ orthogonal matrix of left-hand singular vectors, one of the matrices found by singular value decomposition
$\mathcal{S}$	$min(u, 2n) \times min(u, 2n)$ matrix of diagonal elements, $sv_1, sv_2, \ldots, sv_{min(u,2n)}$ ordered such that $sv_1 \geq sv_2 \geq \ldots \geq sv_{min(u,2n)} \geq 0$
$\mathcal{W}$	$u \times 2n$ matrix, one of the matrices found by singular value decomposition
$\mathcal{Y}$	$2n \times 2n$ orthogonal matrix of right-hand singular vectors, one of the matrices found by singular value decomposition
$\mathcal{E}$	$n \times 2$ matrix, the first column contains the first n elements of the first right-hand singular vector of Y, the second column contains the second n elements of the first right-hand singular vector of Y
$\mathcal{X}'$	2×2 matrix, orthogonal matrix of right-hand singular vectors, found by singular value decomposition applied to $\mathcal{E}$
$\mathcal{Q}$	matrix of eigenvectors of a square, positive definite, symmetric matrix
$\boldsymbol{\Lambda}$	diagonal matrix of eigenvalues of a square, positive definite, symmetric matrix

$\mathcal{R}$	matrix of cross-correlations between electrodes

Chapter 1

Introduction

The study of brain electrical activity is a non-invasive method for investigating brain function. Evoked potentials (EPs) denote brain electrical activity that is elicited or evoked by an external stimulus, and event-related potentials (ERPs) denote brain electrical activity that occurs in response to an internally generated stimulus. In this dissertation, my use of "evoked potentials" includes event-related potentials, also.

Dipole modeling is an EP analysis technique which promises to advance knowledge of brain function. In dipole modeling, a method based on electric field theory, the neural generators of evoked potentials are modeled as current dipoles inside the head, with the equivalent dipole generators being those which gives rise to scalp potentials most like the measured potentials. Dipole modeling estimates the location, orientation, and time-varying activity of the equivalent dipole generators of evoked potentials.

Most dipole modeling research has focussed on fitting one or more dipoles to a single evoked potential average [1, 2, 3, 4, 5, 6, 7, 8, 9], with the resulting location parameters being of most interest. Most clinical and research applications of evoked potentials, however, are designed to study changes in the EP as a function of stimulus characteristics, drug states, disease states, or other between subject differences or within subject experimental manipulations. In analysis of variance or general linear models nomenclature, these between subject or within subject differences are called

covariate effects. In other words, a covariate is a predictor variable for the experimental manipulations (predicting the response to a conditioning stimulus vs. the response to a testing stimulus, for example), and the covariate effect is a measure of the brain response to experimental manipulations (i.e., the covariate effect is the magnitude of the difference between the conditioning and testing responses). Dipole modeling methods used in the papers cited above do not provide a means for analyzing multiple data sets and estimating such covariate effects.

In 1990, Turetsky, Raz, and Fein [10] proposed the Dipole Components Model (DCM) as an advance in the conceptual framework of dipole modeling. In the DCM, dipole sources for multiple data sets are fit concurrently with the constraint that the same dipoles (i.e., same locations and orientations) generated the data for all the data sets, and the dipoles are allowed to have differing time-varying activity for each data set. The DCM can be applied to multiple data sets gathered under different experimental conditions or from different subjects, and can be used to estimate covariate effects on the amplitude and latency of EPs.

Although the analysis method of dipole modeling is over 20 years old, the most popular dipole modeling algorithm (BESA–Brain Electrical Source Analysis, NeuroScan, Inc) is crude, using simplified physical head models and a nonparametric time-varying dipole magnitude function. These simplifications result in a tractable, but misspecified, problem. Previous research has shown that misspecification of the physical head model results in biased location and orientation parameter estimates (i.e., by biased estimates, I refer to estimates with systematic errors that cannot be "averaged" out) [11, 12, 13, 14, 15]. There has been little exploration of the effect of dipole modeling misspecification on the equivalent generator amplitude and amplitude ratios.

This dissertation investigates the effect of dipole model misspecification on the bias and variance of amplitude and derived amplitude ratio estimates for evoked potentials, when the Dipole Components Model is used to estimate covariate effects on EP amplitude. The estimation of covariate effects on EP amplitude using the DCM is described in detail in Section 1.3.4.

The experiment that led to my interest in the effects of model misspecifica-

tion on estimation of covariate effects on amplitude and the derived amplitude ratios is described in Chapter 2. In that chapter, I compared the reliability of the auditory evoked P50 conditioning-testing (C-T) ratio (an amplitude ratio) as measured by peak-picking versus dipole modeling.

The auditory P50 evoked potential is recorded in response to click stimulation. P50 has received great attention in the psychiatric community in recent years due to the phenomenon of P50 suppression. P50 suppression occurs when P50 is recorded in a paired click (or conditioning-testing) paradigm. In normals, the amplitude of the P50 response to the second (testing) click is reduced relative to the first (conditioning) click, when the clicks are separated by less than one second [16, 17, 18]. This suppression does not usually occur in schizophrenics or in about half of their first-degree relative [19, 20, 21, 22], and has been proposed as a potential genetic marker of the predisposition or vulnerability to schizophrenia.

P50 suppression is typically measured by the conditioning-testing (C-T) ratio, which is defined as the amplitude of the testing click response divided by the amplitude of the conditioning click response. Unfortunately, the excitement over these findings and the interest of the psychiatric research community in applying the P50 methodology to the study of schizophrenia has been tempered by the low test-retest reliability (as evidenced by a small intraclass correlation coefficient) of the C-T ratio as measured by peak-picking [23, 24]. A small intraclass correlation coefficient (ICC) indicates that the variability of the C-T ratio within a subject is large in comparison to the variability of the C-T ratio between subjects. With peak-picking, noise makes independent contributions to the conditioning and testing amplitude estimates, with more than cumulative effects on the C-T ratio. Because the Dipole Components Model uses multiple channels of information and because the DCM can simultaneously fit the conditioning and testing responses (thus "pooling" the effect of noise during the responses), I suspected that the DCM might lead to a more reliable C-T ratio.

Dipole modeling was applied to the auditory evoked P50 response as collected in a conditioning-testing paradigm, and amplitude parameters were fit to the conditioning and testing responses. Dipole modeling significantly improved the re-

liability (as measured by the ICC) of the C-T ratio as compared to peak-picking, implying that even a misspecified dipole model provided an advantage over peak-picking. Paradoxically, dipole modeling did not lead to an increase in the reliability of the conditioning and testing response amplitude estimates over peak-picking, only improving the reliability of the C-T ratio. These results led me to ask two questions: (1) The DCM resulted in more reliable C-T ratios, but were these ratio measures unbiased? and (2) Will DCM amplitude ratios always be more reliable than amplitude measurements (i.e., what is the variance of the estimates of covariate effects on amplitude as compared to the derived amplitude ratios?).

In order to answer question (1), I turned to the theory of linear least squares fitting as presented in Chapter 3. Chapter 3 shows that in two special cases, of which the P50 data analyzed in Chapter 2 is one, misspecification of the dipole model results in biased estimation of the covariate effects on amplitude, although the derived amplitude *ratios* are unbiased.

The proofs in Chapter 3 assumed noise-free evoked potentials, and therefore could not determine the variance of the covariate effects on amplitude estimated by dipole modeling or of the derived ratio estimates. Chapter 3, Section 3.2.5 examines the variance of covariate effects on amplitude assuming evoked potentials with Gaussian noise (a simplification), and shows that the variance of covariate effects on amplitude estimated by dipole modeling is not easily determined analytically, even when simplifying assumptions are made. Section 3.2.5 shows that simulations are necessary to determine the variance of the estimated covariate effects on amplitude, and to answer question (2).

Chapter 4 describes the simulations that were used to investigate the effect of dipole model misspecification on the variance of the estimators of covariate effects on amplitude, and the derived amplitude ratios. In summary, the results of Chapter 4 show that the variance of the derived amplitude ratios is smaller than the variance of the estimators of covariate effects on amplitude. The variances of the derived ratios and the estimators of covariate effects on amplitude were compared to their means, and the decreased ratio variance was evidenced by the increased coefficient of variation (COV) of the amplitude ratios, where the COV is defined as $\bar{x}/SD$. Increased

*COV*s result in increased reliability of derived amplitude ratios as compared to the estimators of covariate effects on amplitude. The results of Chapter 4 also showed that the concurrent presence of model misspecification and EEG noise did not lead to biased derived amplitude ratio estimates.

The results of Chapter 4 showed that the derived amplitude ratios were accurately and reliably estimated in the presence of model misspecification and noise, and the results of Chapter 3 show that this is because the effect of model misspecification "cancels" for a ratio measure. This led me to question whether a model was truly necessary for ratio estimation. In Chapter 5 I propose a method for estimation of evoked potential amplitudes and amplitude ratios that uses multiple channels of data but does not use the dipole model. When this method is applied to the simulated data used in Chapter 4, it results in increased amplitude *COV*s as compared to dipole modeling, and the ratio *COV*s are comparable to those obtained by dipole modeling. In addition, when this "model-free" method is applied to the real P50 data used in Chapter 2, it results in an improvement in reliability (as measured by the ICC) comparable to the improvement gained using dipole modeling. The model-free method is much faster and easier to use than dipole modeling, and may be very useful for analyzing data such as P50 where ratios are of most importance.

Chapter 6 discusses the results of this dissertation, and suggests future research.

The remainder of this chapter will introduce the reader to evoked potentials and the analysis of evoked potentials using dipole modeling. This chapter will also introduce notation used throughout the dissertation, as well as review the intraclass correlation coefficient, the statistic used to evaluate the variance of covariate estimates.

Notation: Bold-faced letters indicate vectors, bold-faced script letters indicate matrices, and normal-faced italic letters indicate scalars. Unit vectors (vectors of length 1) are indicated by $\hat{\mathbf{a}}$.

1.1 Evoked Potentials

The electrical activity of the brain can be recorded non-invasively from the scalp. Evoked potentials (EPs) are measurements of the surface electrical activity of the brain in response to a stimulus. A single stimulus response has a small amplitude at the scalp and is obscured by other physiological activity, such as the electroencephalogram (EEG) or electromyogram (EMG). Therefore, responses are elicited repeatedly and averaged in order to enhance the time-synchronized evoked potential. Generally, the term evoked potential refers to the averaged response.

EPs can be classified according to stimulus type, time of occurrence, and subject task. EPs in response to auditory, visual, and somatosensory stimulation are routinely recorded, and give information about the specific sensory system stimulated. EPs can be recorded at short and long latencies post-stimulus. Subcortical EPs are generated by the afferent sensory pathway to the primary sensory cortex. Subcortical EPs typically have latencies of less than 10-20 ms and amplitudes of less than 1 μV at the scalp. The auditory brainstem response [25] and the somatosensory P13 [26, 27] are examples of subcortical EPs. Short latency cortical EPs are generated by primary sensory cortex, and have latencies ranging from 10-100 ms and amplitudes of up to 10 μV or more. The somatosensory N20 is a classic example of a short latency cortical EP [28, 29]. Subcortical and short-latency cortical EPs are considered to be "hard-wired," and the physical characteristics of the stimulus determine the response. As such, no subject participation or awareness is required, and many subcortical and short-latency EPs can be recorded while a subject is sleeping. These short-latency EPs are often referred to as exogenous potentials [30]. Longer latency cortical EPs reflect processing by higher order cortical areas (i.e., not primary or perhaps even secondary cortex), and typically have latencies of over 100 ms and are usually larger in amplitude than the short latency cortical EPs. Some long-latency cortical EPs, of which the P300 and readiness potential are examples, require the subject to perform a task or at the very least stay awake and alert. These EPs seem to reflect cognitive processing, because the EP can still be recorded even when the physical characteristics of the stimulus change (i.e., a P300 can be recorded in response to either an unexpected stimulus or

the *absence* of an expected stimulus; therefore the P300 response *must* be cognitive, not sensory). These long-latency EPs are often referred to as endogenous EPs [30].

EPs are typically characterized by describing the latency, polarity, and amplitude of peaks in individual channels of data, a process known as peak picking. These peaks are usually the primary measures of the EP components. Many researchers have collected EPs to visual, auditory, and somatosensory stimulation from subjects with no sensory deficits. These data were used to determine normative values for the peak characteristics of each type of EP. These normative values have been used to establish guidelines for the clinical use of EPs [31, 32].

Short latency exogenous EPs are clinically useful for testing conduction along afferent pathways. A short latency EP with an abnormal peak latency may signal a lesion in the afferent pathway [31]. EPs are also used to monitor activity of the brain or afferent structures during surgery [33]. Some longer latency endogenous EPs seem to reflect the activity of complex cognitive or psychological processes, and are used to study psychiatric populations [19, 34, 30]. In these clinical applications, peak characterization (or peak picking) is the most frequent method of analysis.

Many of the clinically useful applications of EPs depend on the stability and reliability of the EP over time. EP amplitudes as measured by peak picking are less reliable than are EP latency measures; therefore EP latencies are more often used clinically. Nevertheless, in some research work, amplitude changes have been observed in the absence of latency changes [35, 36, 18, 37]. A reliable method of amplitude measurement is required before these observations can be employed clinically, and peak picking is not satisfactory.

Peak picking is limited because it cannot describe the pattern of brain activation that resulted in the presence of an EP. An EP component (i.e., "peak") may reflect the summation of electrical activity from two or more brain regions. Peak picking cannot separate these overlapping contributions and instead identifies one peak. In such a case, the latency of this peak may not represent the peak latency of brain activation. Figure 1.1 describes such a case. Plot (a) shows the overlapping activity (in time) of two widely separated simulated neural generators. Plot (b) shows the signal that would be generated by these overlapping contributions at the vertex elec-

trode, if no noise were present. The shape is irregular, and may lead one to suspect multiple generators. However, plot (c) shows the same signal when noise is added, and plot (d) shows a filtered version of the data from plot (c). Only a single peak is evident in plot (d), and this demonstrates one way that peak picking can be "fooled."

Peak picking is limited because it cannot describe the brain changes that cause an abnormal EP. Peak picking is also limited because it describes the latency and amplitude of EP peaks (i.e., peak picking characterizes a single time point in the wave), and these peak measurements are sensitive to such things as noise (i.e., EEG and EMG noise), filter settings, errors in electrode placement, and electrode impedance. These limitations have led investigators to use additional techniques to describe the EP, such as principal components analysis, topographic mapping, and dipole modeling. Several of these techniques attempt to locate the neural generators of the EP.

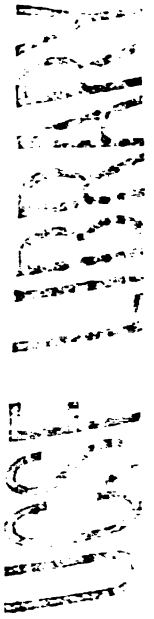

1.2 Neural Generators of Evoked Potentials

Investigators agree that short latency EP components are generated by structures along the afferent pathway, and educated "guesses" about the location and orientation of the equivalent generators of short latency EPs can be made. However, the neural generators of long latency EP components cannot be related to the anatomy of afferent pathways, and the location and orientation of long latency components are therefore more difficult to determine. In addition, anatomy can only suggest neural generator location and orientation, and the behavior of the generator over time (i.e., intensity of response) cannot be characterized without additional information. Knowledge of the location, orientation, and time-varying magnitude of EP generators would allow more precise diagnosis of functional brain abnormalities, and potentially might lead to a better understanding of how psychological processes are related to brain structures.

The techniques employed by researchers to attempt to locate the sources of EPs include intracranial recording of EPs [38, 39, 40, 41, 29, 42], characterization of EP changes due to lesions [43, 44, 45, 46, 47], topographic mapping of EPs [48, 49, 50],

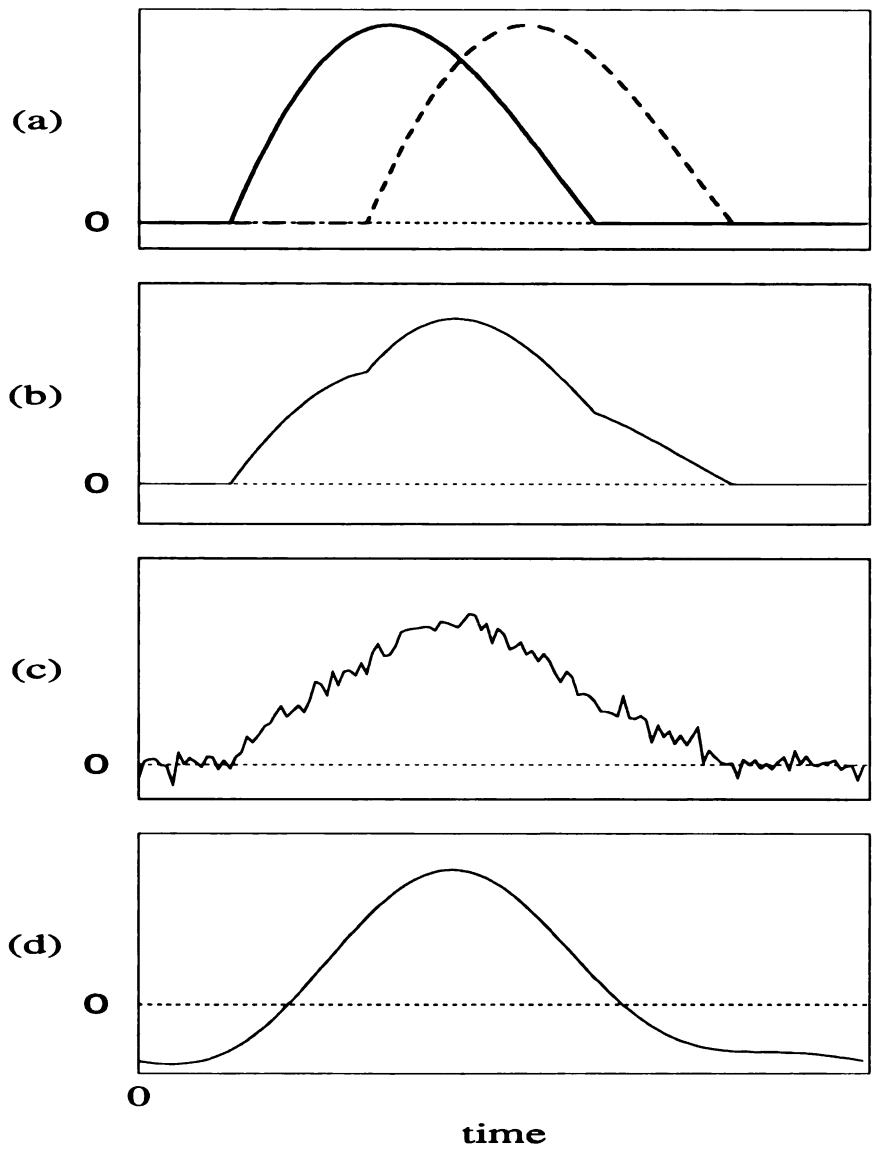

Figure 1.1: How overlapping generators can fool peak picking
Plot (a) shows the time-varying activation of two generators widely separated in space, but overlapping in time. Plot (b) shows the summation of the two generators as it would appear at the vertex. Plot (c) is a noisy version of the data in plot (b). Plot (d) is a filtered version of the data in plot (c). Only a single peak is evident in plot (d), which would fool peak picking.

and volume conduction models based on electric field theory [8, 9, 1, 51, 7, 10, 52]. Intracranial recordings are obtained from surgically implanted electrodes. Only subjects with severe neurological disorders are surgically implanted, and the electrode positions are determined by clinical considerations, not research considerations. Lesion studies are limited because of the difficulty in determining the extent of the lesion, interpreting the effect of the lesion on the EP, and because in humans one cannot choose the lesion site. It is also difficult to duplicate results, since lesions differ from patient to patient. Difficulties associated with topographic mapping include determination of which EP components to examine, correlating the map with the assumed underlying sources, and selection of an appropriate reference electrode. Volume conduction models make simplifying assumptions about head shape and conductivity, and the solutions are not unique. In summary, no method is ideal.

Because this dissertation investigates the effect of dipole model misspecification on the bias and variance of covariate estimates, I will not consider intracranial recordings, lesion studies, or topographic mapping further. The next section introduces the dipole model.

1.3 Dipole Modeling

The analysis of evoked potentials by dipole modeling is based on electric field theory. In this method, the neural generators of evoked potentials are modeled as current dipoles. There are several conditions under which a compound action potential can be well modeled by a dipole, such as when it is initiated, when it traverses a narrow region of the volume conductor, when it reaches the end of an axon, when it traverses a short axon, when it traverses a curved axon, and when it traverses a boundary between adjacent regions of differing media conductivity [53, 54, 55, 56]. In addition, synchronous activity of cortical pyramidal cells, which are oriented toward the cortical surface, causes intraneuronal current flow parallel to the neurons. This results in different cortical layers acting as sources and sinks, and thus generates a current dipole [57, 58, 59] or quadrupole [60] oriented perpendicular to the cortical layers. The effect of any arrangement of sources and sinks (or cortical source) in the

far-field can be well-approximated by a dipole [61]. The following sections present the equation which describes the surface voltage due to a dipole inside a homogeneous sphere and methods for solving the inverse problem.

1.3.1 Describing Equation

Several simplifying assumptions have been made in order to write the following analytical expression for the surface voltage due to a neural generator in the head. These are:

1 The head is a sphere filled with a medium of homogeneous conductivity.

2 The neural generator is a point current dipole.

3 The location of the generator is fixed over its time of activation.

4 The radius of the head is 1 unit (the computed potentials can be easily scaled if the radius does not equal 1).

5 The conductivity of the head is 1 unit (the computed potentials can be easily scaled if the conductivity does not equal 1).

A current dipole in a sphere, as well as the coordinate system to be used in this dissertation, is illustrated in Figure 1.2. The signal at scalp electrode k, $(k = 1, \ldots, n)$, at time t due to single dipole is [62, 52]:

$$V_{kt} = f_{k1}(\boldsymbol{\theta})\xi_{t1} + f_{k2}(\boldsymbol{\theta})\xi_{t2} + f_{k3}(\boldsymbol{\theta})\xi_{t3} \tag{1.1}$$

where:

$$f_{kd}(\boldsymbol{\theta}) = f^0_{kd}(\boldsymbol{\theta}) - f^0_{(n+1)d}(\boldsymbol{\theta}) \quad k = 1, \ldots, n; \quad d = 1, 2, 3 \tag{1.2}$$

$$f^0_{kd}(\boldsymbol{\theta}) = \frac{-2a_{kd}}{\rho_k^2} + \frac{\eta_{kd}}{\rho_k} + \frac{\eta_{kd}b_k - \theta_d}{\zeta_k} \quad k = 1, \ldots, n+1; \quad d = 1, 2, 3 \tag{1.3}$$

$$\begin{aligned} \boldsymbol{\theta} &= (\theta_1, \theta_2, \theta_2)^T \\ \boldsymbol{\xi}_t &= (\xi_{t1}, \xi_{t2}, \xi_{t3})^T \end{aligned}$$

$$\begin{aligned}
\boldsymbol{\eta}_k &= (\eta_{k1}, \eta_{k2}, \eta_{k3})^T \\
\rho_k &= \| \boldsymbol{\eta}_k - \boldsymbol{\theta} \|_2 && (1.4) \\
a_{kd} &= \frac{\theta_d - \eta_{kd}}{\rho_k} && (1.5) \\
b_k &= \boldsymbol{\eta}_k \cdot \boldsymbol{\theta} && (1.6) \\
\zeta_k &= \rho_k^2 + \rho_k - b_k \rho_k && (1.7)
\end{aligned}$$

where $\boldsymbol{\theta}$ is a vector representing the dipole location in Cartesian coordinates. The vector of dipole magnitudes in Cartesian coordinates at time t is $\boldsymbol{\xi}_t$. I use the notation $\boldsymbol{\xi}_t$ instead of $\boldsymbol{\xi}(t)$ because evoked potentials are discrete time-series, not continuous time-series. The electrode location k in Cartesian coordinates is $\boldsymbol{\eta}_k$, d indexes the three coordinate directions, and $\boldsymbol{\eta}_{n+1}$ is the location of the reference electrode. In the coordinate system used in this dissertation, the x axis runs between the nasion and inion (nasion is positive), the y axis runs between the left and right auditory meatus (left is positive), and the z axis runs between the positive vertex and the intersection of the x and y axis. This is a right handed coordinate system.

Alternatively, when the generator is assumed to be fixed in location *and* orientation, Equation 1.1 can be expressed in spherical coordinates, where ϕ_1 is the co-latitude and ϕ_2 is the longitude. The signal at electrode k at time t is then:

$$V_{kt} = f_k(\boldsymbol{\theta}, \boldsymbol{\phi}) p_t \tag{1.8}$$

where

$$\begin{gathered}
f_k(\boldsymbol{\theta}, \boldsymbol{\phi}) = f_{k1}(\boldsymbol{\theta}) sin\phi_1 cos\phi_2 + f_{k2}(\boldsymbol{\theta}) sin\phi_1 sin\phi_2 + f_{k3}(\boldsymbol{\theta}) cos\phi_1 \\
k = 1, \ldots, n
\end{gathered} \tag{1.9}$$

and where

$$\begin{aligned}
p_t &= \sqrt{\xi_{t1}^2 + \xi_{t2}^2 + \xi_{t3}^2} \\
&= \| \boldsymbol{\xi}_t \|_2
\end{aligned}$$

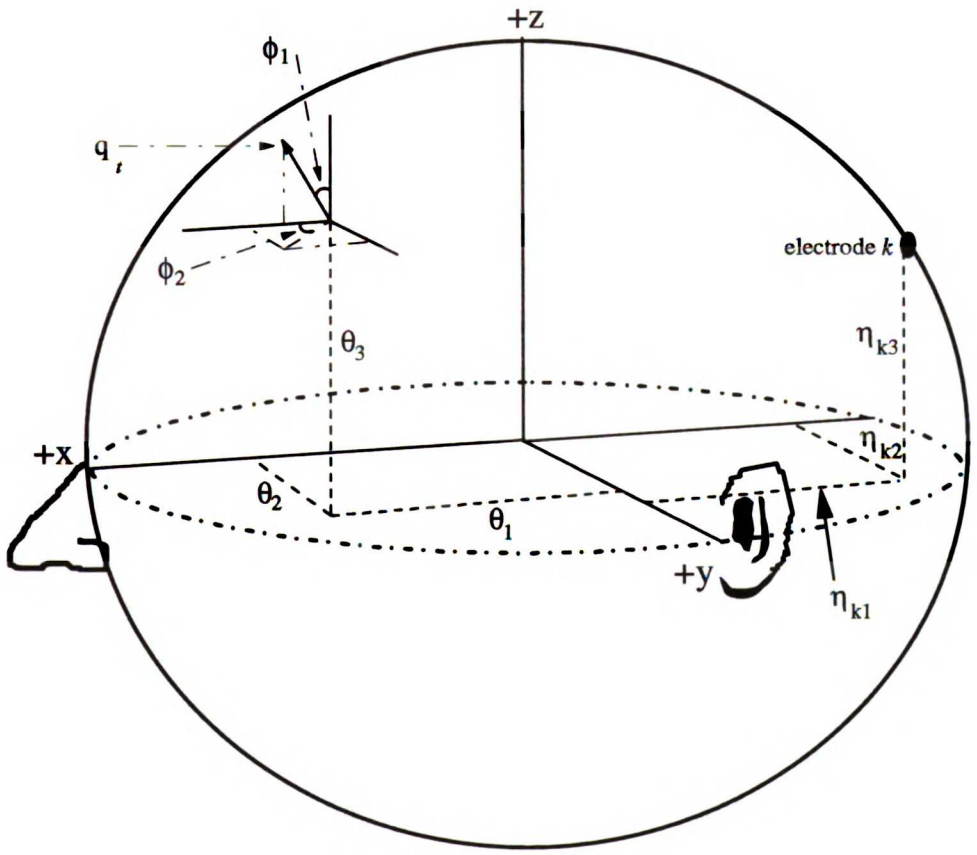

Figure 1.2: Coordinate system used.

i.e., the following relationships hold

$$\begin{aligned} \xi_{t1} &= p_t sin\phi_1 cos\phi_2 \\ \xi_{t2} &= p_t sin\phi_1 sin\phi_2 \\ \xi_{t3} &= p_t cos\phi_1 \end{aligned} \tag{1.10}$$

As noted previously, it is trivial to scale the potentials when assumptions 4 and 5 are violated, and all other assumptions still hold. This is accomplished in the following manner. Let R be the true radius and M be the true conductivity. According to [62], the scaled potentials S are then

$$S_t = \frac{1}{MR^2} V_t$$

Linear superposition holds in a volume conductor, therefore when more than one dipole is present in the sphere, the voltage measured at the surface is equivalent to the algebraic sum of the individual contributions. Therefore, if V_{kt} is generated by l dipoles, the signal at electrode k becomes

$$V_{kt} = \sum_{j=1}^{l} f_{ki}(\boldsymbol{\theta}_i, \boldsymbol{\phi}_i) p_{it}$$

where $f_{ki}(\boldsymbol{\theta}_i, \boldsymbol{\phi}_i)$ is the weighting function at electrode k due to dipole i, and p_{it} is the dipole magnitude function for dipole i at time t.

Previous investigators have used more realistic (and thus more complicated) models for the head than the homogeneous sphere model. The head is clearly very different from a homogeneous sphere, and the use of this simple head model introduces model misspecification. Since this dissertation is concerned with investigating the errors in the estimates of covariate effects when model misspecification is present, and also because the simple head model is computationally advantageous, I will be using the homogeneous sphere dipole model in my data analysis and simulations.

Solutions to the homogeneous sphere dipole model can be found using either a time domain approach [1, 63] or a frequency domain approach [52, 64, 65]. In addition, the problem can be solved by estimating all parameters using nonlinear optimization techniques, or by "splitting" the problem into nonlinear and linear parts, and solving each part using appropriate numerical methods. In this dissertation, I

will only be solving the intracranial dipole model in the time domain, and will focus my review on time domain solutions.

Most dipole modeling of evoked potentials in the time domain has focussed on fitting one or more dipoles to a single evoked potential average, and do not estimate covariate effects. The estimation of covariate effects (i.e., the *size* of an effect on the amplitude or latency of an EP due to experimental manipulations) is essential for EP research. The Dipole Components Model (DCM) is an extension of dipole modeling in the time domain to include estimation of covariate effects on EP amplitude and latency, and the DCM will be reviewed. Some discussion of frequency domain solutions will be included, because of the ease of estimating covariate effects on EP amplitude and latency in the frequency domain.

It is important to understand how the problem is solved when "split" into linear and nonlinear parts, so I will describe linear and nonlinear solutions in great detail.

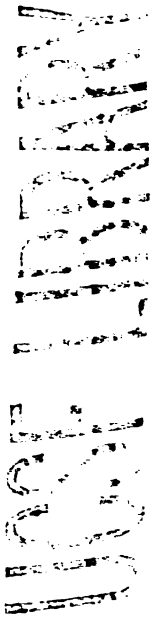

1.3.2 Linear Solutions

In the dipole model, the scalp recorded potentials are a function of the equivalent dipole generator location, orientation, and magnitude over time (see Equations 1.1-1.9). In Equation 1.8, the equivalent dipole generator location and orientation are fixed, and the scalp recorded potentials are a *nonlinear* function of dipole location and orientation (the weighting function $f_k(\boldsymbol{\theta}, \boldsymbol{\phi})$ is a nonlinear function of dipole location and orientation), and a *linear* function of the dipole magnitudes p_t. In Equation 1.1, only the dipole location is fixed, and the scalp recorded potentials are a *nonlinear* function of dipole location (the weighting function $f_{kd}(\boldsymbol{\theta})$ is a nonlinear function of the dipole location), and a *linear* function of the dipole magnitudes in the three Cartesian coordinate directions, ξ_{td}.

If the locations and/or orientations of the neural generators are fixed and either known or have been previously estimated, then the electrode weighting functions $f_k(\boldsymbol{\theta}, \boldsymbol{\phi})$ can be easily computed by Equations 1.1-1.9. This situation can arise on the rare occasion when the locations and orientations of the generators are known from

anatomy. This situation occurs more frequently when the dipole model is "split" into linear and nonlinear parts, i.e. when a linear method is used to estimate the linear parameters after a nonlinear optimization routine is used to estimate the other parameters (usually location and orientation, but sometimes time varying magnitude parameters also).

If the locations and orientations of the dipole generators are fixed, then Equation 1.8 must be solved for the dipole locations, orientations, and dipole magnitudes over time. Assuming that the dipole location and orientation are known or have been estimated using a nonlinear optimization routine, the electrode weighting functions $f_k(\boldsymbol{\theta}, \boldsymbol{\phi})$ can be computed by Equations 1.1- 1.9. In this case, only the dipole moments over time, p_t, must be solved for each generator, and this is a linear problem. The voltage at a number of electrodes due to several sources can be written as a matrix problem, as follows.

$$\begin{pmatrix} f_{11} & f_{12} & \cdots & f_{1l} \\ f_{21} & f_{22} & \cdots & f_{2l} \\ f_{31} & f_{32} & \cdots & f_{3l} \\ \vdots & \vdots & \ddots & \vdots \\ f_{n1} & f_{n2} & \cdots & f_{nl} \end{pmatrix} \begin{pmatrix} p_{11} & p_{12} & \cdots & p_{1u} \\ p_{21} & p_{22} & \cdots & p_{2u} \\ \vdots & \vdots & \ddots & \vdots \\ p_{l1} & p_{l2} & \cdots & p_{lu} \end{pmatrix} = \begin{pmatrix} V_{11} & V_{12} & \cdots & V_{1u} \\ V_{21} & V_{22} & \cdots & V_{2u} \\ V_{31} & V_{32} & \cdots & V_{3u} \\ \vdots & \vdots & \ddots & \vdots \\ V_{n1} & V_{n2} & \cdots & V_{nu} \end{pmatrix}$$

where u is the number of time points, n is the number of electrodes, and l is the number of dipole sources. The notation is as follows: V_{kt} is the recorded voltage at electrode k at time point t, f_{kj} is the electrode weighting function $f_{kj}(\boldsymbol{\theta}_j, \boldsymbol{\phi}_j)$ for dipole j, and p_{jt} is the dipole magnitude for dipole j at time point t. In this example, there are 3 location and 2 orientation parameters for each dipole, and u dipole moment parameters for each dipole ($[5 + u] \times l$ parameters total, $5 \times l$ parameters known or estimated using a nonlinear method, and $u \times l$ parameters estimated linearly).

The problem can still be written in matrix notation if the locations of the generators are fixed but the orientations are allowed to vary. A fixed location, varying orientation generator can be used to model a sequentially activated section of cortex. The centroid of the cortical section is the location of the dipole, and the dipole orientation varies as the cortex is activated. The fixed location, varying orientation

dipole is a simplification of the true physiology, as the centroid of the activated cortical section would shift and would not be concurrent with the centroid of the entire cortical section.

For a fixed location and variable orientation dipole, Equation 1.1 must be solved. Assuming that the locations of the generators are known or have been estimated using a nonlinear optimization routine, the weighting functions $f_{kdj}(\boldsymbol{\theta})$ can be computed by Equations 1.2-1.7. In this case, the dipole magnitude in each coordinate direction can be estimated linearly (this is sometimes referred to as solving for a "triplet" dipole). When dipole orientations are allowed to vary over time, the voltage at a number of electrodes due to several sources can be written as follows.

$$\begin{pmatrix} f_{111} & f_{121} & f_{131} & \cdots & f_{11l} & f_{12l} & f_{13l} \\ f_{211} & f_{221} & f_{231} & \cdots & f_{11l} & f_{12l} & f_{13l} \\ \vdots & \vdots & \vdots & \ddots & \vdots & \vdots & \vdots \\ f_{n11} & f_{n21} & f_{n31} & \cdots & f_{n1l} & f_{n2l} & f_{n3l} \end{pmatrix} \begin{pmatrix} \xi_{111} & \cdots & \xi_{u11} \\ \xi_{121} & \cdots & \xi_{u21} \\ \xi_{131} & \cdots & \xi_{u31} \\ \xi_{112} & \cdots & \xi_{u12} \\ \xi_{122} & \cdots & \xi_{u22} \\ \xi_{132} & \cdots & \xi_{u32} \\ \vdots & \ddots & \vdots \\ \xi_{11l} & \cdots & \xi_{u1l} \\ \xi_{12l} & \cdots & \xi_{u2l} \\ \xi_{13l} & \cdots & \xi_{u3l} \end{pmatrix} = \begin{pmatrix} V_{11} & \cdots & V_{1u} \\ V_{21} & \cdots & V_{2u} \\ \vdots & \ddots & \vdots \\ V_{n1} & \cdots & V_{nu} \end{pmatrix}$$

where f_{kdj} is the electrode weighting function $f_{kdj}(\boldsymbol{\theta})$ for dipole j, and ξ_{tdj} is the dipole moment at time point t in coordinate direction d for dipole j. In this example, there are three location parameters for each dipole (which are known or estimated using a nonlinear optimization routine), and $3 \times u$ linearly estimated dipole moment parameters for each dipole ($[3 + 3 \times u] \times l$ parameters total).

In the previous two examples, it was assumed that the dipole locations and/or orientations were known or had been estimated by a nonlinear optimization routine. The dipole moments were then solved at each time point. This leads to a large number of estimated parameters. In order to reduce the total number of parameters estimated, the time-varying dipole magnitude function can be parameterized.

The Dipole Components Model (DCM) of Turetsky [10] fixes the location and orientation of each dipole, and parameterizes the time-varying dipole moment function as a decaying sinusoid. Nonlinear optimization is used to estimate the location, orientation, and decaying sinusoid parameters for the equivalent dipole generator. The decaying sinusoid dipole magnitude function is described by:

$$p_t = sin[\frac{2\pi}{\lambda}(t-\tau)]e^{-\beta(t-\tau)} \tag{1.11}$$

and the equation for V_{kt} is

$$V_{kt} = \sum_{j=1}^{l} \alpha_j p_{jt} f_{kj}(\boldsymbol{\theta}_{kj}, \boldsymbol{\phi}_{kj}) \tag{1.12}$$

where λ is the wavelength, τ is onset latency, β is the decay of the decaying sinusoid, and α is the intensity or amplitude of the dipole. If the dipole location, orientation, and magnitude function shape (described by λ, τ, and β) are known or have been estimated, then $f_{kj}(\boldsymbol{\theta}_j, \boldsymbol{\phi}_j)$ and p_t can be easily computed. The linear problem of estimating the magnitude of the decaying sinusoid can be written in matrix notation, as follows,

$$\begin{pmatrix} f_{11}p_{11} & f_{12}p_{21} & \cdots & f_{1l}p_{l1} \\ \vdots & \vdots & \ddots & \vdots \\ f_{n1}p_{11} & f_{n2}p_{21} & \cdots & f_{nl}p_{l1} \\ f_{11}p_{12} & f_{12}p_{22} & \cdots & f_{1l}p_{l2} \\ \vdots & \vdots & \ddots & \vdots \\ f_{n1}p_{12} & f_{n2}p_{22} & \cdots & f_{nl}p_{l2} \\ \vdots & \vdots & \vdots & \vdots \\ \vdots & \vdots & \vdots & \vdots \\ f_{11}p_{1u} & f_{12}p_{2u} & \cdots & f_{1l}p_{l1} \\ \vdots & \vdots & \ddots & \vdots \\ f_{n1}p_{1u} & f_{n2}p_{2u} & \cdots & f_{nl}p_{lu} \end{pmatrix} \begin{pmatrix} \alpha_1 \\ \alpha_2 \\ \vdots \\ \alpha_l \end{pmatrix} = \begin{pmatrix} V_{11} \\ \vdots \\ V_{n1} \\ V_{12} \\ \vdots \\ V_{n2} \\ \vdots \\ \vdots \\ V_{n1} \\ \vdots \\ V_{nu} \end{pmatrix}$$

where f_{kj}, p_{jt}, and V_{kt} are the same as described previously, and α_j is the magnitude of the dipole moment function for dipole j. This leads to 3 location, 2 orientation, and

3 dipole magnitude "shape" parameters for each dipole (estimated using a nonlinear optimization method), and 1 linearly estimated dipole magnitude parameter for each dipole ($9 \times l$ parameters total).

The three matrix problems defined above are all matrix equations of the form $Ax = b$. Note that in the first two problems shown, x and b are actually matrices, but the problem can be treated as $Ax = b$ with multiple right hand sides (i.e., the first column of b is the first right hand side, and is used to solve for the first column of x, the second column of b is the second right hand side and is used to solve for the second column of x, and so on). Such problems can be easily solved using standard linear algebra techniques, such as performing an LU decomposition of A and using backsubstitution to solve for each right hand side. Many "canned" routines are available to solve this problem [66, 67, 68, 69].

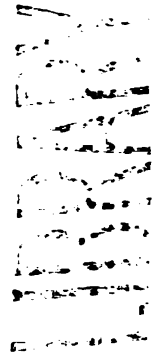

1.3.3 Nonlinear Solutions

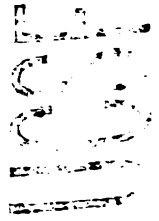

In setting up the problems above, I assumed that the dipole locations and/or orientations were known or had been previously estimated, and that parameters related to the dipole magnitude over time could then be solved using linear methods. In the third linear problem described above, I assumed that the parameters of the decaying sinusoid had been previously estimated using a nonlinear optimization routine, and the magnitude of the decaying sinusoid could be estimated using linear methods.

In practice, nonlinear optimization techniques are used to estimate some or all of the parameters of the dipole model, because the locations and orientations of the equivalent dipole generators are rarely known. Nonlinear optimization techniques are used alone or with linear estimation techniques. When used alone, all parameters of the dipole model (locations, orientations, and dipole magnitudes) are estimated using nonlinear optimization. Frequently, however, within an iteration, the nonlinear optimization algorithm is used to estimate the locations and/or orientations, and the remaining dipole magnitude parameters are estimated linearly (e.g., ξ_{td} of Equation 1.1, p_t of Equation 1.8, or α_j when the dipole magnitude is parameterized) [63, 70].

Iterative nonlinear optimization routines attempt to minimize an objective function of several parameters (often a sum of squared errors) by adjusting those parameters. At each iteration, the optimization algorithm perturbs the current parameters in a deterministic (as in the Newton methods or nonlinear simplex) or stochastic (as in simulated annealing or genetic algorithms) manner, and recomputes the objective function. The value of the objective function determines whether the perturbed parameters are accepted or rejected. The process continues until a minimum of the objective function is reached (hopefully the lowest or global minimum).

The dipole model estimation problem is complex, resulting from a large number of parameters and their nonlinear relationships (see Equations 1.1-1.7). The resulting multivariate estimation surface often has both large numbers of local minima and a very shallow sloping surface near the global minimum. Such estimation problems overwhelm the capabilities of the most popular nonlinear estimation procedures, the Newton-type methods, leading to convergence at local minima.

The Newton-type methods were the original methods used for dipole modeling [8, 1, 51]. Because of the above problems, the nonlinear simplex method (sometimes called the polytope method to distinguish it from the better-known linear programming simplex method) has become the method commonly used in equivalent dipole source modeling [71, 12, 10, 72]. The nonlinear simplex is a derivative-free method that often works well on nonlinear estimation surfaces, and adapts better than Newton methods to moving through and out of long valleys.

The application of the dipole model to auditory P50 data, described in Chapter 2, used the nonlinear simplex method to estimate the dipole parameters. Although simplex was known to converge to local minima for multiple dipole problems, most researchers were of the opinion that local minima were not a problem for single dipole problems such as in Chapter 2. Since that work was accomplished, it has been shown that the simplex method can converge to local minima even for simple single dipole estimation problems [73]. In order to reduce and possibly eliminate the frequency of convergence to local minima, for the simulation experiments described in Chapter 4, I have used simulated annealing. Simulated annealing has been recently shown to be superior to the simplex method for avoiding convergence to local minima when

estimating dipole parameters [73]. Because this dissertation uses both the simplex method and simulated annealing for estimation of dipole parameters, both methods will be reviewed.

Simplex

The simplex method works along the following lines: Suppose there are n parameters to be estimated. First, a simplex is formed. A simplex is a geometric figure with $n+1$ vertices in n-dimensional space (e.g., a triangle in the plane). Each vertex of the simplex has n coordinates, corresponding to estimates of the n parameters. The scaled residual sum of squares ($SRSS$, the sum of squared differences between observed and predicted values, scaled by the sum of the squared observed values) is computed for the parameter estimates at each vertex. The simplex's primary action is to move away from the worst vertex (i.e., the one with the largest $SRSS$) by replacing that vertex with its reflection through the centroid of the remaining vertices. If it cannot find a better point through reflection, the simplex will then contract along a single dimension away from the worst vertex. If a contraction away from the worst vertex does not yield a better point, the simplex will perform a contraction in multiple dimensions around the lowest (best) point. These steps give the simplex an amoeba-like motion that helps it to move rapidly when good reflection moves are available, and to contract in on itself to slither through long valleys. Simplex will only take "downhill" steps (i.e., steps that reduce the value of the SRSS at that vertex). Because simplex can only take downhill steps, it is sensitive to starting values.

In implementing the simplex method, starting and step values (used to construct the initial simplex) must be chosen and a convergence criterion defined. For convergence, the fractional difference between the highest and lowest $SRSS$ at the vertices (the difference of the highest and lowest $SRSS$ divided by the sum of the highest and lowest $SRSS$) must be less than a preset value [66]. Note that this convergence criterion does not guarantee that the simplex is at a minimum in parameter space (i.e., the simplex can shrink to a small enough size to satisfy the convergence criteria but not be at a minimum–this can occur if the multivariate estimation sur-

face is shallow). Although not implemented in the application in Chapter 2, in more recent work [73] a second convergence criterion was added. If the first convergence criterion is met, then it is required that the vertex with the lowest $SRSS$ is truly at a minimum in the parameter space. This is accomplished in a round-robin fashion. Each parameter is perturbed by a small amount while holding the other parameters constant and the $SRSS$ is calculated and compared to the proposed minimum. If the proposed minimum is the smallest, the solution is conditionally accepted. After convergence is reached, the simplex is restarted at the current solution (with a new, large simplex) in order to verify that a better solution cannot be found [74, 66]. When the restarted simplex reconverges to the same parameter values the simplex solution is accepted.

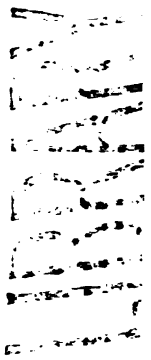

Simulated Annealing

Simulated annealing [75] is a stochastic simulation method for global optimization that has been shown theoretically [76], in large-scale simulation studies [77], and in applications [75, 78] to have superior properties in finding the global minimum on complex nonlinear multivariate estimation surfaces with many local minima as compared to other nonlinear optimization methods. Simulated annealing proceeds towards its solution by randomly generating candidate steps from a probability distribution (usually either Gaussian or Cauchy; the Cauchy distribution is simply a t distribution with 1 degree of freedom). A downhill step (i.e., a step to a location with a smaller $SRSS$) is always accepted. Uphill steps are sometimes accepted, with a probability inversely proportional to the size of the increase in the $SRSS$. As the estimation process proceeds, the probability of accepting uphill steps is systematically decreased.

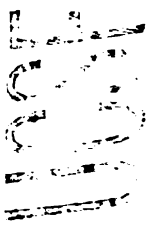

Despite its simplicity, this method is extremely powerful. By sometimes allowing uphill steps, the process can move away from local minima. Although simulated annealing initially samples from the entire parameter space, it progressively homes in on the global minimum by decreasing the probability of taking an uphill step. This makes simulated annealing feasible for complex problems in contrast to

exhaustive direct search methods. The procedure by which the probability of uphill steps is decreased is called the cooling schedule. Simulated annealing literally attempts to imitate the process whereby substances cool to their most stable states according to the Boltzmann probability distribution. Geman and Geman [76] proved that if the cooling schedule is sufficiently slow, simulated annealing will converge to the global minimum.

When substances cool naturally to their ground states, temperature decreases slowly, and energy usually decreases with temperature. However, energy may occasionally increase while temperature decreases. The relationship between energy and temperature level is:

$$Prob(E) \sim \exp(-E/kT) \tag{1.13}$$

where E is the energy, T is the temperature, and k is Boltzmann's constant. Equation 1.13 is known as the Boltzmann distribution, and illustrates that at low temperature there is still a small probability of the system being in a high energy state.

Metropolis [79] simulated changes in a thermodynamic system using the relationship:

$$Prob(\Delta E) \sim \exp(-\Delta E/kT)$$

Simulated annealing applies this idea to parameter estimation via minimization of a function of the parameters. The objective function is the analog of E in Equation 1.13. In the dipole modeling problem, the objective function is the scaled residual sum of squares, and the annealing equation takes the form:

$$Prob(\Delta SRSS) = \begin{cases} 1 & \text{when } \Delta SRSS < 0 \\ \exp(-\Delta SRSS/kT) & \text{otherwise} \end{cases} \tag{1.14}$$

Parameter estimates are generated sequentially and their $SRSS$ is computed. The difference in $SRSS$ between the current and next candidate set of parameter estimates is set to $\Delta SRSS$; k is fixed at 1, and T is started at some value (in the simulations in Chapter 4, I used 0.2) and slowly decreased to 0 as the chain moves

along. Then, by Equation 1.14, the new set of parameter estimates is accepted whenever the $SRSS$ decreases; when the $SRSS$ increases, the new or current parameter estimates are accepted with a probability inversely dependent upon the magnitude of the increase in energy, as described by line 2 of Equation 1.14.

Simulated annealing requires starting parameter values, procedures for generating candidate parameter values, a convergence criterion and a cooling schedule. Simulated annealing initially searches the entire parameter space (because the initial value of the temperature T is chosen to be large), and as a result the choice of starting values is usually of little consequence (a major advantage of the method). Step size and direction are more difficult problems. In the implementation of simulated annealing used in Chapter 4, the approach used is to move round-robin through the parameters, fixing all but one and perturbing that one by a value taken from a Cauchy probability distribution centered at the current estimate. The Chapter 4 implementation uses a separate probability distribution for each parameter, and adaptively adjusts standard deviations to maintain an equal number of generated uphill and downhill steps.

Theoretically, for guaranteed convergence to the global minimum, simulated annealing requires a logarithmic decline of temperature that is too slow for use in real applications [76]. Probably the most frequently used annealing schedule runs for a predetermined number of iterations at a given temperature before reducing the temperature by some fixed factor. However, even this faster schedule may require a very long time to convergence. A considerably faster annealing schedule is used in Chapter 4, where after each single round-robin parameter update, the temperature is lowered by a fixed factor. The parameter chain is said to have converged when the $SRSS$ changes by less than some preset value over a specified number of consecutive round-robin cycles. Although the accelerated cooling schedule and the possible violation of smoothness conditions fail to ensure convergence by theory, a reasonably slow cooling schedule almost always converges to the global minimum [77]. Similar to the simplex method, it is important to verify that simulated annealing could not find a better solution by restarting the procedure (with the original, high temperature T) from the current parameter estimates.

1.3.4 Estimation of Covariate Effects

In evoked potential experiments, researchers present stimuli to human subjects and record the brain electrical response at one or more scalp electrodes. Such experiments are usually designed to study changes in the brain response to the stimulus as a function of stimulus characteristics, drug states, and other covariates. Researchers typically estimate covariate effects by identifying peaks in plots over time of the averaged potentials, then determining the amplitudes (height of the peak responses) and latencies (lags from the presentation of the stimulus to the peak responses) of the peaks, and applying traditional statistical methods such as analysis of variance to these derived measurements.

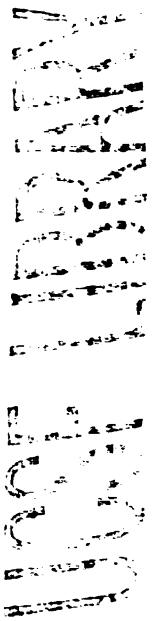

Another commonly used method of estimating covariate effects involves principal components analysis [80, 81] of the waveforms. However, when principal components analysis is applied to simulated data sets with multiple underlying components overlapping in time, it produces factors that do not always accurately reflect the true covariate effects of the underlying components [82, 83].

The spatio-temporal dipole model of Scherg [63] does not include the estimation of covariate effects for subject and experimental conditions. He fits dipoles to each evoked potential average, constraining the dipole locations (and sometimes orientations) to be fixed over time, then solves for the dipole magnitudes over time. This is the same problem I detailed under Section 1.3.2.

Turetsky, Raz, and Fein [10] suggested estimating covariate effects within the context of a time domain dipole model of multichannel evoked potential data. They assumed that the evoked potential averages from several subjects or from several conditions were generated by the same equivalent electrical dipole sources in the brain *across* all subjects or experimental conditions (i.e., the dipole sources had the same locations, orientations, and time-varying "shapes" across subjects or conditions). It is reasonable to assume that the evoked potential averages from several conditions recorded from the same subject are generated by the same sources. This assumption is probably violated across subjects, and a more reasonable model would allow for some small variability in dipole locations across subjects. The time-varying dipole

magnitude function was approximated by a decaying sinusoid (see Equation 1.11), and parameters were included to represent covariate effects on the delay to onset and the amplitude of this function. Raz, Cardenas, and Fletcher [65] proposed estimating covariate effects within the context of a frequency domain dipole model of multichannel evoked potential data. They also assumed that the averages from several subjects or conditions were generated by the same equivalent electrical dipoles *across* all subjects or conditions. The dipole magnitude function was approximated in the frequency domain by Fourier coefficients, and included parameters estimating the covariate effects on amplitude and latency. I will review both covariate estimation models in this section.

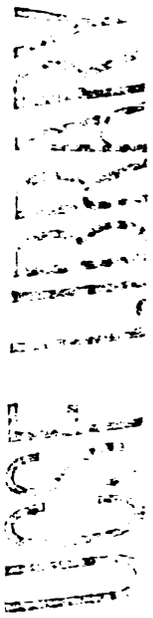

Time Domain Estimation of Covariate Effects

Letting s index subjects, I can write an expression for the scalp recorded voltage at time t due to a single dipole in the time domain as follows:

$$\mathbf{V}_t^s = \mathbf{f}(\boldsymbol{\theta}, \boldsymbol{\phi}) p_t^s \tag{1.15}$$

where $\mathbf{V}_t^s$ is an $n \times 1$ vector of voltages recorded at n measurement locations at time t from subject s, $\mathbf{f}(\boldsymbol{\theta}, \boldsymbol{\phi})$ is an $n \times 1$ vector valued function defined by Equation 1.9 for $k = 1, \ldots, n$, and p_t^s is defined as

$$\begin{aligned} p_t^s &= d^s p_t \\ &= d^s \alpha sin[\frac{2\pi}{\lambda}(t - \tau - \tau^s)] exp(-\beta(t - \tau - \tau^s)) \end{aligned} \tag{1.16}$$

In Equation 1.16, α is the magnitude of the "common" dipole (the dipole shared by all subjects), d^s is a subject specific amplitude weight (representing the subject covariate effect on amplitude) and τ^s is a subject specific latency jitter (representing the subject covariate effect on latency). To ensure uniqueness, the subject weights d^s are scaled to have a product of 1, and the latency shifts τ^s are adjusted to have a mean of 0 for each dipole. Alternatively, I can scale p_t such that $\| \mathbf{p} \|_\infty = 1$ (where

$\| \mathbf{p} \|_\infty = max|p_t| \ \forall \ t)$ and place no constraints on the d^s. For the case of using a decaying sinusoid for p_t, this is easily accomplished by setting α to 1.

Differences in the scalp recorded voltages across experimental conditions can be modeled in a similar fashion. Letting e index experimental conditions, I can write:

$$\mathbf{V}_t^{se} = \mathbf{f}(\boldsymbol{\theta}, \boldsymbol{\phi}) p_t^{se} \tag{1.17}$$

where $\mathbf{V}_t^{se}$ is an $n \times 1$ vector of voltages recorded at n measurement locations at time t from subject s during experimental condition e, and p_t^{se} is defined as

$$\begin{aligned} p_t^{se} &= d^s d^e p_t \\ &= d^s d^e \alpha sin[\frac{2\pi}{\lambda}(t - \tau - \tau^s - \tau^e)] exp(-\beta(t - \tau - \tau^s - \tau^e)) \end{aligned} \tag{1.18}$$

In Equation 1.18, d^e represents the experimental condition covariate effect on amplitude and τ^e represents the experimental condition covariate effect on latency. As before, the experimental condition weights d^e are scaled to have a product of 1, and the latency shift τ^e are adjusted to have a mean of 0 for each equivalent dipole.

When the covariate dipole model described in Equation 1.15 is fit over v subjects, nine common parameters are estimated (three location [$\boldsymbol{\theta}$], two orientation [$\boldsymbol{\phi}$], and four time-varying moment function parameters [$\alpha, \lambda, \tau, \beta$]), v amplitude parameters are estimated, and v latency parameters are estimated. This is a total of $9 + 2v$ parameters per dipole. A nonlinear optimization procedure could be used to estimate all parameters, or the amplitude parameters could be estimated linearly and all other parameters estimated nonlinearly. The dipole model described in Equation 1.17 can be solved in a similar fashion.

For the case of estimating the auditory P50 conditioning-testing ratio, the model described in Equation 1.15 is used, only that d^e are estimated instead of d^s. There are $v = 2$ experimental conditions. Let d^a be the covariate effect on the testing amplitude, and let d^b be the covariate effect on the conditioning amplitude. After dipole modeling is completed, the C-T ratio is simply,

$$\begin{aligned} \text{C-T ratio} &= \frac{d^a \alpha}{d^b \alpha} \\ &= \frac{d^a}{d^b} \end{aligned}$$

It is worthwhile to note that Equations 1.15 and 1.17 can both be extended to multiple dipoles by simply summing over all dipoles. Letting l be the number of dipoles, I can write

$$\mathbf{V}_t^{se} = \sum_{j=1}^{l} \mathbf{f}_j(\boldsymbol{\theta}_j, \boldsymbol{\phi}_j) p_{jt}^{se}$$

where $\mathbf{f}_j(\boldsymbol{\theta}_j, \boldsymbol{\phi}_j)$ is the weighting vector for dipole j at location $\boldsymbol{\theta}_j$ and orientation $\boldsymbol{\phi}_j$, and p_{jt}^{se} is the time-varying magnitude function for dipole j, subject s, condition e, and time t.

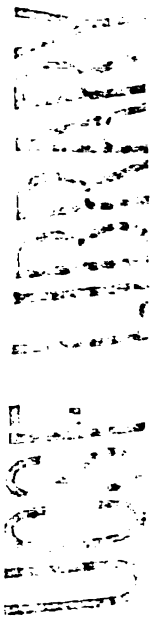

Frequency Domain Estimation of Covariate Effects

For simplicity, I will first describe the model in the time domain and then derive the frequency domain representation. The evoked potential stimulus is assumed to be presented in m trials indexed by i, and $\mathbf{V}_i(t)$ is an $n \times 1$ vector of recorded electrical potentials at time t. There are assumed to be u time points, and l dipoles generating $\mathbf{V}_i(t)$. In the time domain, the model has the form

$$\begin{aligned} \mathbf{V}_i(t) &= \sum_{j=1}^{l} exp(\mathbf{d}_j^T \mathbf{z}_i) \mathbf{f}_j(\boldsymbol{\theta}_j, \boldsymbol{\phi}_j) p_j(t + \boldsymbol{\tau}_j^T \mathbf{z}_i) + \mathbf{e}_i(t) \qquad (1.19) \\ i &= 1, \ldots, m \\ t &= 1, \ldots, u \end{aligned}$$

where $p_j(t)$ is the time-varying dipole moment of dipole j at time t, $\mathbf{d}_j$ and $\boldsymbol{\tau}_j$ are parameter vectors representing the covariate effects on the amplitude and latency of the response of generator j, $\mathbf{z}_i$ is a vector of covariates, and $\mathbf{e}_i(t)$ is a mean zero noise process. It is assumed that $\mathbf{e}_i(t)$ is a stationary, mixing, random process, and that $\mathbf{e}_i(t)$ is independent of $\mathbf{e}_{i'}(t)$ for $i \neq i'$.

In the case of fitting the dipole model to the auditory P50 collected in a conditioning-testing paradigm, the trials are grouped according to the values of the covariate, and there are only a few distinct values of $\mathbf{z}_i$. The responses to the first click can be grouped (for analysis purposes) into the first m_1 trials, and the responses to the second click can be grouped into the next m_1 trials. Therefore, $\mathbf{z}_i$ can be defined as follows:

$$\mathbf{z}_i = \begin{cases} 1/2 & \text{for } i = 1, \ldots, m_1 \\ -1/2 & \text{for } i = m_1 + 1, \ldots, m \end{cases} \tag{1.20}$$

The model is made identifiable by constraining $\Sigma_i \mathbf{z}_i = 0$. This means that the product of the amplitude effects is one, and the sum of the latency effects is zero.

The time domain model described in Equation 1.19 can now be transformed to the frequency domain. Let $\mathbf{V}_{i\mathcal{F}}$, $P_{\mathcal{F}j}$, and $\mathbf{E}_{i\mathcal{F}}$ be the discrete Fourier transforms at frequency $\gamma_{\mathcal{F}} = 2\pi\mathcal{F}/u$ of $\mathbf{V}_i(t)$, $p_j(t)$, and $\mathbf{e}_i(t)$. Then the frequency domain representation of the model has the approximate form:

$$\begin{aligned} \mathbf{V}_{i\mathcal{F}} &= \sum_{j=1}^{l} exp(\mathbf{d}_j^T \mathbf{z}_i + i\gamma_{\mathcal{F}} \boldsymbol{\tau}_j^T \mathbf{z}_i) \mathbf{f}_j(\boldsymbol{\theta}_j, \boldsymbol{\phi}_j) P_{\mathcal{F}j} + \mathbf{E}_{i\mathcal{F}} \\ i &= 1, \ldots, m \\ \mathcal{F} &= 1, \ldots, w \end{aligned} \tag{1.21}$$

where $w < u/2$ is the number of Fourier frequencies that are included in the analysis. The value of w is chosen using prior knowledge of the smoothness of the evoked potential.

Equation 1.21 shows that the latency parameters $\boldsymbol{\tau}_j$ are separated from the Fourier coefficients $P_{1j}, \ldots, P_{wj}$ in the frequency domain model, while in the time domain model described in Equation 1.19 the parameter $\boldsymbol{\tau}_j$ is included in the argument of the magnitude functions $p_j(\cdot)$. This greatly facilitates estimation of the latency parameters.

For the case of estimating the auditory P50 conditioning-testing ratio, $\mathbf{z}_i$ are defined as in Equation 1.20, and I let $l = 1$ in Equation 1.21 (i.e., fitting a single

dipole to the P50). Because there is only an experimental condition covariate (i.e., I do not need a covariate to describe changes between subjects because I am fitting on a single subject), the parameter vectors $\mathbf{d}$ and $\boldsymbol{\tau}$ become scalars d and τ, and $\mathbf{z}_i$ becomes a scalar z_i. A nonlinear optimization algorithm is then used to fit the dipole parameters. There are three location parameters ($\boldsymbol{\theta}$), two orientation parameters ($\boldsymbol{\phi}$), one parameter describing the covariate effects on amplitude, one parameter describing the covariate effects on latency, and w Fourier frequency ($P_{1j}, \ldots, P_{wj}$) parameters to estimate ($7 + w$ total parameters).

Once dipole modeling is completed, the C-T ratio is simply

$$\begin{aligned}
\text{C-T ratio} &= \frac{e^{(z_i=m_1+1,\ldots,m)d}(\gamma_1 + \ldots + \gamma_w)}{e^{(z_i=1,\ldots,m_1)d}(\gamma_1 + \ldots + \gamma_w)} \\
&= \frac{e^{-0.5d}(\gamma_1 + \ldots + \gamma_w)}{e^{0.5d}(\gamma_1 + \ldots + \gamma_w)} \\
&= e^{-0.5d} - e^{0.5d} \\
&= e^{-0.5d-0.5d} \\
&= e^{-d} \qquad (1.22)
\end{aligned}$$

As shown in Equation 1.22, if the amplitude d is correctly estimated, that is equivalent to correctly estimating the C-T ratio.

1.4 Intraclass Correlation Coefficient

All evoked potential analyses methods (peak-picking amplitude and latency measurement, principal components analysis, topographic mapping, dipole modeling) involve measurement error, in large part due to the noise still remaining in the averaged evoked potential. Measurement error complicates subsequent statistical analyses and interpretation, and therefore it is necessary to quantify the consistency of a given measurement by determining its reliability, r_{xx}, defined as the correlation between two equivalent measures of the same variable. The square root of r_{xx} may be interpreted as the correlation between the value of the variable as measured and its true value, allowing one to assess the efficacy of a particular measurement method [84].

Reliability of a given measurement is often measured by intraclass correlation coefficients (ICCs). Since different forms of the ICC produce different reliability results when applied to the same set of data, it is important to understand the sources of noise in each measurement in order to choose the appropriate ICC. For a more complete discussion of ICCs, see [85]. The statistical model I have used in Chapter 2 to determine the reliability of the dipole modeling estimates of covariate effects follows.

I wish to determine the reliability of auditory evoked P50 suppression over several replications, in either several subjects or in one subject over different clinical states or conditions. Thus there are m classes (representing subjects or conditions) and n P50 measurements (C-T ratios) per class. Let x_{ij} denote the ith rating ($i = 1, \ldots, n$) on the jth class ($j = 1, \ldots, m$). The following model for x_{ij} is then assumed:

$$x_{ij} = \mu + b_j + w_{ij} \tag{1.23}$$

where μ is the overall population mean (of the C-T ratio, in this example), b_j is the difference from μ of the jth class's true mean (i.e., the true P50 suppression of the subject during cocaine withdrawal or the jth subject's true P50 suppression), and w_{ij} is the error term, which encompasses the inseparable effects of measurement error and variability within a class. The component b_j is assumed to be normally distributed with mean 0 and variance σ^2_{bc}. The component w_{ij} is also assumed to be normally distributed with mean 0 and variance σ^2_{wc}. Both components are assumed to be independent of all other components in the model. The population ICC is then $\rho = \sigma^2_{bc}/(\sigma^2_{bc} + \sigma^2_{wc})$ and the quantities σ^2_{bc} and σ^2_{wc} can be estimated from quantities computed in a one-way ANOVA, as shown in Table 1.1.

The sample ICC (r) estimates the population ICC (ρ) and is computed as follows:

$$r = \frac{MSB - MSW}{MSB + (n-1)MSW} \tag{1.24}$$

A large value of r indicates that the variability between class measurements is greater than the variability within subjects, i.e. that repeated measurements within

Table 1.1: Analysis of variance for a reliability model

Source of variation	Degrees of freedom	Sum of squares	Mean square	Mean square estimates	F
Between classes	$m-1$	SSB	$MSB = \frac{SSB}{m-1}$	$n\sigma_{bc}^2 + \sigma_{wc}^2$	$\frac{MSB}{MSW}$
Within classes	$m(n-1)$	SSW	$MSW = \frac{SSW}{m(n-1)}$	σ_{wc}^2	
$SSB = \sum_{i=1}^{m} n(\bar{x}_{i.} - \bar{x}_{..})^2$			$SSW = \sum_{i=1}^{m}\sum_{j=1}^{n}(x_{ij} - \bar{x}_{i.})^2$		
$\bar{x}_{i.} = \sum_{j=1}^{n} \frac{x_{ij}}{n}$			$\bar{x}_{..} = \sum_{i=1}^{m}\sum_{j=1}^{n} \frac{x_{ij}}{mn}$		

a given class show stability. It is clear from Equation 1.24 that r approaches 1 as reliability increases. The *population* intraclass coefficient, ρ, ranges from 0 to 1 [86], but the estimator r described above might be negative if ρ is small and the measurements x_{ij} are noisy.

In this dissertation, I am interested in the test $H_0 : \rho \leq \rho_0$ versus $H_1 : \rho > \rho_0$. This test is performed as described by Donner and Eliasziw [87]. Accept $H_1 : \rho > \rho_0$ if $F > CF_{\alpha;\nu1,\nu2}$, where F is the value shown in Table 1.1 and $F_{\alpha;\nu1,\nu2}$ is the tabular value of the F distribution with $\nu1, \nu2$ degrees of freedom at the α per cent level of significance. The between classes degrees of freedom and the within classes degrees of freedom correspond to $\nu1, \nu2$, respectively. The constant C is defined by:

$$C = 1 + \frac{n\rho_0}{1 - \rho_0}$$

1.5 Summary

This introductory chapter has introduced evoked potentials, dipole modeling, linear estimation, nonlinear estimation, the estimation of covariate effects on evoked potential amplitude and latency, and the intraclass correlation coefficient.

Most of these topics are integrated in the next chapter, where I describe an application of dipole modeling of auditory P50 evoked potentials.

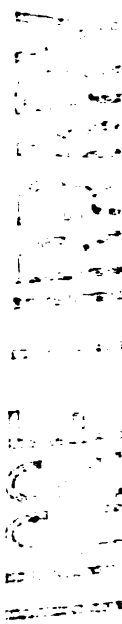

Chapter 2

The Reliability of Auditory P50 Suppression as Measured by the Conditioning-Testing Ratio is Improved by Dipole Modeling

2.1 Introduction

The phenomenon of P50 suppression has received increasing attention from psychiatric researchers in recent years. In normal subjects, suppression of the auditory P50 evoked response to the second of two paired clicks occurs when the interstimulus interval is less than 1 sec [88, 89, 16, 17]. The first (conditioning) click is thought to activate an inhibitory mechanism, causing a reduced response to a test click presented while the inhibitory mechanism is active. The degree of suppression of the test response is typically measured by the ratio of P50 amplitude to the testing versus conditioning click, called the C-T ratio. In normal subjects, at an interclick interval of 500 ms, the C-T ratio is usually less than 0.5 [18, 90]. Under the same conditions in schizophrenics, the response amplitude to the test stimulus is comparable or only slightly suppressed as compared to the conditioning stimulus, resulting in C-T ratios close to 1.0 [90]. This reduced or absent P50 suppression has been hypothesized by

Freedman and colleagues to reflect a preattentive, or neuronal impairment of auditory sensory gating [20, 91].

The clinical utility of the auditory P50 suppression measure is under question because of its low test-retest reliability. Kathmann and Engel [24] measured P50 suppression twice in 9 normals and 6 schizophrenics. They found very unstable C-T ratios, with reliabilities of 0.11 in the normals and -0.22 in the schizophrenics. Similarly, Boutros and colleagues [23] found a C-T ratio reliability of 0.14 across six replications in 10 normal subjects. The low reliability of the C-T ratio severely limits its utility as a tool for characterizing sensory gating in individual subjects, and precludes longitudinal studies examining the association between sensory gating and clinical variables.

The reliability of a measure such as P50 suppression is a function of: (a) the consistency within individuals over time of the "true" underlying phenomena, which the measure is supposed to capture, and (b) the contributions of measurement error (i.e., noise), which result in the measured phenomena differing from the "true" phenomena. Analysis of how P50 is measured provides insight into possible contributions of measurement error to its unreliability. In all studies to date, P50 amplitudes to the conditioning and testing stimuli are estimated independently via picking peaks on the vertex recordings, either as simple amplitudes, or as amplitude differences between a vertex peak and the prior (i.e., N40) vertex trough. The estimated P50 amplitude to each response is a function of the true P50 response and the noise in the average evoked potential (EP) at the time point(s) at which it was measured. The noise arises from the amplifiers, from the background electroencephalogram (EEG) and from muscle activity (the electromyogram [EMG]). With the conditioning and testing stimuli separated by 500 ms, the noise in the average EPs at the times of the P50 responses to the conditioning and testing stimuli are for the most part independent. Given the independent noise of the two measurements, taking their ratio augments the effect of the noise on the ratio. The distribution of the C-T ratio and simulations of the effect of computing the ratio on the signal-to-noise ratio is shown below in Section 2.2. The noise augmentation results in a reduced signal-to-noise ratio (SNR) of the C-T ratio as compared to the SNR of each of the conditioning and

testing stimuli. This analysis suggests two possibilities for increasing the reliability of the C-T ratio measurement. The first is to increase the SNR of the measured P50 response to each of the conditioning and testing stimuli. The second is to develop a measurement paradigm wherein the noise from the conditioning and testing P50 response measurements do not make independent (and therefore augmenting) contributions to the noise of the C-T ratio.

The Dipole Components Model (DCM) [10] may meet both goals for increasing the reliability of the C-T ratio. The DCM assumes that the conditioning and testing P50 responses arise from the same underlying brain process (assumed to be a point dipole source), and simultaneously fits a single dipole source to both responses. The amplitude of the dipole source is allowed to vary across conditioning and testing responses, with the ratio of the corresponding amplitude parameters yielding the C-T ratio. In such modeling, the noise at the two responses is pooled and makes only an averaged contribution to the C-T ratio. Furthermore, the dipole parameters are estimated using topographic data from multiple electrodes and multiple time points. To the degree that topographic information helps define the P50 dipole source, there is the potential for the P50 dipole magnitude to be measured with higher SNR than P50 amplitude measured from a single electrode. However, it is important to note that the DCM procedure is crude and simple. As examples, it models the head as a homogeneous sphere, the P50 sources as single point dipoles, and the dipole magnitude response as a decaying sinusoid. Given this acknowledged model misspecification, there is the real possibility that dipole modeling of P50 in a conditioning-testing paradigm might be very poor, adding unwanted noise to the measurements and resulting in even lower C-T ratio reliabilities than those derived from simple peak picking on vertex recordings. The goal of this research was to determine whether use of the DCM increases the reliability of the P50 suppression C-T ratio.

2.2 Theory

This section will demonstrate that, given independence of the C and T measurements, the signal to noise ratio (SNR) of the C-T ratio is generally diminished in comparison to the SNR of either the C or T response. This will be demonstrated by: (1) an analytical examination of the density function of the ratio of independent, normally distributed, random variables; and (2) simulation of the distribution of the C-T ratio (the C and T responses are assumed to be independent with square root distribution).

2.2.1 Analytic

Geary [92] showed that if X_1 and X_2 are independent, normally distributed random variables with mean 0 and variance 1, their ratio follows the Cauchy distribution. For those unfamiliar with the Cauchy distribution, it is just the t distribution with 1 degree of freedom. As practitioners will know well from testing hypotheses and/or calculating confidence intervals from small samples, the lower the degrees of freedom of the t, the more heavy-tailed it is, that is, the lower its SNR. Marsaglia [93] considered independent normal variates with no restriction on their means and variances, and showed that if f is the density of X_1/X_2 and g is the Cauchy density, then for $x \geq 0$,

$$f(x) \geq c_1 g(x)(1 + c_2) \tag{2.1}$$

where $c_1 > 0$ and $c_2 \geq 0$ are constants. Therefore, the second moment of X_1/X_2, $E^2(X_1/X_2)$, is infinite, because

$$\begin{aligned} E^2(X_1/X_2) &= \int_{-\infty}^{+\infty} x^2 f(x)dx \\ &\geq \int_{0}^{+\infty} x^2 f(x)dx \\ &\geq c_1 \int_{0}^{+\infty} x^2 g(x)dx \\ &\geq \infty \end{aligned}$$

and the last integral is infinite because the second moment of the Cauchy distribution is symmetric and infinite [94].

Because the variance of a random variable equals its second moment minus the square of its mean, X_1/X_2 has infinite variance. Simply put, the quotient of two independent normals will be at least as heavy-tailed as the Cauchy distribution, and this in turn means that the population SNR of the ratio of independent normals approaches zero in the limit, and the sample SNR is small in comparison to the SNR of either component of the ratio.

2.2.2 Simulation

The analytic discussion above assumed X_1 and X_2 to be independently normally distributed variates. The C and T amplitudes are not normally distributed as they cannot be negative, and a normal distribution with the means and variances observed for the C and T responses of this chapter (see Section 2.4) would include negative amplitudes. Work be Sand [95] indicates that auditory brainstem response amplitudes, which are smaller than the P50, but also are bounded by zero amplitude, are well represented as square-root normal variates (i.e., their square roots are normally distributed). Because the analytic proofs in Section 2.2.1 do not necessarily hold for square-root normal variates, the simulation study was carried out assuming that the P50 responses are square-root normal variates, as follows:

1 Means and SD were computed for the conditioning and testing response amplitudes from the peak picking data used in this study. Therefore, the results from these simulations are directly applicable to this chapter.

2 Fifty samples of size 1000 each were drawn from a square-root normal distribution with (untransformed) mean 4.13 and SD 2.29 (group C).

3 Fifty samples of size 1000 each were drawn from a square-root normal distribution with (untransformed) mean 2.03 and SD 1.28 (group T).

4 The signal-to-noise ratio of the quotient of corresponding samples from Group C and Group T were computed (50 computations).

The results of these simulations are as follows:

$$\begin{aligned} \text{mean SNR of the quotient} &= 0.29 \\ \text{median SNR of the quotient} &= 0.27 \\ \text{range of SNRs of the quotient} &= (0.03, 0.76) \end{aligned}$$

Because the SNR of the C group is 1.80 (mean divided by the SD, also known as the coefficient of variation) and the SNR of the T group is 1.58, all simulated SNRs of the quotient of the measurement were diminished compared to the SNR of either the C group or the T group.

2.3 Methods

2.3.1 Overview

The goal was to determine the effects of dipole component modeling (DCM) on the reliability of the P50 suppression C-T ratio. The data collected and analyzed by Jerger et al. [96] were used. C-T ratio reliabilities were obtained by computing intraclass correlation coefficients (ICCs) [85], and the ICCs were compared as described by Donner and Eliasziw [87]. The methods used here were discussed in Section 1.4.

2.3.2 Subjects

Twelve subjects, six women and six men, with no history of drug or alcohol abuse or a family history of neurologic or psychiatric disorder, were studied. Subjects were between 23 and 29 years of age, were free of medication at the time of the study, gave informed consent, and were paid for their participation.

2.3.3 Recording Methods

Subjects were relaxed, awake, and seated upright in a quiet room during the recording sessions. Recordings were made using 14 tin EEG electrodes in an electrode cap (Electro-Cap International, Eaton, OH) and referenced to a tin electrode

clipped to the left ear. The electrode locations corresponded to the International 10-20 System, and included Fz, Cz, Pz, Oz, Fpl, Fp2, F7, F8, T3, T4, C3, C4, T5, and T6. These electrode locations are shown in Figure 2.1. Vertical eye movements were monitored using gold electrodes above and below the right eye, and horizontal eye movements were monitored using electrodes placed at the lateral canthi. Impedances for cap electrodes were lowered using electrode gel (Electro-Cap International), and Grass EC2 Electrode Cream was used for the reference and electrooculogram (EOG) leads. Two kinds of electrode pastes were used because the Electro-Cap gel was too thin for use in the cup electrodes or ear clip, and the Grass cream was too thick for use in the electrocap. Although the differences in ion concentration in the two pastes can cause a very slowly varying potential difference, this electrical artifact should be filtered out by our analog filtering. All impedances were below 5000 ohms and signals were amplified 50,000 times by a Grass Model 12 Neurodata Acquisition System with analog filters at 0.1 and 1000 Hz. ERPSYSTEM Software (Neurobehavioral Laboratory Software, San Rafael, CA) was used to control stimulus presentation and data acquisition through an Analog Devices RTI 800-815/F laboratory interface card on a 20 MHz Intel 80386-based personal computer. Data were sampled at 2000 Hz and averaged for 250 ms beginning 50 ms prior to each click, for a total of 500 ms of data for each pair of clicks. Trials, consisting of pairs of clicks, were rejected if activity exceeded $\pm$ 70 μV on either eye-movement channel. Note that given the 2000 Hz sampling rate, the low-pass filter cutoff used in this study is less than ideal, and subsequent studies have utilized a 300 Hz low-pass filter cutoff.

2.3.4 Auditory Stimulation

Binaural clicks were produced by square pulses of 0.05 ms duration, which were generated by the Analog-Devices D/A converter, then passed though a Hewlett-Packard 350D Attenuator, amplified by a Pioneer SX-2300 stereo receiver/amplifier, and delivered to the subject over Realistic NOVA '20 headphones (Tandy Corporation, Houston, TX). In the original experiment [96], a selective attention paradigm using four combinations of clicks at two different intensities was designed. The experiment

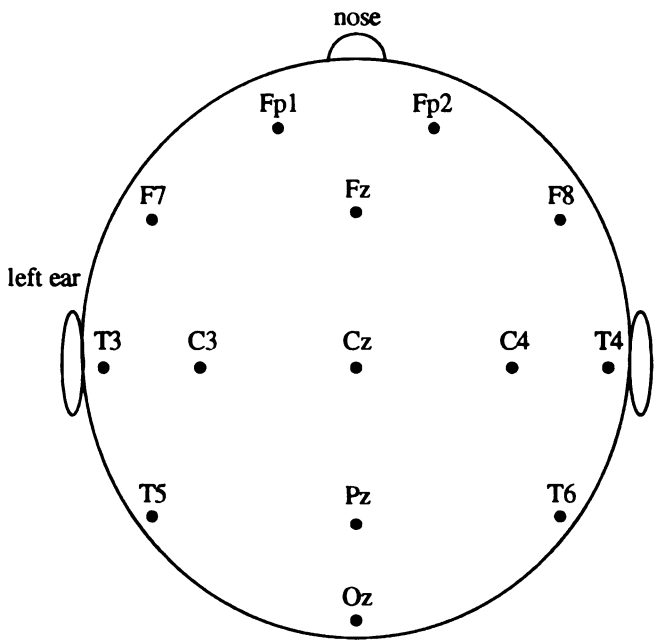

Figure 2.1: Electrode locations used for P50 study.

was conducted with the subject required to perform a task requiring attention to either the first or second click, as conveyed by the experimental instructions. Each of these two tasks was repeated on three different occasions on non-consecutive days by each subject. Jerger and colleagues [96] showed that the P50 was unaffected by the task, so for the purpose of this analysis (the Jerger data was analyzed in this chapter), all six runs (2 tasks $\times$ 3 replications) are considered replications. As in [96], only data from the high-intensity paired clicks (which had by far the largest number of trials) is examined. The high-intensity clicks were just over 76 dB above subject threshold, were separated by 500 ms, with the intertrial interval varying between 7 and 8 sec. Between 110 and 120 artifact-free trials were recorded during each run.

2.3.5 EP Waveform Analysis-Peak Picking

The average EPs were digitally bandpass filtered between 10 and 50 Hz (half amplitude cutoff frequencies). Because the dominant frequency constituents of the middle latency response range from 30 to 50 Hz [97] and the dominant frequency

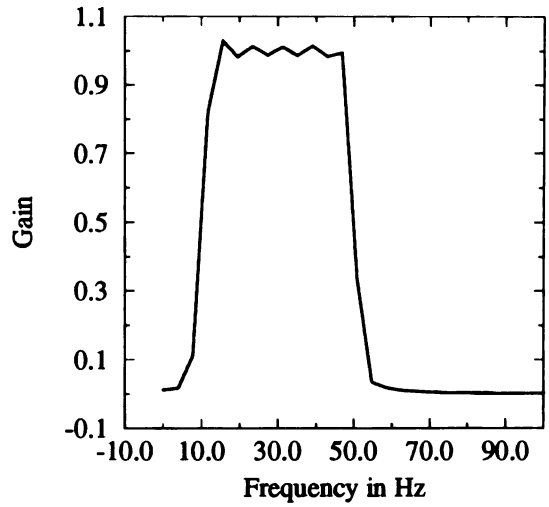

Figure 2.2: Frequency response of the 10-50 Hz digital bandpass filter.

constituents of the auditory N100/P200 are below 10 Hz, the digital filtering removed the majority of the auditory N100, P200, and 60 Hz noise, and allowed us to analyze the remaining P50 response (see [96] for a description of the filter construction). Figure 2.3.5 shows the frequency response of the digital bandpass filter.

P50 amplitude at the vertex electrode was measured relative to the preceding peak of negative polarity. The peak-picking algorithm of ERPSYSTEM was used to choose the peaks, and the peaks chosen were then verified with the help of an experienced rater (Christie Biggins). The peaks were chosen as the most positive (or negative) voltage value within a specific time range after the stimulus. The time window for the negativity preceding P50 was 30-50 ms, and the window for P50 was 40-80 ms. In no case did the algorithm choose a P50 that preceded the N40. In cases where the auditory P30 overlapped the P50 such that no clear N40 could be identified, the P50 amplitude was measured to the prestimulus baseline for the conditioning and testing stimuli within that pair. The C-T ratio was computed by dividing the amplitude of the testing response by the amplitude of the conditioning response.

2.3.6 EP Waveform Analysis-Dipole Modeling

A simple dipole model was simultaneously fit to both the conditioning and testing responses for each replication of each subject (i.e., 72 dipole localizations were performed, 12 subjects $\times$ 6 replications). The head was assumed to be a sphere of homogeneous conductivity (i.e., the differing conductivities of the skull, scalp, and brain were not considered). The P50 generator was assumed to be a single, point dipole with fixed location and orientation throughout its time of activation. The dipole activity over time was modeled as a decaying sinusoid with a fixed latency of onset in response to both clicks and with two (1 replication $\times$ 2 clicks) click-specific amplitude parameters [10]. We did not let latency differ in response to the conditioning and testing clicks, as previous analysis of these data (using peak picking) indicated no such latency differences [96]. The dipole model for the scalp recorded potential at electrode k at time t was:

$$V_{kt}^{e} = d^{e} p_t f_k(\boldsymbol{\theta}, \boldsymbol{\phi}) \text{ for } e = 1, 2 \tag{2.2}$$

where

$$p_t = \alpha sin[\frac{2\pi}{\lambda}(t-\tau)]exp[-\beta(t-\tau)] \tag{2.3}$$

and where d^e is the amplitude parameter for experimental condition e, and $f_k(\boldsymbol{\theta}, \boldsymbol{\phi})$ is the weighting function as defined in Equations 1.1-1.9.

The nonlinear simplex method (see Section 1.3.3 and [74, 66]) was used to estimate the dipole location, orientation, and decaying sinusoid parameters. This optimization algorithm is sensitive to starting values of the parameters, and when it is unsuccessful, either does not converge, or converges to a local minima rather than the absolute minima or best solution. This is a limitation of the simplex method, and although convergence was monitored, no attempt was made to verify that simplex converged to the global minimum in this experiment.

The DCM was applied to data within a time window to contain both the ascending and descending aspects of the P50 peak at the vertex. The starting point for the window over subjects ranged from 35-46 ms, and the window width ranged between 27-45 ms. In general, the vertex P50 within the window resembled one

half period of a sinusoid. The starting parameter for the wavelength of the decaying sinusoid function was set to twice the window width and the starting delay parameter was set to the zero crossing of the vertex potential relative to the onset of the window. The starting parameters were set to 0.0002 for sinusoidal decay, 3 (arbitrary units) for overall dipole amplitude, and 1 for each click-specific amplitude parameter (indicating no difference in P50 amplitude for the two clicks). The starting dipole location was the center of the head, and the starting dipole orientation was toward the nasion.

In addition to fitting a dipole to each replication separately, the DCM was used to fit a dipole over all six replications of each subject simultaneously (i.e., 12 dipole localizations were performed). As with the previous model, click-specific amplitude parameters were fit to describe the P50 amplitude differences (i.e., 12 click-specific amplitude parameters were fit, 6 replications $\times$ 2 clicks). This model has the advantage of constraining the dipole location to be the same within a subject across replications. The dipole model is the same as in Equation 2.2, except that $e = 1, \ldots, 12$.

2.3.7 EP Waveform Analysis-Decaying Sinusoid Modeling

As discussed in the introduction, if dipole modeling improved the C-T ratio reliability, the improvement may be due to a combination of: (1) pooling the noise from the conditioning and testing responses, (2) increasing the SNR for the conditioning and testing amplitude measures via modeling of the topographic response as an intracranial dipole source, and (3) chance. In order to determine the effect caused by pooling of noise and simultaneously fitting both P50 responses, we fit a model that pooled the noise while estimating the amplitude on the vertex channel alone, without using multiple channels or intracranial dipole constraints. To accomplish this, a decaying sinusoid was fit to the averaged and filtered EP data for the vertex electrode. A time window around the P50 peak was chosen as described above, and the conditioning and testing responses were fit simultaneously using the same nonlinear simplex algorithm as for the DCM. A decaying sinusoid with separate conditioning and testing amplitude parameters was fit for each run of each subject (72 analyses),

and also to all six runs for each subject. The windows and time function starting parameters were chosen as for the DCM above, and did not need to be adjusted for any of the analyses. As in the DCM analysis, the C-T ratio was computed by dividing the amplitude parameter for the testing response by the amplitude parameter for the conditioning response.

2.4 Results

The topography for the conditioning and testing responses to the auditory click is shown in Figure 2.3. One P50 average for one subject is shown. Clear separation of the P50 and P30 peaks can be seen in the vertex, C3, and C4 recordings. The remaining electrode sites show that the amplitude of the P50 is decreased at the surrounding electrodes, and a reversal of potential is seen at the lateral electrodes. This topographical distribution of potential is consistent with a dipole model of the P50 generator. All but one subject showed comparable potential topography. Figure 2.4 shows the conditioning and testing responses to the auditory click of a representative average of this subject. On the vertex recordings displayed on the left of Figure 2.4, P50 can be identified according to the peak picking rules; however, the remaining electrodes do not show a potential topography consistent with a P50 dipole.

Peak Picking: As noted above, according to our scoring rules, a P50 at the vertex electrode could be identified for all recordings. For three subjects the negativity preceding P50 was obscured by P30 on one or more of the six replications. For these data, P50 amplitude could only be measured relative to the prestimulus baseline. The C-T ratios derived from peak picking ranged from 0.01 to 1.66, with a mean of 0.53 and SD of 0.32. The ICC computed across all 6 replications was $r = 0.27$. If the subject displayed in Figure 2.4 is deleted from the computations, the ICC becomes 0.37.

Dipole Components Modeling: DCM was first independently applied to 6 replications for each subject. Although the simplex procedure always yielded an estimated dipole, this dipole did not always model what was apparently the P50 response at the vertex. An example of where the dipole modeling worked well is presented in

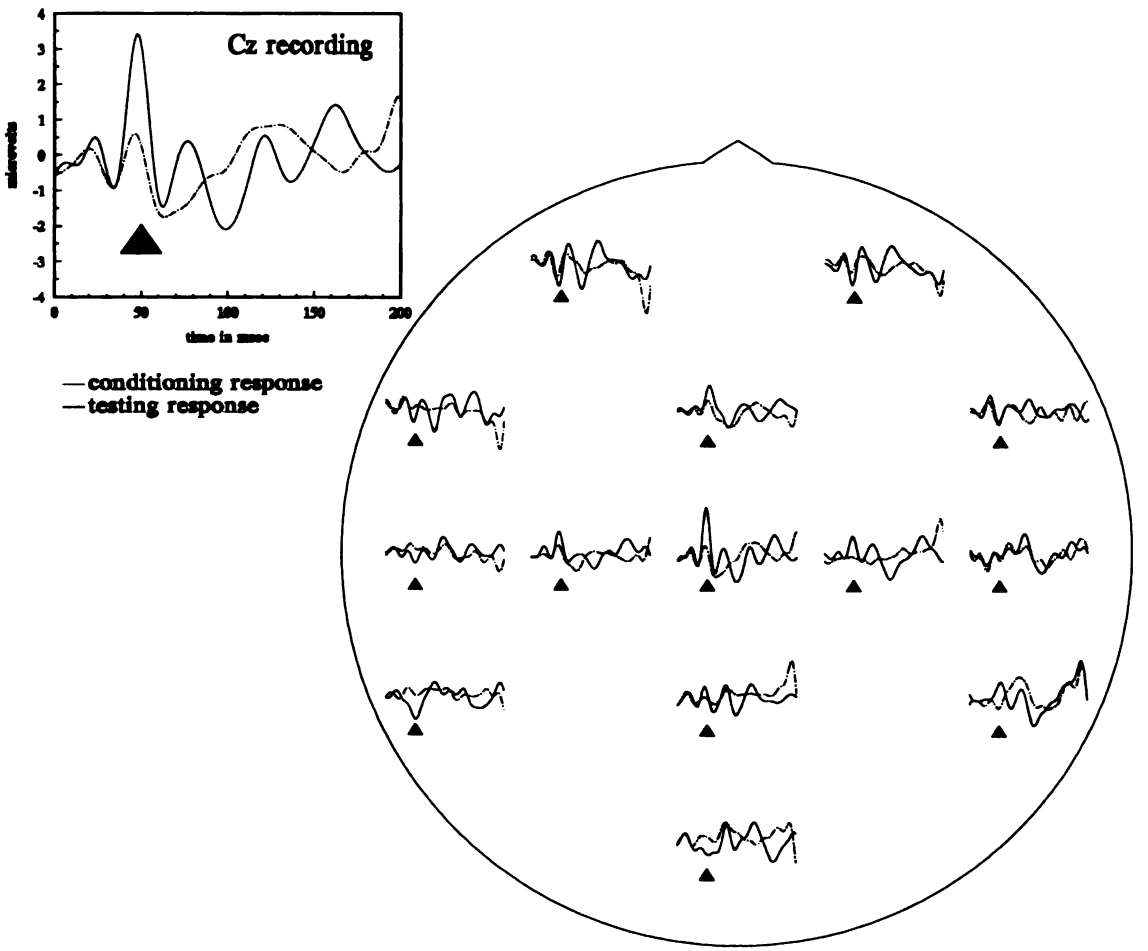

Figure 2.3: P50 Response to the Conditioning-Testing Paradigm
The topography of the P50 response for a representative subject is displayed for both the conditioning and testing stimuli. The responses measured at the vertex (Cz) (on which peak picking is usually performed) is shown at the top left. The testing response has similar topography to that of the conditioning response and is suppressed at most electrode sites. All but one subject had a similar P50 topography. Markers are displyed at 50 ms poststimulus.

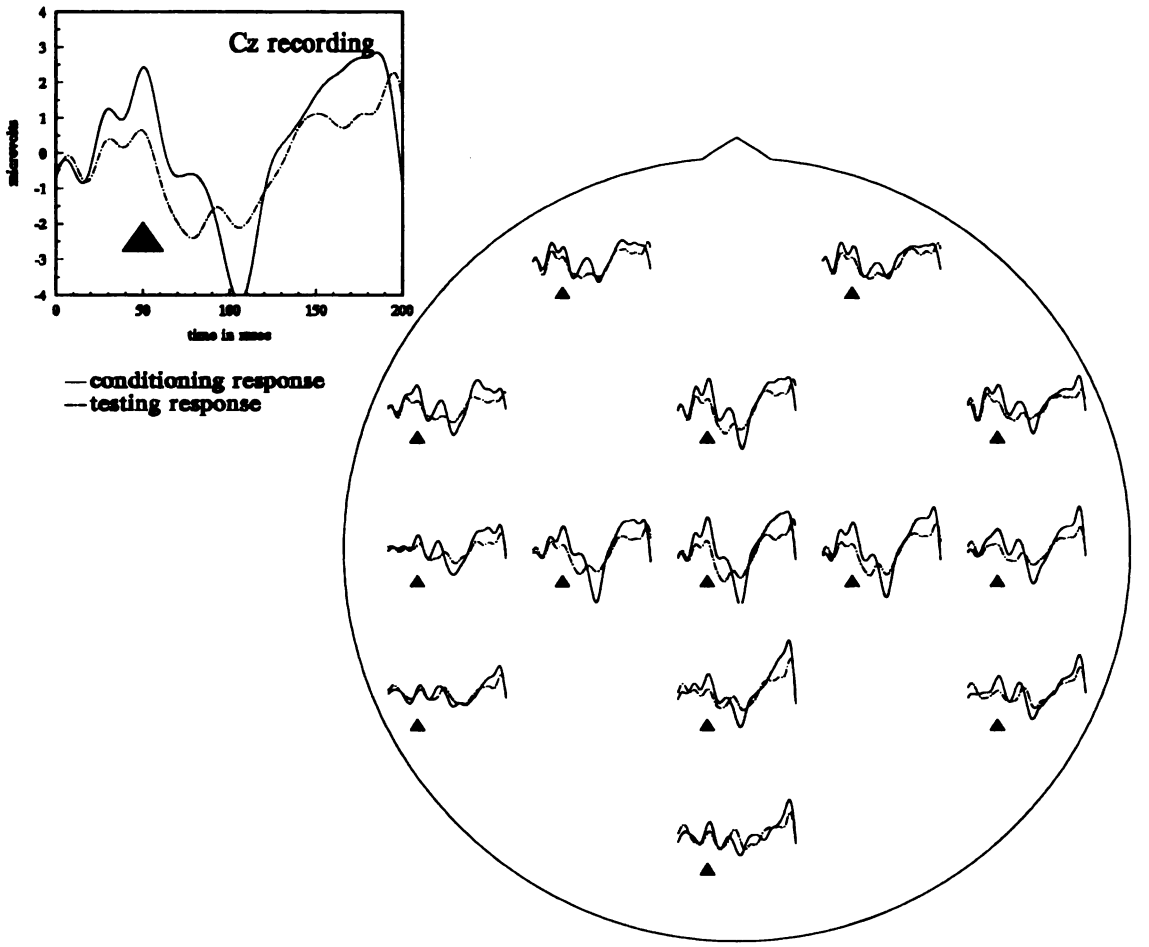

Figure 2.4: P50 Response to the Conditioning-Testing Paradigm: Excluded Subject The topography of the P50 responses is displayed for the one subject whose topography was dissimilar from that of the remaining subjects. Although P50 can be identified at Cz according to our peak picking rules (see graph at left), the topography shown at the right does not follow a typical P50 distribution, and dipole modeling was unsuccessful for this subject. Markers are at 50 ms poststimulus.

Figure 2.5. Note that the topography of the P50 response is modeled well by a single dipole; for contrast, compare the topography in Figure 2.4. For two subjects, there was significant activity in the analysis window at the F7 and F8 electrode sites such that the simplex algorithm primarily fit the activity at those electrode sites rather than at Cz. For these subjects, the F7 and F8 electrode sites were removed and the DCM was applied to the data from the remaining 12 electrode sites, which resulted in good fitting of the vertex P50. To determine whether the activity at F7 and F8 affected all the dipole fits, we redid them all with F7 and F8 removed. For three additional subjects, there was relatively poor fitting at Cz and surrounding electrodes because the simplex algorithm was drawn toward fitting earlier, but temporally overlapping higher amplitude activity at lateral electrode sites. Adjusting the analysis window to de-emphasize this earlier lateral activity resulted in much improved dipole fits at Cz. For one subject, the one displayed in Figure 2.4, nothing we did enabled us to model the activity at the vertex–this subject was removed from the dipole analysis. The C-T ratios were computed from the DCM results of 11 subjects by dividing the click 2 amplitude parameter by the click 1 amplitude parameter.

Using all 14 electrodes in the DCM, the proportion of variance accounted for by DCM ranged from 29% to 86% (mean $\pm$ SD, 58% $\pm$ 12%), yielding C-T ratios that ranged from 0.00 to 1.59 (0.44 $\pm$ 0.30). The ICC was 0.57, significantly larger than that obtained from peak picking of all 12 subjects ($p < 0.009$, comparing ICCs of 0.57 and 0.27). The difference between the ICC obtained from dipole modeling and the ICC obtained from peak picking of the 11 subjects for which DCM was satisfactory nearly reached significance ($p < 0.06$, comparing ICCs of 0.57 and 0.37). Eliminating F7 and F8 from the analysis, DCM accounted for between 36% and 89% of the variance (64% $\pm$ 12%), yielding C-T ratios that ranged from 0.00 to 1.94 (0.46 $\pm$ 0.36). This yielded an ICC of 0.63. This ICC was significantly greater than that obtained by peak picking for either 12 or 11 subjects ($p < 0.002$ and $p < 0.02$, respectively).

When DCM was applied simultaneously to all six runs for each subject, the resulting C-T ratios and ICCs were almost identical to those obtained when each run was fit separately.

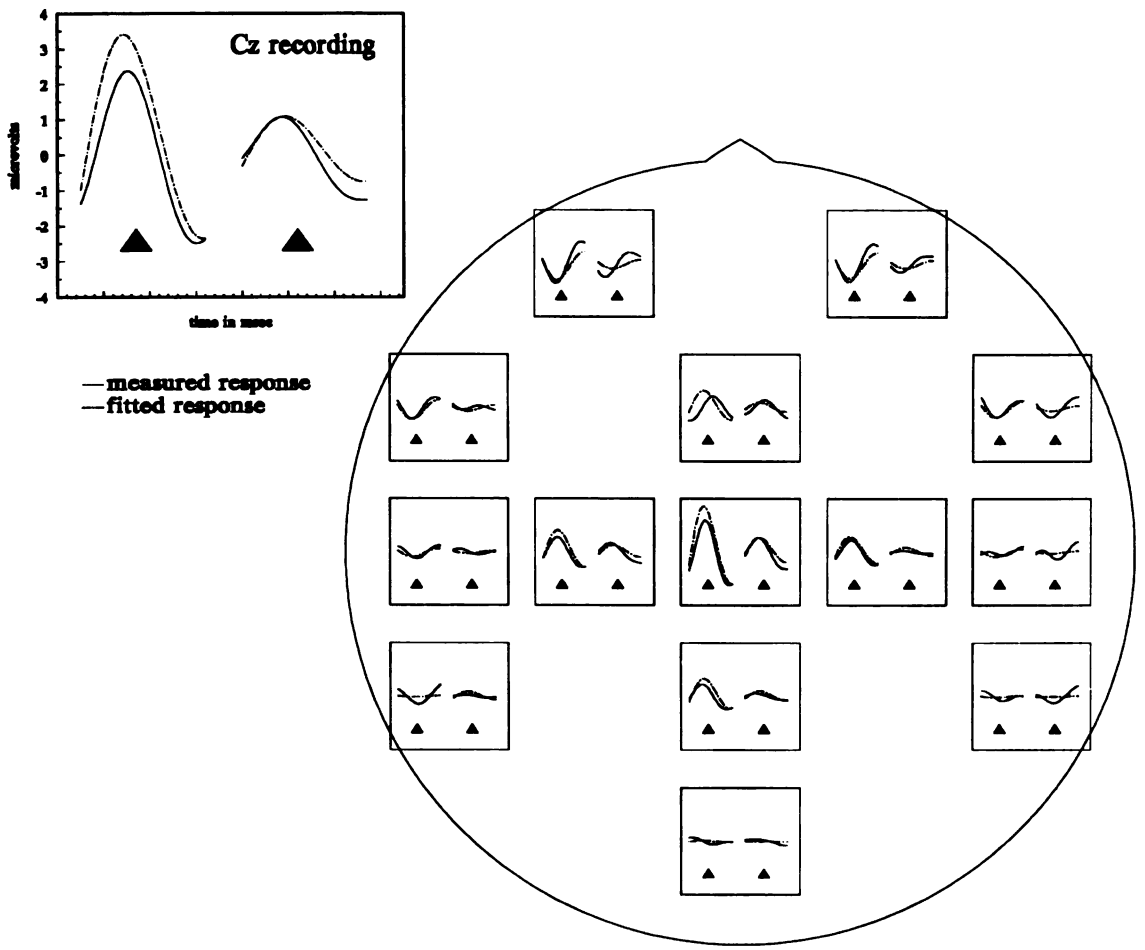

Figure 2.5: Dipole Modeling of P50 Response
The measured and fitted P50 responses to the conditioning and testing clicks for the same subject shown in Figure 2.3 are shown here. The best fitting dipole well describes the amplitude at Cz and across the head for both the conditioning and testing response.

Modeling of Vertex Data Using a Decaying Sinusoid: When a decaying sinusoid was fit to each run separately, resulting C-T ratios ranged from 0.02 to 1.04 (0.30 ± 0.20), with an ICC of 0.31. When all 6 replications for each subject were fit simultaneously, the results were almost identical.

2.5 Discussion

The auditory P50 response recorded using a conditioning-testing paradigm was modeled using a relatively simple dipole components model. This modeling resulted in a substantial and statistically significant increase in the reliability of the derived C-T ratio measure of P50 suppression in comparison to the C-T ratio measured by peak picking on vertex recordings. This result is potentially very important. It provides promise that P50 suppression can be measured with high enough reliability to be useful for characterizing sensory gating in individual subjects and for use in longitudinal studies examining the association between sensory gating and clinical variables.

It is important to emphasize that the results reported are not general for all dipole modeling algorithms, but are specific to the Dipole Components Model. Other dipole modeling procedures [1, 98] are not appropriate for this study, as they model each evoked potential separately and do not pool noise estimates across multiple event-related potential (ERP) recordings. Moreover, the application of other dipole modeling procedures to this data set is not straightforward. In the case of the instantaneous state dipole modeling approach [1], in which a dipole is fit to a single time point, the first question that must be answered is to which time point should the dipole be fitted? The simple answer is to use peak picking to choose the P50 peaks for both responses (this latency determination involves two sources of noise, as previously discussed), then to fit a dipole to each response (two more independent measurements, leading to two additional sources of noise). Scherg's approach [63] does not simplify matters either. Because BESA (Brain Electrical Source Analysis, Neuro-Scan, Inc) cannot fit a single dipole to the conditioning and testing responses simultaneously, the conditioning and testing responses would be modeled separately

(two sources of noise). In addition, as BESA does not use a parametric form for the dipole magnitude function, the dipole magnitude cannot be described by a single parameter, and the dipole magnitude function for the two responses may differ greatly. The C-T ratio is computed by dividing the testing response amplitude by the conditioning response amplitude, so in order to use Scherg's dipole magnitude, a single point of the magnitude function must be chosen to represent the P50 generator magnitude. How will this point be chosen? Again, the simple answer is to peak pick on the dipole magnitude function. Because the magnitude functions for the two responses are likely to be different, they must be peak picked separately, introducing two more sources of noise. In summary, although dipole modeling approaches *other* than the DCM are promising and their use of topographic information may lead to improved amplitude estimates, they do not address the issue of independent noise measurement and are therefore not appropriate for the C-T ratio reliability problem.

The range of C-T ratios obtained in this study using peak picking is wide, consistent with other studies [23, 90]. The range of C-T ratios obtained using dipole modeling was also wide, but the increased ICC indicates that the variability of C-T ratios within subjects has decreased relative to the variability of C-T ratios between subjects, and the wide range of dipole modeling C-T ratios is explained by differences between subjects. Dipole modeling provides a more stable C-T ratio within individuals.

Standard peak picking measures P50 amplitude relative to the preceding N40 component or other surrounding activity, and thus reflects variability and noise of both the P50 and the other activity. In contrast, DCM, as applied in this work, only models the P50 component. To determine whether this was a significant factor in the results reported here, the peak picking was redone versus a prestimulus baseline. The results were not appreciably affected. Note, however, that even this peak measurement method does not get away from the problem of confounding P50 activity with other (i.e., prestimulus) activity. Such is the reality of referential EEG recordings.

These results also provide some data on the best montage to use for dipole modeling of the P50 response. It is well known that EMG artifact from the temporalis,

frontalis, and posterior cervical muscles can contaminate middle latency auditory responses [99]. Although EMG artifact is relatively small at the vertex, recordings from electrodes that overlie the offending muscles are more susceptible to EMG artifact. In particular, this study observed that eliminating the F7 and F8 recordings increased the goodness of fit and the reliability of the dipole modeling.

Any model improvements could be tested using the methodology (i.e., testing model improvements by comparing the ICC between analyses using different models) of this chapter. It is important to note that although consistency is a cornerstone of usefulness, it does not prove validity. Of course, sometimes consistency can result from a methodological artifact. Such is not the case in the paradigm presented here where the consistency measure we used, the intraclass correlation coefficient, compares within and between subject variance of the C-T ratio. These two sources of variability could not have affected the DCM results differentially due to artifact because within and between subject variation was treated identically, with each repetition of P50 data analyzed independently.

The C-T ratio reliabilities computed from click-specific amplitude parameters obtained when all six runs were simultaneously included in the DCM were comparable to those obtained when the DCM was fit to each run separately. This result was surprising, since fitting over more replications would hypothetically increase the effective SNR, especially for estimation of dipole location and orientation, resulting in a more accurate modeling of the data. One possible explanation for this result may be that the electrode caps were not placed in exactly the same manner across days, introducing noise into the DCM.

These findings raise the possibility that P50 suppression can now be utilized to study individual subjects. Several studies have shown that the P50 C-T ratio is affected by diseases and drugs. For example, the C-T ratio is increased in schizophrenics compared to nonpsychotic controls [90, 100, 20, 91], in cocaine addicts compared to both normal controls and chronic alcoholics [101], and with normalization of schizophrenic P50 with nicotine administration [102, 103]. In all these studies, however, P50 suppression was examined only via group comparisons. If dipole modeling increases the reliability of the C-T ratio in these clinical populations as we have

shown that it does in normals, it will then be possible to relate the C-T ratio to clinical state variables. This would increase the power of studies of the effects of neuroleptics (or nicotine) on schizophrenic subjects and would make possible the examination of the possible modulating effects of clinical status variables. In studies of cocaine addicts, it would also facilitate longitudinal studies of the effect of various lengths of abstinence on P50 suppression. Before this promise can be realized, it is necessary to determine the reliability of P50 suppression in the appropriate clinical populations. It is possible that the underlying "true" P50 suppression phenomenon is less (or more) stable in such clinical populations than it is in normals. This is an empirical question and can only be resolved by analyzing replicate data in such populations using the DCM. This step is necessary to advance the understanding of the potential and limitation of the P50 suppression measure in those clinical populations.

It has yet to be explained how dipole modeling improved the reliability of the C-T ratio. As mentioned above, fitting across several runs did not lead to further improvements in C-T ratio reliability. The control experiment, during which a decaying sinusoid was fit to two responses simultaneously using a single channel only, did not lead to improved C-T ratio reliability, either. This seems to suggest that the dipole model and the use of multiple channels of data led to the improvement in C-T ratio reliability. If this is true, then the reliability of the conditioning and testing amplitudes should also be increased over the peak picking measures.

The reliabilities of the conditioning and testing peak amplitudes as measured by peak picking on 12 subjects were $r = 0.84$ and $r = 0.50$, respectively. The reliabilities of the conditioning and testing peak amplitudes as measured by dipole modeling were $r = 0.52$ and $r = 0.69$, respectively. These differences in reliability between peak picking and dipole modeling for both the conditioning and testing amplitudes were not significant, which implies that the dipole model and the use of multiple channels led to no improvement.

The observation that dipole modeling improved ratio reliability but not amplitude reliability despite using simplified head and time-varying magnitude functions leads to another hypothesis. Could it be that the misspecification of the dipole model (e.g., use of a homogeneous sphere head model, use of a decaying sinusoid magnitude

function, modeling a single generator) affects the estimation and variability of amplitude parameters, but has little effect of the ratios (i.e., does model misspecification *cancel* in a derived ratio measure?).

This paradox, that dipole modeling leads to improved C-T ratio reliability but not to improved conditioning and testing amplitudes, bears further investigation. The hypothesis that model misspecification cancels in a derived ratio measure must also be investigated. These questions will be addressed in Chapter 3.

In summary, this study shows that the reliability of P50 suppression can be made substantially greater than previously reported. Furthermore, this demonstrates that the Dipole Components Model can lead to increased reliability of evoked potential amplitude ratios. These findings have potentially very important implications both for further P50 studies in clinical populations and for future applications of Dipole Component Modeling.

Chapter 3

Theoretical considerations

3.1 Introduction

The previous chapter showed that dipole modeling led to more reliable estimation of amplitude ratios than did peak picking, but failed to lead to more reliable amplitude measurements. Research by Raz, Cardenas, and Fletcher helped to shed light on this apparent paradox.

Raz, Cardenas, and Fletcher [65] extended the frequency domain dipole model to include estimation of covariate effects, as described in Section 1.3.4. Recall that in the frequency domain model, the time-varying dipole magnitude is estimated by Fourier coefficients. They tested the efficacy of the model by simulating evoked potential data designed to resemble auditory P50 as recorded in a conditioning-testing paradigm. In this paradigm, the EP in response to the second of paired clicks is reduced in amplitude relative to the response to the first click. The simulated noise was averaged spontaneous EEG and the SNR was varied to construct data sets with low and high SNRs. Simulated data were generated using two head models: (1) a spherical model of homogeneous conductivity, and (2) a realistic skull shape model of homogeneous conductivity. Data were generated using either one dipole or two bilateral, synchronously active dipoles. The estimation procedure always assumed a single dipole generator in a spherical head.

The results demonstrated that the estimators of the covariate effects on

amplitude (which are essentially ratio estimates for the frequency domain model, as shown in Section 1.3.4, Equation 1.22) and latency performed well even when the method, which assumed a spherical head, was applied to simulated data generated from a realistic head shape. Additionally, the estimators performed well even when the data were generated by two dipoles but were fit with a single dipole. As expected, the location and orientation estimators were essentially unbiased when applied to data generated in the spherical model, and biased when applied to data generated in the realistic head shape model.

These results led me to suspect that the errors (i.e., bias) in the estimates of the covariate effect on amplitude (estimated using dipole modeling) caused by model misspecification "canceled" when a ratio was computed. These suspicions led to me to confirm the empirical results theoretically, as described in this chapter.

I also hypothesized that model misspecification led to more variable amplitude estimates as compared to ratios, which in turn would lead to less reliable amplitude estimates (as measured by the ICC) as compared to ratios. I will examine this hypothesis later in this chapter.

I am interested in determining errors due to model misspecification when dipole modeling (via minimization of a least squares criterion, such as the scaled residual sum of squares, defined in Section 1.3.3) is used to estimate covariate effects on amplitude and the derived amplitude ratio. I shall treat the parameters representing the covariate effects on amplitude (hereafter called "amplitude parameters", for simplicity) as linear variables in the problem, and dipole location, orientation, and time-varying dipole magnitude function are treated as nonlinear variables (this "splitting" of the problem into linear and nonlinear parts was discussed in Sections 1.3.2 and 1.3.3). I will assume that some nonlinear optimization procedure has been used to estimate all variables except the amplitude parameters. The problem can then be expressed in matrix notation as an inconsistent set of linear equations and the amplitude parameters can be easily estimated. Using this method, I will show that although the amplitude parameters are estimated with error in the presence of model misspecification (i.e., the amplitude parameters are biased), derived amplitude ratios (i.e., the ratio of the estimated amplitude parameters) are unbiased under some

types of model misspecification (e.g., head model and time-varying magnitude function misspecification) for three special cases. These cases are the single dipole case, the case of multiple dipoles when all dipoles have the same magnitude, and the case of multiple dipoles when all dipoles are changing in the same way across replications (i.e., all amplitude ratios are equal). In addition, when all amplitudes are equal, misspecification of the number of dipoles will not affect amplitude ratio estimation.

Examples of evoked potentials generated by a single component include wave I of the auditory brainstem response and somatosensory N20. Physiologically, multiple dipoles with equal amplitude ratios could occur in response to auditory stimulation. The auditory system is bilateral rostral to the superior olive, and in the case of unilateral stimulation, the two hemispheres are probably not activated equally (i.e., the generators will not have the same amplitude). However, any adaptation (e.g., such as the "gating" of the testing auditory P50 response) would probably occur equally in both hemispheres. In the case of bilateral stimulation, equal amplitude and equal amplitude ratios are likely.

Notation: I use bold-faced letters to indicate vectors, bold-faced script letters to indicate matrices, and use normal-faced italic letters to indicate scalars. Unit vectors (vectors of length 1) are indicated by a $\hat{}$.

3.2 Proofs

3.2.1 Single time point, single dipole

Proposition 3.1 *For the case of fitting a single dipole to a single time point with head model misspecification, the amplitude parameter estimates are biased, and the ratio of amplitude parameter estimates is unbiased.*

Proof 3.1

Let

$\mathbf{V}_{gt}^{a}$ = $n \times 1$ vector of given surface potentials (generated by correct model, no noise) at a single time point

$\mathbf{V}_{ft}^a = n \times 1$ vector of fitted surface potentials at a single time point where n is the number of measurement locations. Then let

$$\begin{aligned} \mathbf{V}_{gt}^a &= c^a q_t \mathbf{g}(\boldsymbol{\theta}_g, \boldsymbol{\phi}_g) \\ \mathbf{V}_{ft}^a &= d^a p_t \mathbf{f}(\boldsymbol{\theta}_f, \boldsymbol{\phi}_f) \end{aligned}$$

where $\mathbf{g}(\boldsymbol{\theta}_g, \boldsymbol{\phi}_g)$ is an $n \times 1$ vector valued function which relates the given dipole location $\boldsymbol{\theta}_g$ and orientation $\boldsymbol{\phi}_g$ to the given noise-free potentials at the n measurement locations on the surface. If the surface is a sphere of homogeneous conductivity, then the function $\mathbf{g}(\boldsymbol{\theta}_g, \boldsymbol{\phi}_g)$ is the same as Equation 1.9, i.e. $\mathbf{g}(\boldsymbol{\theta}_g, \boldsymbol{\phi}_g) = (g_1(\boldsymbol{\theta}_g, \boldsymbol{\phi}_g), g_2(\boldsymbol{\theta}_g, \boldsymbol{\phi}_g), \ldots, g_n(\boldsymbol{\theta}_g, \boldsymbol{\phi}_g))^T$. The scalar c^a represents the true covariate effect on amplitude and q_t represents the common amplitude at time t of the dipole generator. The vector $\mathbf{f}(\boldsymbol{\theta}_f, \boldsymbol{\phi}_f)$ is an $n \times 1$ vector valued function which relates the fitted dipole location $\boldsymbol{\theta}_f$ and orientation $\boldsymbol{\phi}_f$ to the fitted potentials $\mathbf{V}_{ft}^a$. I assume that $\boldsymbol{\theta}_f$ and $\boldsymbol{\phi}_f$ have already been estimated by a nonlinear optimization procedure, and that $\mathbf{f}(\boldsymbol{\theta}_f, \boldsymbol{\phi}_f)$ has been computed. Furthermore, because of head model misspecification, $\mathbf{g}(\boldsymbol{\theta}_g, \boldsymbol{\phi}_g) \neq \mathbf{f}(\boldsymbol{\theta}_f, \boldsymbol{\phi}_f)$ in general. The estimated covariate effect on amplitude (i.e., the "amplitude parameter") is a scalar and is represented by d^a, and p_t represents the common amplitude time t of the fitted generator. I am considering the case of noise-free potentials.

For convenience, I can write:

$$\begin{aligned} \mathbf{g}(\boldsymbol{\theta}_g, \boldsymbol{\phi}_g) &= g_m \hat{\mathbf{g}} \\ \mathbf{f}(\boldsymbol{\theta}_f, \boldsymbol{\phi}_f) &= f_m \hat{\mathbf{f}} \end{aligned}$$

where $\hat{\mathbf{g}}$ is the unit vector and g_m is the length of $\mathbf{g}(\boldsymbol{\theta}_g, \boldsymbol{\phi}_g)$, and $\hat{\mathbf{f}}$ is the unit vector and f_m is the length of $\mathbf{f}(\boldsymbol{\theta}_f, \boldsymbol{\phi}_f)$. Therefore,

$$\begin{aligned} \mathbf{V}_{gt}^a &= c^a q_t g_m \hat{\mathbf{g}} \\ \mathbf{V}_{ft}^a &= d^a p_t f_m \hat{\mathbf{f}} \end{aligned}$$

Assuming I have measured $\mathbf{V}_{gt}^a$ and have some estimate of $p_t f_m \hat{\mathbf{f}}$, I am interested in finding d^a which minimizes the least squares error between $\mathbf{V}_{gt}^a$ and $\mathbf{V}_{ft}^a$.

I thus have a set of inconsistent equations of the form $\mathbf{a}x = \mathbf{b}$, where $\mathbf{a}$ is $p_t f_m \hat{\mathbf{f}}$, x is d^a, and $\mathbf{b}$ is $c^a q_t g_m \hat{\mathbf{g}}$. From Strang [104] I know that the least squares solution of $\mathbf{a}x = \mathbf{b}$ in one unknown is:

$$\bar{x} = \frac{\mathbf{a}^T\mathbf{b}}{\mathbf{a}^T\mathbf{a}} \tag{3.1}$$

Using this result to solve for d^a, and recalling that for vectors $\mathbf{a}^T\mathbf{b} = \mathbf{a} \cdot \mathbf{b}$ (dot product), that $\mathbf{a} \cdot \mathbf{b}$ is a scalar, and that $\hat{\mathbf{f}} \cdot \hat{\mathbf{f}} = 1$ (i.e., the dot product of a unit vector with itself is 1), I can show

$$d^a = \frac{(p_t f_m \hat{\mathbf{f}})^T c^a q_t g_m \hat{\mathbf{g}}}{(p_t f_m \hat{\mathbf{f}})^T p_t f_m \hat{\mathbf{f}}} = \frac{c^a p_t q_t f_m g_m \hat{\mathbf{f}} \cdot \hat{\mathbf{g}}}{p_t^2 f_m^2 \hat{\mathbf{f}} \cdot \hat{\mathbf{f}}} = \frac{c^a p_t q_t f_m g_m \hat{\mathbf{f}} \cdot \hat{\mathbf{g}}}{p_t^2 f_m^2} \tag{3.2}$$

and $d^a \neq c^a$ unless $g_m = f_m$, $q_t = p_t$, and $\hat{\mathbf{g}} = \hat{\mathbf{f}}$. Equation 3.2 shows that least squares fitting with an incorrect model ($\hat{\mathbf{g}} \neq \hat{\mathbf{f}}$ and/or $g_m \neq f_m$) will lead to errors in the estimated amplitude parameter d^a. In terms of dipole modeling of evoked potentials, $\hat{\mathbf{g}} \neq \hat{\mathbf{f}}$ when the shape of the volume conduction model used in fitting is not the same as for the given data (for example, if the given data were generated by a head and a sphere model was used for fitting). Even when the shape of the volume conduction model used in fitting is the same as for given data, if the conductivities of the volume conduction model used in fitting is not the same as for the true data, $g_m \neq f_m$. If the nonlinear optimization method did not solve the nonlinear least squares problem appropriately (i.e., converged to a local minimum), then even when no model misspecification is present, $\hat{\mathbf{g}} \neq \hat{\mathbf{f}}$ and $g_m \neq f_m$.

Now let us consider amplitude ratio estimates. Let $\mathbf{V}_{gt}^b$ be a second set of given potentials and $\mathbf{V}_{ft}^b$ be the fitted set of potentials at a single time point, described as follows:

$$\begin{aligned} \mathbf{V}_{gt}^b &= c^b q_t g_m \hat{\mathbf{g}} \\ \mathbf{V}_{ft}^b &= d^b p_t f_m \hat{\mathbf{f}} \end{aligned}$$

The length or amplitude of the data vectors are described by the norm, and the ratio of the norms of the vectors $\mathbf{V}_{gt}^a$ and $\mathbf{V}_{gt}^b$ can be computed as follows:

$$\frac{\| \mathbf{V}_{gt}^a \|_2}{\| \mathbf{V}_{gt}^b \|_2} = \frac{\sqrt{\mathbf{V}_{gt}^a \cdot \mathbf{V}_{gt}^a}}{\sqrt{\mathbf{V}_{gt}^b \cdot \mathbf{V}_{gt}^b}} = \frac{\sqrt{c^a c^a q_t^2 g_m^2 \hat{\mathbf{g}} \cdot \hat{\mathbf{g}}}}{\sqrt{c^b c^b q_t^2 g_m^2 \hat{\mathbf{g}} \cdot \hat{\mathbf{g}}}} = \frac{\sqrt{c^a c^a q_t^2 g_m^2}}{\sqrt{c^b c^b q_t^2 g_m^2}} = \frac{c^a}{c^b} \tag{3.3}$$

and the ratio of the norms of the vectors $\mathbf{V}^a_{ft}$ and $\mathbf{V}^b_{ft}$ can also be computed:

$$\frac{\| \mathbf{V}^a_{ft} \|_2}{\| \mathbf{V}^b_{ft} \|_2} = \frac{\sqrt{\mathbf{V}^a_{ft} \cdot \mathbf{V}^a_{ft}}}{\sqrt{\mathbf{V}^b_{ft} \cdot \mathbf{V}^b_{ft}}} = \frac{\sqrt{d^a d^a p_t^2 f_m^2 \hat{\mathbf{f}} \cdot \hat{\mathbf{f}}}}{\sqrt{d^b d^b p_t^2 f_m^2 \hat{\mathbf{f}} \cdot \hat{\mathbf{f}}}} = \frac{\sqrt{d^a d^a p_t^2 f_m^2}}{\sqrt{d^b d^b p_t^2 f_m^2}} = \frac{d^a}{d^b} \tag{3.4}$$

I can also show that d^b, the least squares solution to $\mathbf{a}x = \mathbf{b}$ where $\mathbf{a}$ is $p_t f_m \hat{\mathbf{f}}$, x is d^b, and $\mathbf{b}$ is $c^b q_t g_m \hat{\mathbf{g}}$, is

$$d^b = \frac{(p_t f_m \hat{\mathbf{f}})^T c^b q_t g_m \hat{\mathbf{g}}}{(p_t f_m \hat{\mathbf{f}})^T p_t f_m \hat{\mathbf{f}}} = \frac{c^b p_t q_t f_m g_m \hat{\mathbf{f}} \cdot \hat{\mathbf{g}}}{p_t^2 f_m^2 \hat{\mathbf{f}} \cdot \hat{\mathbf{f}}} = \frac{c^b p_t q_t f_m g_m \hat{\mathbf{f}} \cdot \hat{\mathbf{g}}}{p_t^2 f_m^2} \tag{3.5}$$

and then,

$$\frac{d^a}{d^b} = \frac{\frac{c^a p_t q_t f_m g_m \hat{\mathbf{f}} \cdot \hat{\mathbf{g}}}{p_t^2 f_m^2}}{\frac{c^b p_t q_t f_m g_m \hat{\mathbf{f}} \cdot \hat{\mathbf{g}}}{p_t^2 f_m^2}} = \frac{c^a}{c^b} \tag{3.6}$$

Equation 3.6 shows that ratios derived from the amplitude parameter estimates are preserved, even when fitting with an incorrect model, as long as the same model (f_m, p_t, and $\hat{\mathbf{f}}$) is used to fit both data sets, and both data sets are generated by the same g_m and $\hat{\mathbf{g}}$.

It is worthwhile to note that amplitude ratios are preserved no matter what f_m and $\hat{\mathbf{f}}$ are, as long as the same f_m and $\hat{\mathbf{f}}$ are used to fit both data sets. This means that the difference between the physical head model used for fitting and the true head does not affect the amplitude ratios. Inspection of equations 3.2 and 3.5 clearly shows that the difference between d^a and c^a or d^b and c^b becomes larger as the difference between g_m and f_m or $\hat{\mathbf{g}}$ and $\hat{\mathbf{f}}$ becomes larger. But the amplitude ratio is preserved regardless of the differences between g_m and f_m or $\hat{\mathbf{g}}$ and $\hat{\mathbf{f}}$. This also shows that when fitting the amplitude parameters linearly, failure of the nonlinear optimization method to converge to the global minimum (the global minimum is the best estimate of $\boldsymbol{\theta}_f$ and $\boldsymbol{\phi}_f$, which are subsequently used to compute f_m and $\hat{\mathbf{f}}$) will not affect the amplitude ratios, since the values of f_m and $\hat{\mathbf{f}}$ are not important and cancel in the computation of d^a/d^b.

When the amplitude parameters are not estimated linearly, f_m and $\hat{\mathbf{f}}$ are not guaranteed to cancel *unless* the global minimum is reached by the nonlinear optimization routine (i.e., the least squares fit is *truly* the *best* least squares fit). In

other words, when a nonlinear optimization routine is used to estimate the amplitude parameters, d^a will not equal the right side of Equation 3.2 (the solution found using linear estimation), and d^b will not equal the right side of Equation 3.5 (the solution found using linear estimation) *unless* the global minimum is reached. The effects of head model misspecification only cancel when d^a and d^b are the same as in Equations 3.2 and 3.5.

Although the previous work assumed fitting at a single time point, I can extend it to multiple time points, as follows.

3.2.2 Multiple time points, single dipole

Proposition 3.2 *For the case of fitting a single dipole to multiple time points with head model misspecification and time-varying dipole magnitude function misspecification, the amplitude parameter estimates are biased, but the derived ratio of the amplitude parameter estimates is unbiased.*

Proof 3.2

Let

$\mathcal{V}_g^a = n \times u$ matrix of "true" potentials

$\mathcal{V}_f^a = n \times u$ matrix of fitted potentials

$\mathcal{V}_o^a = n \times u$ matrix of unscaled fitted potentials

where n is number of measurement locations and u is number of time points, and let $t = 0, \ldots, u$. I denote the following:

$$\begin{aligned} \mathbf{V}_{gt}^a &= \text{column } t \text{ of matrix } \mathcal{V}_g^a \\ \mathbf{V}_{ft}^a &= \text{column } t \text{ of matrix } \mathcal{V}_f^a \\ \mathbf{V}_{ot}^a &= \text{column } t \text{ of matrix } \mathcal{V}_o^a \end{aligned}$$

where

$$\begin{aligned} \mathbf{V}_{gt}^a &= c^a q_t(\boldsymbol{\chi}) \hat{\mathbf{g}}(\boldsymbol{\theta}_g, \boldsymbol{\phi}_g) \\ \mathbf{V}_{ot}^a &= p_t(\boldsymbol{\psi}) \hat{\mathbf{f}}(\boldsymbol{\theta}_f, \boldsymbol{\phi}_f) \\ \mathbf{V}_{ft}^a &= d^a \mathbf{V}_{ot}^a \end{aligned}$$

and where $q_t(\boldsymbol{\chi})$ is the true time-varying dipole magnitude, which describes the shape of the dipole activity over time t as a function of the parameter vector $\boldsymbol{\chi}$. The fitted time-varying dipole magnitude is $p_t(\boldsymbol{\psi})$ is a function of the fitted parameter vector $\boldsymbol{\psi}$, and in general, $q_t(\boldsymbol{\chi}) \neq p_t(\boldsymbol{\psi})$ because of model misspecification (both misspecification of the head model and time-varying dipole magnitude function). For example, the dipole components model [10] used in Chapter 2 used a decaying sinusoid for $p_t(\boldsymbol{\psi})$, such that $\psi_1 = \alpha$, $\psi_2 = \lambda$, $\psi_3 = \tau$, and $\psi_4 = \beta$. It is unlikely that the true dipole magnitude function $q_t(\boldsymbol{\chi})$ is a decaying sinusoid .

For simplicity, let

$$\begin{aligned} q_t(\boldsymbol{\chi}) &= q_t \\ p_t(\boldsymbol{\psi}) &= p_t \end{aligned} \tag{3.7}$$

I can then write:

$$\begin{aligned} \mathbf{V}_{gt}^a &= c^a q_t g_m \hat{\mathbf{g}} \\ \mathbf{V}_{ot}^a &= p_t f_m \hat{\mathbf{f}} \\ \mathbf{V}_{ft}^a &= d^a \mathbf{V}_{ot} \end{aligned}$$

Let $\mathbf{V}_g^a$, $\mathbf{V}_o^a$, and $\mathbf{V}_f^a$ be $nu \times 1$ vectors, where

$$\mathbf{V}_g^a = \begin{bmatrix} \mathbf{V}_{g0}^a \\ \mathbf{V}_{g1}^a \\ \vdots \\ \mathbf{V}_{gu}^a \end{bmatrix} \quad \mathbf{V}_o^a = \begin{bmatrix} \mathbf{V}_{o0}^a \\ \mathbf{V}_{o1}^a \\ \vdots \\ \mathbf{V}_{ou}^a \end{bmatrix} \quad \mathbf{V}_f^a = d^a \begin{bmatrix} \mathbf{V}_{o0}^a \\ \mathbf{V}_{o1}^a \\ \vdots \\ \mathbf{V}_{ou}^a \end{bmatrix}$$

As before, assuming I have been given $\mathbf{V}_g^a$ and have some estimate of $\mathbf{V}_o^a$, I am interested in finding d^a which minimizes the least squares error between $\mathbf{V}_g^a$ and $\mathbf{V}_f^a$. I again have a set of inconsistent equations of the form $\mathbf{a}x = \mathbf{b}$, where $\mathbf{a}$ is $\mathbf{V}_o^a$, x is d^a, and b is $\mathbf{V}_g^a$. Using equation 3.1, I find:

$$\mathbf{a}^T\mathbf{b} = c^a p_0 q_0 f_m g_m \hat{\mathbf{f}} \cdot \hat{\mathbf{g}} + c^a p_1 q_1 f_m g_m \hat{\mathbf{f}} \cdot \hat{\mathbf{g}} + \cdots + c^a p_u q_u f_m g_m \hat{\mathbf{f}} \cdot \hat{\mathbf{g}}$$

$$
\begin{aligned}
&= c^a f_m g_m \hat{\mathbf{f}} \cdot \hat{\mathbf{g}} \left(\sum_{t=0}^{u} p_t q_t \right) \\
\mathbf{a}^T\mathbf{a} &= p_0^2 f_m^2 + p_1^2 f_m^2 + \cdots + p_u^2 f_m^2 \\
&= f_m^2 \left(\sum_{t=0}^{u} p_t^2 \right) \\
d^a &= \frac{\mathbf{a}^T\mathbf{b}}{\mathbf{a}^T\mathbf{a}} = \frac{c^a f_m g_m \hat{\mathbf{f}} \cdot \hat{\mathbf{g}} \left(\sum_{t=0}^{u} p_t q_t \right)}{f_m^2 \left(\sum_{t=0}^{u} p_t^2 \right)}
\end{aligned} \tag{3.8}
$$

and therefore $d^a \neq c^a$ unless $p_t = q_t \; \forall t$, $\hat{\mathbf{f}} \cdot \hat{\mathbf{g}} = 1$ (implying that $\hat{\mathbf{f}} = \hat{\mathbf{g}}$), and $g_m = f_m$. Equation 3.8 shows that least squares fitting with an incorrect time-varying amplitude function (i.e., when $p_t \neq q_t$), even if the correct head model is used, leads to an error in the amplitude parameter estimate d^a.

Now I will consider the derived amplitude ratio estimate. Let $\mathbf{V}_g^b$ be a second set of given potentials measured over time and $\mathbf{V}_o^b$ and $\mathbf{V}_f^b$ be the unscaled fitted and fitted potentials to $\mathbf{V}_g^b$, described as follows:

$$
\mathbf{V}_g^b = \begin{bmatrix} \mathbf{V}_{g0}^b \\ \mathbf{V}_{g1}^b \\ \vdots \\ \mathbf{V}_{gu}^b \end{bmatrix} \quad \mathbf{V}_o^b = \begin{bmatrix} \mathbf{V}_{o0}^b \\ \mathbf{V}_{o1}^b \\ \vdots \\ \mathbf{V}_{ou}^b \end{bmatrix} \quad \mathbf{V}_f^b = d^b \begin{bmatrix} \mathbf{V}_{o0}^b \\ \mathbf{V}_{o1}^b \\ \vdots \\ \mathbf{V}_{ou}^b \end{bmatrix}
$$

where

$$
\begin{aligned}
\mathbf{V}_{gt}^b &= c^b q_t g_m \hat{\mathbf{g}} \\
\mathbf{V}_{ot}^b &= p_t f_m \hat{\mathbf{f}}
\end{aligned}
$$

The ratio of the norms of the vectors $\mathbf{V}_g^a$ to $\mathbf{V}_g^b$ and $\mathbf{V}_f^a$ to $\mathbf{V}_f^b$ can be computed as follows:

$$
\begin{aligned}
\frac{\| \mathbf{V}_g^a \|_2}{\| \mathbf{V}_g^b \|_2} &= \frac{\sqrt{\mathbf{V}_g^a \cdot \mathbf{V}_g^a}}{\sqrt{\mathbf{V}_g^b \cdot \mathbf{V}_g^b}} \\
&= \frac{\sqrt{c^a c^a q_0^2 g_m^2 + c^a c^a q_1^2 g_m^2 + \cdots + c^a c^a q_u^2 g_m^2}}{\sqrt{c^b c^b q_0^2 g_m^2 + c^b c^b q_1^2 g_m^2 + \cdots + c^b c^b q_u^2 g_m^2}} \\
&= \frac{\sqrt{c^a c^a g_m^2 \sum_{t=0}^{u} q_t^2}}{\sqrt{c^b c^b g_m^2 \sum_{t=0}^{u} q_t^2}}
\end{aligned}
$$

$$= \frac{c^a g_m \sqrt{\sum_{t=0}^{u} q_t^2}}{c^b g_m \sqrt{\sum_{t=0}^{u} q_t^2}}$$
$$= \frac{c^a}{c^b}$$

$$\frac{\| \mathbf{V}_f^a \|_2}{\| \mathbf{V}_f^b \|_2} = \frac{\sqrt{\mathbf{V}_f^a \cdot \mathbf{V}_f^a}}{\sqrt{\mathbf{V}_f^b \cdot \mathbf{V}_f^b}}$$
$$= \frac{\sqrt{d^a d^a p_0^2 f_m^2 + d^a d^a p_1^2 f_m^2 + \cdots + d^a d^a p_u^2 f_m^2}}{\sqrt{d^b d^b p_0^2 f_m^2 + d^b d^b p_1^2 f_m^2 + \cdots + d^b d^b p_u^2 f_m^2}}$$
$$= \frac{\sqrt{d^a d^a f_m^2 \sum_{t=0}^{u} p_t^2}}{\sqrt{d^b d^b f_m^2 \sum_{t=0}^{u} p_t^2}}$$
$$= \frac{d^a f_m \sqrt{\sum_{t=0}^{u} p_t^2}}{d^b f_m \sqrt{\sum_{t=0}^{u} p_t^2}}$$
$$= \frac{d^a}{d^b}$$

I can also show that d^b, the least squares solution to $\mathbf{a}x = \mathbf{b}$ where $\mathbf{a}$ is $\mathbf{V}_o^b$, x is d^b, and $\mathbf{b}$ is $\mathbf{V}_g^b$ is

$$d^b = \frac{c^b f_m g_m \hat{\mathbf{f}} \cdot \hat{\mathbf{g}} \left(\sum_{t=0}^{u} p_t q_t\right)}{f_m^2 \left(\sum_{t=0}^{u} p_t^2\right)}$$

Then,

$$\frac{d^a}{d^b} = \frac{\frac{c^a f_m g_m \hat{\mathbf{f}} \cdot \hat{\mathbf{g}} \left(\sum_{t=0}^{u} p_t q_t\right)}{f_m^2 \left(\sum_{t=0}^{u} p_t^2\right)}}{\frac{c^b f_m g_m \hat{\mathbf{f}} \cdot \hat{\mathbf{g}} \left(\sum_{t=0}^{u} p_t q_t\right)}{f_m^2 \left(\sum_{t=0}^{u} p_t^2\right)}} = \frac{c^a}{c^b} \tag{3.9}$$

Equation 3.9 shows that the amplitude ratio is correctly estimated, even when fitting with an incorrect head model and/or an incorrect time-varying dipole magnitude function, as long as the same model (f_m and $\hat{\mathbf{f}}$) and same amplitude waveshape (p_t) is used to fit both data sets, and both data sets are generated by the same g_m, $\hat{\mathbf{g}}$, and q_t. The assumption that both data sets are generated by the same g_m, $\hat{\mathbf{g}}$ and q_t is reasonable for subcortical and short-latency cortical EPs, because they are "hard-wired" responses, as discussed in Chapter 1.

I have shown so far that amplitude ratios are estimated without bias in the face of head model misspecification and misspecification of the time-varying dipole magnitude function. I am also interested in the effect of misspecification of the number of dipoles used in fitting, particularly the case when two generators are mistakenly fit by a single dipole.

3.2.3 Misspecification of number of dipoles

I will assume that the two generators have the same amplitude, but I will not assume that the two generators are synchronous (i.e., the generators can have different "waveshapes"). This is a reasonable assumption when looking at early generators (subcortical and short latency cortical) of potentials evoked by bilateral stimulation, such as the auditory P50 evoked response. The bilateral generators should then have similar amplitudes (but perhaps different waveshapes), that should change similarly in response to different stimulation intensities or rates.

Proposition 3.3 *For the case of fitting a misspecified number of dipoles to multiple time points with head model and time-varying dipole magnitude function misspecification, the amplitude parameter estimates are biased, but the ratio of amplitude parameter estimates is unbiased, assuming that all true generators have the same amplitude (within a data set) and amplitude ratio (computed across data sets).*

Proof 3.3

Let

$\mathcal{V}_g^a = n \times u$ matrix of given potentials

$\mathcal{V}_f^a = n \times u$ matrix of fitted potentials

$\mathcal{V}_o^a = n \times u$ matrix of unscaled fitted potentials

where n is number of measurement locations and u is number of time points. Then let

$$\begin{aligned} \mathbf{V}_{gt}^a &= c^a[q_{1t}(\boldsymbol{\chi}_1)\mathbf{g}_1(\boldsymbol{\theta}_{g1}, \boldsymbol{\phi}_{g1}) + q_{2t}(\boldsymbol{\chi}_2)\mathbf{g}_2(\boldsymbol{\theta}_{g2}, \boldsymbol{\phi}_{g2})] \\ \mathbf{V}_{ft}^a &= d^a p_t(\boldsymbol{\psi})\mathbf{f}(\boldsymbol{\theta}_f, \boldsymbol{\phi}_f) \end{aligned}$$

where c^a, d^a, p_t, and $\mathbf{f}(\boldsymbol{\theta}_f, \boldsymbol{\phi}_f)$ are defined as previously. The time-varying magnitude of "true" generator 1 at time t is q_{1t} and is a function of $\boldsymbol{\chi}_1$, and q_{2t} is the time-varying magnitude of "true" generator 2 as a function of $\boldsymbol{\chi}_2$ at time t. Note that for synchronous generators, $q_{1t} = q_{2t}$. I do not not require equality of q_{1t} and q_{2t}, however, and the two generators can have different waveforms. Let $\mathbf{g}_1(\boldsymbol{\theta}_{g1}, \boldsymbol{\phi}_{g1})$ be an $n \times 1$ vector valued function that relates the true dipole location and orientation ($\boldsymbol{\theta}_{g1}$ and $\boldsymbol{\phi}_{g1}$) of the first generator to the given noise-free potentials, and $\mathbf{g}_2(\boldsymbol{\theta}_{g2}, \boldsymbol{\phi}_{g2})$ is an $n \times 1$ vector valued function that relates the true dipole location and orientation ($\boldsymbol{\theta}_{g2}$ and $\boldsymbol{\phi}_{g2}$) of the second generator to the given noise-free potentials.

Using notation similar to that in the previous proofs, let

$$\begin{aligned} \mathbf{V}^a_{gt} &= c^a(q_{1t} g_{m1} \hat{\mathbf{g}}_1 + q_{2t} g_{m2} \hat{\mathbf{g}}_2) \\ \mathbf{V}^a_{ot} &= p_t f_m \hat{\mathbf{f}} \\ \mathbf{V}^a_{ft} &= d^a \mathbf{V}_{ot} \end{aligned}$$

I can also then define the $nu \times 1$ vectors $\mathbf{V}^a_g$, $\mathbf{V}^a_o$, and $\mathbf{V}^a_f$ as before:

$$\mathbf{V}^a_g = \begin{bmatrix} \mathbf{V}^a_{g0} \\ \mathbf{V}^a_{g1} \\ \vdots \\ \mathbf{V}^a_{gu} \end{bmatrix} \quad \mathbf{V}^a_o = \begin{bmatrix} \mathbf{V}^a_{o0} \\ \mathbf{V}^a_{o1} \\ \vdots \\ \mathbf{V}^a_{ou} \end{bmatrix} \quad \mathbf{V}^a_f = d^a \begin{bmatrix} \mathbf{V}^a_{o0} \\ \mathbf{V}^a_{o1} \\ \vdots \\ \mathbf{V}^a_{ou} \end{bmatrix}$$

I use equation 3.1 to solve for d^a, and find

$$\begin{aligned} \mathbf{a}^T\mathbf{b} &= c^a(p_0 q_{10} f_m g_{m1} \hat{\mathbf{g}}_1 \cdot \hat{\mathbf{f}} + p_0 q_{20} f_m g_{m2} \hat{\mathbf{g}}_2 \cdot \hat{\mathbf{f}}) + \cdots + \\ &\quad c^a(p_u q_{1u} f_m g_{m1} \hat{\mathbf{g}}_1 \cdot \hat{\mathbf{f}} + p_u q_{2u} f_m g_{m2} \hat{\mathbf{g}}_2 \cdot \hat{\mathbf{f}}) \\ &= c^a f_m \left[\left(g_{m1} \hat{\mathbf{g}}_1 \cdot \hat{\mathbf{f}} \sum_{t=0}^{u} p_t q_{1t} \right) + \left(g_{m2} \hat{\mathbf{g}}_2 \cdot \hat{\mathbf{f}} \sum_{t=0}^{u} p_t q_{2t} \right) \right] \\ \mathbf{a}^T\mathbf{a} &= f_m^2 \sum_{t=0}^{u} p_t^2 \\ d^a &= \frac{\mathbf{a}^T\mathbf{b}}{\mathbf{a}^T\mathbf{a}} = \frac{c^a f_m \left[\left(g_{m1} \hat{\mathbf{g}}_1 \cdot \hat{\mathbf{f}} \sum_{t=0}^{u} p_t q_{1t} \right) + \left(g_{m2} \hat{\mathbf{g}}_2 \cdot \hat{\mathbf{f}} \sum_{t=0}^{u} p_t q_{2t} \right) \right]}{f_m^2 \sum_{t=0}^{u} p_t^2} \end{aligned} \tag{3.10}$$

Equation 3.10 shows that $d^a \neq c^a$ and that least squares fitting will lead to errors in amplitude parameter estimates.

Now I will consider amplitude ratio estimates. Let $\mathbf{V}_g^b$ be a second set of given potentials and $\mathbf{V}_o^b$ and $\mathbf{V}_f^b$ be the unscaled fitted and fitted potentials to $\mathbf{V}_g^b$. Let

$$\mathbf{V}_g^b = \begin{bmatrix} \mathbf{V}_{g0}^b \\ \mathbf{V}_{g1}^b \\ \vdots \\ \mathbf{V}_{gu}^b \end{bmatrix} \quad \mathbf{V}_o^b = \begin{bmatrix} \mathbf{V}_{o0}^b \\ \mathbf{V}_{o1}^b \\ \vdots \\ \mathbf{V}_{ou}^b \end{bmatrix} \quad \mathbf{V}_f^b = d^b \begin{bmatrix} \mathbf{V}_{o0}^b \\ \mathbf{V}_{o1}^b \\ \vdots \\ \mathbf{V}_{ou}^b \end{bmatrix}$$

where

$$\begin{aligned} \mathbf{V}_{gt}^b &= c^b(q_{1t}g_{m1}\hat{\mathbf{g}}_1 + q_{2t}g_{m2}\hat{\mathbf{g}}_2) \\ \mathbf{V}_{ot}^b &= p_t f_m \hat{\mathbf{f}} \\ \mathbf{V}_{ft}^b &= d^b \mathbf{V}_{ot} \end{aligned}$$

The ratio of the norms of the vectors $\mathbf{V}_g^a$ to $\mathbf{V}_g^b$ and $\mathbf{V}_f^a$ and $\mathbf{V}_f^b$ can be easily computed:

$$\begin{aligned} \frac{\| \mathbf{V}_g^a \|_2}{\| \mathbf{V}_g^b \|_2} &= \frac{\sqrt{\mathbf{V}_g^b \cdot \mathbf{V}_g^b}}{\sqrt{\mathbf{V}_g^b \cdot \mathbf{V}_g^b}} \\ &= \frac{\sqrt{c^a c^a (g_{m1}^2 \sum_{t=0}^u q_{1t}^2 + 2g_{m1}g_{m2}\hat{\mathbf{g}}_1\hat{\mathbf{g}}_2 \sum_{t=0}^u q_{1t}q_{2t} + g_{m2}^2 \sum_{t=0}^u q_{2t}^2)}}{\sqrt{c^b c^b (g_{m1}^2 \sum_{t=0}^u q_{1t}^2 + 2g_{m1}g_{m2}\hat{\mathbf{g}}_1\hat{\mathbf{g}}_2 \sum_{t=0}^u q_{1t}q_{2t} + g_{m2}^2 \sum_{t=0}^u q_{2t}^2)}} \\ &= \frac{c^a \sqrt{g_{m1}^2 \sum_{t=0}^u q_{1t}^2 + 2g_{m1}g_{m2}\hat{\mathbf{g}}_1\hat{\mathbf{g}}_2 \sum_{t=0}^u q_{1t}q_{2t} + g_{m2}^2 \sum_{t=0}^u q_{2t}^2}}{c^b \sqrt{g_{m1}^2 \sum_{t=0}^u q_{1t}^2 + 2g_{m1}g_{m2}\hat{\mathbf{g}}_1\hat{\mathbf{g}}_2 \sum_{t=0}^u q_{1t}q_{2t} + g_{m2}^2 \sum_{t=0}^u q_{2t}^2}} \\ &= \frac{c^a}{c^b} \\ \frac{\| \mathbf{V}_f^a \|_2}{\| \mathbf{V}_f^b \|_2} &= \frac{\sqrt{\mathbf{V}_f^a \cdot \mathbf{V}_f^a}}{\sqrt{\mathbf{V}_f^b \cdot \mathbf{V}^{\mathbf{b}}{}_f}} \\ &= \frac{\sqrt{d^a d^a p_0^2 f_m^2 + d^a d^a p_1^2 f_m^2 + \cdots + d^a d^a p_u^2 f_m^2}}{\sqrt{d^b d^b p_0^2 f_m^2 + d^b d^b p_1^2 f_m^2 + \cdots + d^b d^b p_u^2 f_m^2}} \\ &= \frac{\sqrt{d^a d^a f_m^2 \sum_{t=0}^u p_t^2}}{\sqrt{d^b d^b f_m^2 \sum_{t=0}^u p_t^2}} \\ &= \frac{d^a f_m \sqrt{\sum_{t=0}^u p_t^2}}{d^b f_m \sqrt{\sum_{t=0}^u p_t^2}} \end{aligned}$$

$$= \frac{d^a}{d^b}$$

I can also show that d^b is

$$d^b = \frac{\mathbf{a}^T\mathbf{b}}{\mathbf{a}^T\mathbf{a}} = \frac{c^b f_m \left[\left(g_{m1}\hat{\mathbf{g}}_1 \cdot \hat{\mathbf{f}} \sum_{t=0}^{u} p_t q_{1t}\right) + \left(g_{m2}\hat{\mathbf{g}}_2 \cdot \hat{\mathbf{f}} \sum_{t=0}^{u} p_t q_{2t}\right)\right]}{f_m^2 \sum_{t=0}^{u} p_t^2} \tag{3.11}$$

Then I compute d^a/d^b as

$$\frac{d^a}{d^b} = \frac{\frac{c^a f_m\left[\left(g_{m1}\hat{\mathbf{g}}_1 \cdot \hat{\mathbf{f}} \sum_{t=0}^{u} p_t q_{1t}\right)+\left(g_{m2}\hat{\mathbf{g}}_2 \cdot \hat{\mathbf{f}} \sum_{t=0}^{u} p_t q_{2t}\right)\right]}{f_m^2 \sum_{t=0}^{u} p_t^2}}{\frac{c^b f_m\left[\left(g_{m1}\hat{\mathbf{g}}_1 \cdot \hat{\mathbf{f}} \sum_{t=0}^{u} p_t q_{1t}\right)+\left(g_{m2}\hat{\mathbf{g}}_2 \cdot \hat{\mathbf{f}} \sum_{t=0}^{u} p_t q_{2t}\right)\right]}{f_m^2 \sum_{t=0}^{u} p_t^2}}$$

$$= \frac{c^a}{c^b} \tag{3.12}$$

Equation 3.12 shows that amplitude ratios are estimated without bias when the number of dipoles is misspecified and the same $\hat{\mathbf{f}}$, f_m, and p_t are used to fit both sets of given potentials. It is important to note that the two given dipole generators do not need to be bilaterally symmetric, and the two dipoles do not need to have the same time-varying dipole magnitude (i.e., q_{1t} does not have to equal q_{2t}), although they must be scaled the same way (i.e., both dipoles must be scaled by c^a and c^b). When all true generators have the same amplitude, it is only important to use the same model ($\hat{\mathbf{f}}$, f_m, and p_t) when fitting the two sets of data for unbiased ratio estimation.

The preceding work seems to suggest that amplitude ratios are always preserved during dipole modeling, and may cause one to conclude that dipole modeling can correctly estimate amplitude ratios for multiple dipole problems despite model misspecification. Unfortunately, amplitude ratios are preserved only in the special cases such as in Sections 3.2.1-3.2.3 (i.e., single dipole active, or two dipoles with the same scaling). Dipole modeling is not a "magic" method for accurately estimating generator amplitude ratios. In the next section I will show that, in general, neither amplitude parameter estimates nor amplitude ratio estimates will be unbiased in the face of model misspecification, and will also show another special case in which amplitude ratios are unbiased.

3.2.4 Multiple dipoles

Proposition 3.4 *For the case of fitting multiple dipoles to multiple time points with head model and time-varying dipole magnitude function misspecification, both amplitude parameter and amplitude ratio estimates are biased, unless all dipoles have the same amplitude ratio (computed across data sets).*

Proof 3.4

For an inconsistent set of equations of the form $\mathcal{A}\mathbf{x} = \mathbf{b}$, the least squares solution is [104]:

$$\mathbf{x} = (\mathcal{A}^T\mathcal{A})^{-1}\mathcal{A}^T\mathbf{b} \tag{3.13}$$

and for the case of dipole modeling

$$\begin{aligned}
\mathbf{x} &= \text{vector of dipole amplitudes} \\
\mathbf{b} &= \text{vector of given potentials} \\
\mathcal{A} &= \text{map from dipole amplitude to potentials at the measurement locations} \\
(\mathcal{A}^T\mathcal{A})^{-1}\mathcal{A}^T &= \text{map from potentials to dipoles amplitudes}
\end{aligned}$$

where $\mathcal{A} \in \Re^{nu \times l}$, $\mathbf{x} \in \Re^{l}$, and $\mathbf{b} \in \Re^{nu}$. As previously defined, n is the number of measurement locations, u is the number of time points, and I now define l to be the number of dipoles.

Using the notation developed in previous proofs, I can define $\mathcal{A}$, $\mathbf{x}$, and $\mathbf{b}$. Let

$$\begin{aligned}
\mathcal{V}_g^a &= \mathcal{V}_{g_1}^a + \mathcal{V}_{g_2}^a + \cdots + \mathcal{V}_{g_l}^a \\
\mathcal{V}_f^a &= \mathcal{V}_{f_1}^a + \mathcal{V}_{f_2}^a + \cdots + \mathcal{V}_{f_l}^a
\end{aligned}$$

where $\mathcal{V}_g^a$ and $\mathcal{V}_f^a$ are $n \times u$ matrices of given and fitted potentials. Letting j index dipoles and t index time points, I can write ($\forall\, j$ and t),

$$\begin{aligned}
\mathbf{V}_{g,t}^a &= c_j^a q_{jt}(\boldsymbol{\chi}_j)\mathbf{g}_j(\boldsymbol{\theta}_{g,t}, \boldsymbol{\phi}_{g_j}) \\
\mathbf{V}_{f,t}^a &= d_j^a p_{jt}(\boldsymbol{\psi}_j)\mathbf{f}_j(\boldsymbol{\theta}_{f,t}, \boldsymbol{\phi}_{f_j})
\end{aligned}$$

or, in the shorthand notation used previously,

$$\begin{aligned}
\mathbf{V}^a_{g_j t} &= c^a_j q_{jt} g_{mj} \hat{\mathbf{g}}_j \\
\mathbf{V}^a_{o_j t} &= p_{jt} f_{mj} \hat{\mathbf{f}}_j \\
\mathbf{V}^a_{f_j t} &= d^a_j \mathbf{V}_{o_j t}
\end{aligned}$$

And now

$$\mathcal{A} = \begin{bmatrix} \mathbf{V}^a_{o_1 0} & \mathbf{V}^a_{o_2 0} & \cdots & \mathbf{V}^a_{o_l 0} \\ \mathbf{V}^a_{o_1 1} & \ddots & & \vdots \\ \vdots & & \ddots & \vdots \\ \mathbf{V}^a_{o_1 u} & \cdots & \cdots & \mathbf{V}^a_{o_l u} \end{bmatrix}$$

$$\mathbf{x} = \begin{bmatrix} d^a_1 \\ d^a_2 \\ \vdots \\ d^a_l \end{bmatrix} \quad \mathbf{b} = \begin{bmatrix} \mathbf{V}^a_{g_1 0} + \mathbf{V}^a_{g_2 0} + \cdots + \mathbf{V}^a_{g_l 0} \\ \mathbf{V}^a_{g_1 1} + \mathbf{V}^a_{g_2 1} + \cdots + \mathbf{V}^a_{g_l 1} \\ \vdots \\ \mathbf{V}^a_{g_1 u} + \mathbf{V}^a_{g_2 u} + \cdots + \mathbf{V}^a_{g_l u} \end{bmatrix}$$

The map from potentials to dipole amplitudes, $(\mathcal{A}^T\mathcal{A})^{-1}\mathcal{A}^T$ is an $l \times nu$ matrix, and I will denote the rows of this matrix by $\mathbf{y}^T_j$, where $\mathbf{y}_j$ are $nu \times 1$ vectors, as shown:

$$(\mathcal{A}^T\mathcal{A})^{-1}\mathcal{A}^T = \begin{bmatrix} \mathbf{y}^T_1 \\ \mathbf{y}^T_2 \\ \vdots \\ \mathbf{y}^T_l \end{bmatrix}$$

Using Equation 3.13, I can find that d^a_1 is just $\mathbf{y}^T_1\mathbf{b}$, d^a_2 is $\mathbf{y}^T_2\mathbf{b}$, and so on for all d^a_j, as shown:

$$d^a_j = g_{m1} c^a_1 \hat{\mathbf{g}}_1 \cdot \mathbf{y}_j \sum_{t=0}^{u} q_{1t} + g_{m2} c^a_2 \hat{\mathbf{g}}_2 \cdot \mathbf{y}_j \sum_{t=0}^{u} q_{2t} + \ldots + g_{ml} c^a_l \hat{\mathbf{g}}_l \cdot \mathbf{y}_j \sum_{t=0}^{u} q_{lt} \qquad (3.14)$$

It can be easily shown that for a second set of data, that differs from the first data set by only the dipole amplitudes of each generator, that

$$d^b_j = g_{m1} c^b_1 \hat{\mathbf{g}}_1 \cdot \mathbf{y}_j \sum_{t=0}^{u} q_{1t} + g_{m2} c^b_2 \hat{\mathbf{g}}_2 \cdot \mathbf{y}_j \sum_{t=0}^{u} q_{2t} + \ldots + g_{ml} c^b_l \hat{\mathbf{g}}_l \cdot \mathbf{y}_j \sum_{t=0}^{u} q_{lt}$$

Equation 3.14 shows that in general the amplitude parameters are biased when estimated using dipole modeling via least squares fitting because $d_j^a \neq c_j^a$, and instead d_j^a is some combination of all the true dipole amplitudes. This is clear by simply rewriting Equation 3.14 as

$$d_j^a = c_1^a x_1 + c_2^a x_2 + \ldots + c_j^a x_j + \ldots + c_l^a x_l \tag{3.15}$$

where $x_i = g_{mi}\hat{\mathbf{g}}_i \cdot \mathbf{y}_j \sum_{t=0}^{u} q_{it}$. From Equation 3.15, it is obvious that $d_j^a \neq c_j^a$ in general.

The question that remains is whether or not the amplitude ratio for each individual dipole is preserved. The amplitude ratio of the individual "true" dipoles is simply the ratio of the norms of each dipole contribution to the potential map, the $\mathbf{V}_{g,t}^i$. The amplitude ratio of the individual fitted dipoles is the ratio of the norms of $\mathbf{V}_{f,t}^i$. These are easily shown to be:

$$\begin{aligned} \frac{\| \mathbf{V}_{g,t}^a \|_2}{\| \mathbf{V}_{t,t}^b \|_2} &= \frac{c_j^a}{c_j^b} \\ \frac{\| \mathbf{V}_{f,t}^a \|_2}{\| \mathbf{V}_{f,t}^b \|_2} &= \frac{d_j^a}{d_j^b} \end{aligned}$$

For simplicity, I will again assume that $x_i = g_{mi}\hat{\mathbf{g}}_i \cdot \mathbf{y}_j \sum_{t=0}^{u} q_{it}$. I can then show

$$\begin{aligned} \frac{d_j^a}{d_j^b} &= \frac{g_{m1}c_1^a\hat{\mathbf{g}}_1 \cdot \mathbf{y}_j \sum_{t=0}^{u} q_{1t} + g_{m2}c_2^a\hat{\mathbf{g}}_2 \cdot \mathbf{y}_j \sum_{t=0}^{u} q_{2t} + \ldots + g_{ml}c_l^a\hat{\mathbf{g}}_l \cdot \mathbf{y}_j \sum_{t=0}^{u} q_{lt}}{g_{m1}c_1^b\hat{\mathbf{g}}_1 \cdot \mathbf{y}_j \sum_{t=0}^{u} q_{1t} + g_{m2}c_2^b\hat{\mathbf{g}}_2 \cdot \mathbf{y}_j \sum_{t=0}^{u} q_{2t} + \ldots + g_{ml}c_l^b\hat{\mathbf{g}}_l \cdot \mathbf{y}_j \sum_{t=0}^{u} q_{lt}} \\ &= \frac{c_1^a x_1 + c_2^a x_2 + \ldots + c_l^a x_l}{c_1^b x_1 + c_2^b x_2 + \ldots + c_l^b x_l} \\ &= \frac{c_j^a}{c_j^b} + \frac{(c_1^a - \frac{c_j^a}{c_j^b}c_1^b)x_1 + (c_2^a - \frac{c_j^a}{c_j^b}c_2^b)x_2 + \ldots + (c_l^a - \frac{c_j^a}{c_j^b}c_l^b)x_l}{c_1^2 x_1 + c_2^2 x_2 + \ldots + c_l^2 x_l} \end{aligned} \tag{3.16}$$

Equation 3.16 shows that, in general, d_j^a/d_j^b equals c_j^a/c_j^b plus a remainder term. For simplicity, I can rewrite Equation 3.16 as

$$\frac{d_j^a}{d_j^b} = \frac{c_j^a}{c_j^b} + \frac{z_n}{z_d} \tag{3.17}$$

where z_n and z_d are defined as follows:

$$\begin{aligned} z_n &= (c_1^a - \frac{c_j^a}{c_j^b}c_1^b)x_1 + (c_2^a - \frac{c_j^a}{c_j^b}c_2^b)x_2 + \ldots + (c_l^a - \frac{c_j^a}{c_j^b}c_l^b)x_l \\ z_d &= c_1^b x_1 + c_2^b x_2 + \ldots + c_l^b x_l \end{aligned}$$

From Equation 3.17 it is obvious that d_j^a/d_j^b will equal c_j^a/c_j^b only when the remainder term z_n/z_d is equal to zero. One case where this will occur is when all terms of z_n equal 0, i.e. when

$$\begin{aligned}
(c_1^a - \tfrac{c_j^a}{c_j^b} c_1^b)x_1 &= 0 \\
(c_2^a - \tfrac{c_j^a}{c_j^b} c_2^b)x_2 &= 0 \\
&\vdots \\
(c_l^a - \tfrac{c_j^a}{c_j^b} c_l^b)x_l &= 0
\end{aligned}$$

and these equations are easily solved for all i, $i = 1, \ldots, l$, as follows:

$$\begin{aligned}
(c_i^a - \frac{c_j^a}{c_j^b} c_i^b) &= 0 \\
c_i^a &= \frac{c_j^a}{c_j^b} c_i^b \\
\frac{c_i^a}{c_i^b} &= \frac{c_j^a}{c_j^b}
\end{aligned}$$

This shows that one special multiple dipole case where estimated amplitude ratios will be unbiased is when all dipoles have the same amplitude ratio, as defined below:

$$\frac{c_1^a}{c_1^b} = \frac{c_2^a}{c_2^b} = \cdots = \frac{c_l^a}{c_l^b}$$

I have established that estimated amplitude ratios are unbiased despite head model ($\hat{\mathbf{g}}_j \neq \hat{\mathbf{f}}_j$ and $g_{mj} \neq f_{mj}$) and time-varying dipole magnitude function misspecification ($q_{jt} \neq p_{jt}$) using dipole modeling and least squares fitting in three special cases. These cases are the single dipole case, the case of multiple dipoles with equal amplitude, and the case of multiple dipoles when all dipoles amplitudes are changing the same way (equal amplitude ratios for all dipoles across data sets). In addition, when all dipoles have the same amplitude parameters (i.e., all dipoles are scaled by c^a and c^b), misspecification of the number of dipoles will not lead to biased amplitude ratio estimation.

3.2.5 Reliability

The above results are encouraging, and prove that dipole modeling gives valid results under the special circumstances detailed previously. However, they do not explain the findings of Cardenas, Gerson, and Fein [105], who found that amplitude ratios estimated using dipole modeling were more reliable than the estimated amplitudes, because the proofs in Sections 3.2.1-3.2.4 all assumed the absence of noise. Therefore, the results of Sections 3.2.1-3.2.4 showed only the effect of model misspecification on the bias of amplitude and amplitude ratio estimates, and did not address the variance of amplitude and amplitude ratio estimates. In order to try to explain the findings of Cardenas, Gerson, and Fein [105], I must first look at the definition of reliability.

The reliability of a measure, denoted by r, is

$$r = \frac{\sigma_{bc}^2}{\sigma_{bc}^2 + \sigma_{wc}^2} \tag{3.18}$$

where σ_{wc}^2 is the variance within a class and σ_{bc}^2 is the variance between classes. For the case of dipole modeling, σ_{wc}^2 is the variance of repeated measures (amplitude or amplitude ratio estimates) on the same subject. For the case of dipole modeling, σ_{bc}^2 is the variance of the measure (amplitude or amplitude ratio) across subjects. Equation 3.18 shows that r approaches a perfect value of 1 as σ_{wc}^2 approaches 0. Therefore, r increases as σ_{wc}^2 decreases.

The results of Cardenas, Gerson, and Fein [105] suggest that for the auditory P50 evoked potential, the within class variance of dipole modeling amplitude ratios is smaller than the within class variance of the amplitude parameters estimated using dipole modeling. If I can show that the amplitude ratios have a smaller σ_{wc}^2 than amplitude parameters in general, then I can explain why dipole modeling improved the reliability of the C-T ratio over peak picking, but did not improve the reliability of either the C or T amplitudes over peak picking [105].

In order to examine this question, I must add noise to the model for the given potentials. For simplicity, I will consider the case of one dipole at a single time

point t. Let

$$\mathbf{V}_{gt}^{a} = c^{a} q_t g_m \hat{\mathbf{g}} + \mathbf{e}_g$$

where $\mathbf{e}_g$ is an $n \times 1$ vector of noise due to EEG and EMG artifact. For simplicity, I will assume that $\mathbf{e}_{gk} \sim N(0, \sigma_t^2)\ \forall\ k$, where k indexes electrodes, and that $\mathbf{e}_{gk}$ is independent of $\mathbf{e}_{gk'}$, which means that the noise between electrodes is uncorrelated. This assumption may be valid for widely spaced electrode locations, but is clearly violated for electrodes which are closely spaced. For example, muscle artifact will contaminate all nearby electrodes, resulting in correlated EMG noise between the affected electrodes. Because EMG is not volume conducted, electrodes relatively far from the muscle will not be affected. The noise on the affected electrodes will thus be nearly independent of the noise on the unaffected electrodes.

The presence of noise on $\mathbf{V}_g$ will affect the nonlinear fit of the dipole location and orientation, i.e., the noise will lead to a rougher and more complex multivariate estimation surface with more local minima. The noise may even "shift" the global minimum. Therefore, the $\mathbf{f}(\boldsymbol{\theta}_f, \boldsymbol{\phi}_f)$ found by fitting on noise-free potentials is generally not the same as $\mathbf{f}'(\boldsymbol{\theta}'_f, \boldsymbol{\phi}'_f)$ found by fitting on noisy potentials. I will model the difference between the two fits as noise, i.e. $\mathbf{f}(\boldsymbol{\theta}_f, \boldsymbol{\phi}_f) - \mathbf{f}'(\boldsymbol{\theta}'_f, \boldsymbol{\phi}'_f) = \mathbf{e}_f$, and then I can write:

$$\mathbf{V}_{fi}^{a} = d^{a}(f_m \hat{\mathbf{f}} + \mathbf{e}_f)$$

where $\mathbf{e}_f$ is an $n \times 1$ vector For simplicity, I will assume that $\mathbf{e}_{fk} \sim N(0, \sigma_f^2)\ \forall\ k$, where k indexes electrodes, and that $\mathbf{e}_{gk}$ is independent of $\mathbf{e}_{fk}$, which means that the noise present on the given potentials is not correlated with the difference between the noise free and noisy fits. This assumption is clearly violated, because the noise present on the given potentials *results* in the noisy fit, and so the noise free and noisy fits cannot be uncorrelated. For simplicity, I will also assume that $\mathbf{e}_{fk}$ is independent of $\mathbf{e}_{fk'}$, which means that the noise between electrodes is uncorrelated. This assumption is probably also violated because $\mathbf{e}_{fk}$ is not truly independent of $\mathbf{e}_{gk}$, and because $\mathbf{e}_{gk}$ is not truly independent of $\mathbf{e}_{gk'}$, as discussed above. I use equation 3.1 to solve for d^a,

the amplitude parameter:

$$d^a = \frac{c^a p_i q_i f_m g_m \hat{\mathbf{f}} \cdot \hat{\mathbf{g}} + c^a q_i g_m \hat{\mathbf{g}} \cdot \mathbf{e}_f + p_i f_m \hat{\mathbf{f}} \cdot \mathbf{e}_g + \mathbf{e}_g \cdot \mathbf{e}_f}{p_i^2 f_m^2 + 2 p_i f_m \hat{\mathbf{f}} \cdot \mathbf{e}_f + \mathbf{e}_f \cdot \mathbf{e}_f} \tag{3.19}$$

Equation 3.19 shows that d^a is a function of several random variables. I can rewrite Equation 3.19 as follows, using Ys to denote random variables, and Xs to denote the other variables.

$$d^a = \frac{X_1 + X_2 Y_1 + X_3 Y_2 + Y_3}{X_4 + X_5 Y_4 + Y_5} \tag{3.20}$$

where X_1 is $c^a p_i q_i f_m g_m \hat{\mathbf{f}} \cdot \hat{\mathbf{g}}$, X_2 is $c^a q_i g_m$, X_3 is $p_i f_m$, X_4 is $p_i^2 f_m^2$, and X_5 is $2 p_i f_m \hat{\mathbf{f}}$, and where Y_1 is $\hat{\mathbf{g}} \cdot \mathbf{e}_f$, Y_2 is $\hat{\mathbf{f}} \cdot \mathbf{e}_g$, Y_3 is $\mathbf{e}_g \cdot \mathbf{e}_f$, Y_4 is $\hat{\mathbf{f}} \cdot \mathbf{e}_f$, and Y_5 is $\mathbf{e}_f \cdot \mathbf{e}_f$.

The distributions of the Ys can be determined, some using simple probability theorems. Recall that a linear combination of independent normally distributed random variables is itself normally distributed as $N(\sum_k a_k \mu_k, \sum_k a_k^2 \sigma_k^2)$ [106]. Therefore, I can write the following:

$$\begin{aligned} Y_1 &= \hat{\mathbf{g}} \cdot \mathbf{e}_g = g_1 e_{f1} + g_2 e_{f2} + \cdots + g_n e_{fn} \\ Y_1 &\sim N(\mu \sum_{i=k}^{n} g_k, \sigma_f^2 \sum_{i=k}^{n} g_k^2) \\ Y_1 &\sim N(0, \sigma_f^2) \end{aligned}$$

because $\sum_{i=k}^{n} g_k^2$ is 1 since $\hat{\mathbf{g}}$ is a unit vector. I can similarly determine the distributions of Y_2 and Y_4, and they are

$$\begin{aligned} Y_2 &\sim N(0, \sigma_g^2) \\ Y_4 &\sim N(0, \sigma_f^2) \end{aligned}$$

The random variable Y_3 is more complicated, because it is the sum of random variable products. I know from probability theory the mean and variance of the product of two random variables, but not the distribution. Let

$$W_1 \sim N(\mu_1, \sigma_1^2) \quad W_2 \sim N(\mu_2, \sigma_2^2)$$

Then, if $Z = W_1 W_2$, the mean and variance are defined as

$$\begin{aligned} E(Z) &= \mu_1 \mu_2 \\ Var(Z) &= \sigma_1^2 \sigma_2^2 + \mu_1^2 \sigma_2^2 + \mu_2^2 \sigma_1^2 \end{aligned}$$

I also know from simple probability theory that a linear combination of random variables has a mean $\sum_k a_k \mu_k$ and variance $\sum_k a_k^2 \sigma_k^2$. Therefore, I know the mean and variance of X_3, as shown:

$$Y_3 = \mathbf{e}_g \cdot \mathbf{e}_f = e_{t1} e_{f1} + e_{t2} e_{f2} + \cdots + e_{tn} e_{fn}$$

Let $Z_k = e_{tk} e_{fk}$, then Z_k has mean 0 and variance $\sigma_t^2 \sigma_f^2$. Y_3 is then $\sum_k a_k Z_k$ where $a_k = 1$ for all k. Thus I know that

$$E(Y_3) = 0 \quad Var(Y_3) = \sigma_t^2 \sigma_f^2$$

The distribution function of X_3 has been shown by Khlobystov and Zadiraka [107]. The distribution function of the random variable $\eta(n) = \sum_{k=1}^{n} e_{tk} e_{fk}$, is given by:

$$F_{\eta(n)} = \begin{cases} \frac{1}{2}[1 + (sgn\ x)(1 - \frac{e^{-\frac{|x|}{\sigma_f \sigma_g}}}{2^{m-1}(m-1)!} \times \Phi_{m-1}(\frac{|x|}{\sigma_f \sigma_g}))] & n = 2m \\ \frac{1}{2}[1 + (sgn\ x)\frac{|x|}{\sigma_f \sigma_g}\{K_m(\frac{|x|}{\sigma_f \sigma_g}) \times L_{m-1}(\frac{|x|}{\sigma_f \sigma_g}) + \\ + L_m(\frac{|x|}{\sigma_f \sigma_g}) \times K_{m-1}(\frac{|x|}{\sigma_f \sigma_g})\}] & n = 2m+1 \end{cases} \tag{3.21}$$

where $\Phi_0(w) = 1$, $\Phi_1(w) = w + 2$, $\Phi_m(w) = (w + 2m)\Phi_{m-1}(w) - w\Phi_{m-1}(w)$, $K_m(w)$ and $L_m(w)$ are the Macdonald and Struve functions, respectively [108].

The random variable Y_5 is also complicated, because it is the sum of squared normal variables. I have

$$\begin{aligned} Y_5 &= \mathbf{e}_f \cdot \mathbf{e}_f = e_{f1}^2 + e_{f2}^2 + \cdots + e_{fn}^2 \\ &= \sum_{k=1}^{n} e_{fk}^2 \\ &= \sum_{k=1}^{n} (\mu_{fk} + \sigma_{fk} U_k)^2 \\ &= \sum_{k=1}^{n} \sigma_{fk}^2 (\frac{\mu_{fk}}{\sigma_{fk}} + U_k)^2 \end{aligned}$$

and since $\sigma_{fk} = \sigma_f$ and $\mu_{fk} = \mu_f \; \forall \; k$

$$Y_5 = n\sigma_f^2 \sum_{k=1}^{n} (\frac{\mu_f}{\sigma_f} + U_k)^2$$

where μ_f is the mean of e_f and U_k are independent samples from a standard normal distribution. From [109] I know that the distribution of $\sum_{k=1}^{n}(\mu_f/\sigma_f + U_k)^2$ is the non-central χ^2 distribution with n degrees of freedom and non-centrality parameter $\sum_{k=1}^{n} \mu_f/\sigma_f$. Since I had previously defined $\mu_f = 0$, the non-centrality parameter is 0, and the non-central χ^2 distribution becomes the central χ^2 distribution. Therefore, Y_5 is distributed as $n\sigma_f\chi^2(n)$.

The preceding discussion shows that the distribution of d cannot easily be found analytically, because d is a function of random variables with different distributions. If I further simplify the problem and assume that Y_1-Y_5 are normally distributed, both the numerator and denominator of equation 3.20 become normally distributed random variables. Previous research [92, 93, 105] has shown that the variance of the ratio of independent normally distributed random variables is infinite, and d would thus have a large variance and small signal to noise ratio.

Let us now turn to the discussion of amplitude ratios. If I let a second set of noisy data be described as

$$\mathbf{V}_g^b = c^b q_i g_m \hat{\mathbf{g}} + \mathbf{e}_g^b$$

where I assume that this data were generated by the same dipole, c^b is the amplitude of the dipole, and $\mathbf{e}_g^b$ is the EEG and EMG artifact present on the data. The fit is modeled as

$$\mathbf{V}_f^b = d^b(f_m p_i \hat{\mathbf{f}} + \mathbf{e}_f^b)$$

The amplitude ratio is then

$$\frac{d^a}{d^b} = \frac{c^a p_i q_i f_m g_m \hat{\mathbf{f}} \cdot \hat{\mathbf{g}} + c^a q_i g_m \mathbf{g} \cdot \mathbf{e}_f + p_i f_m \hat{\mathbf{f}} \cdot \mathbf{e}_g + \mathbf{e}_g \cdot \mathbf{e}_f}{c^b p_i q_i f_m g_m \hat{\mathbf{f}} \cdot \hat{\mathbf{g}} + c^b q_i g_m \mathbf{g} \cdot \mathbf{e}_f^b + p_i f_m \hat{\mathbf{f}} \cdot \mathbf{e}_g^b + \mathbf{e}_g^b \cdot \mathbf{e}_f^b} \tag{3.22}$$

Equation 3.22 shows that the amplitude ratio is a function of several random variables. I can rewrite equation 3.22 as follows, using Ys to denote random variables,

and Xs to denote the other variables.

$$\frac{d^a}{d^b} = \frac{X_1 + X_2Y_1 + X_3Y_2 + Y_3}{X_1^b + X_2^bY_1^b + X_3Y_2^b + Y_3^b}$$

One can easily show that Y_1^b and Y_2^b are normally distributed, and that the distribution of Y_3^b is described by Equation 3.21. If for simplicity I assume that Y_3^b is normally distributed, then d^a/d^b becomes a ratio of normally distributed random variables. As previously mentioned, such a ratio has infinite variance.

I have shown that the variances of amplitude parameters and amplitude ratios estimated by dipole modeling are not easily determined, even when simplifying assumptions (such as the distributions of the noise vectors) are made. In addition, real EEG and EMG artifacts are not normally distributed with 0 mean and same variance across measurement channels (see above discussion), and the noise components $\mathbf{e}_g$ and $\mathbf{e}_f$ are not independent, but are at least weakly correlated with each other. Therefore, the mean, variance, and distributions of dipole modeling amplitudes and amplitude ratios are even more complicated than I have presented.

In chapter 2, it was shown that the ratio of independent normal variates had infinite variance. The violation of independence in the present chapter may in fact lead to a decrease in the variance of the ratio measurement. For example, I can define a random variable Y as the ratio of the random variable X with itself, i.e. $Y = X/X = 1$ for any sample X. In this case, the variance of the random variable Y is 0, because X is perfectly correlated with itself. Therefore, if a random variable is the ratio of two correlated random variables, the variance of the ratio may not be infinite.

Because of the difficulty in solving this problem analytically, and because of the difficulty in estimating the correlation between the noise vectors, I have designed a simulation study in order to determine the relative variances of absolute amplitudes and amplitude ratios estimated using dipole modeling. I can then empirically evaluate whether amplitude ratios are more reliable than amplitude parameters, when estimated using dipole modeling.

I will estimate the variance for the absolute amplitude and amplitude ratio under several types of model misspecification in the presence of noise. I will addi-

tionally determine the effect of dipole location and orientation on the variances by looking at several dipoles and dipole pairs. The simulations and results are described in the following chapter.

Chapter 4

Simulations

4.1 Introduction

Chapter 2 showed that dipole modeling led to increased reliability of the auditory P50 conditioning-testing ratio (an amplitude ratio) over peak picking, but did not lead to increased reliability of the estimated conditioning and testing amplitudes. In chapter 2 it was shown that the process of fitting several data sets and "pooling" the noise across data sets did not account for the increase in reliability, as originally proposed. The use of multiple channels of data did not appear to cause the increase in reliability either, as the reliabilities of the amplitudes did not increase as the ratio reliabilities did. At the end of chapter 2 I proposed that misspecification of the dipole model may affect the variability of amplitudes more than ratios.

Chapter 3 investigated the effect of model misspecification on the amplitude and ratio estimates, and showed that in several cases, model misspecification led to biased amplitudes but unbiased ratios. Chapter 3 also showed that the variability of amplitudes and ratios was difficult to determine analytically, leaving only simulations as a means to test the hypothesis that model misspecification leads to increased variability of amplitudes as compared to ratios.

I am interested in determining errors due to model misspecification when dipole modeling (via minimization of a least squares criterion, such as the scaled residual sum of squares, defined in Section 1.3.3) is used to estimate covariate effects

on amplitude and the derived amplitude ratio. I shall treat the parameters representing the covariate effects on amplitude (hereafter called "amplitude parameters", for simplicity) as linear variables in the problem, and dipole location, orientation, and time-varying dipole magnitude function are treated as nonlinear variables (this "splitting" of the problem into linear and nonlinear parts was discussed in Sections 1.3.2 and 1.3.3).

This chapter describes the simulations used to test the following hypotheses:

1 The coefficient of variation (COV–defined as the mean divided by the standard deviation) of amplitude ratios estimated using dipole modeling is higher than COVs of estimated amplitude parameters in the presence of model misspecification (head model misspecification, time-varying magnitude function misspecification, and misspecification of the number of dipoles) and averaged EEG noise.

2 The COV of dipole modeling amplitude parameter estimates will increase as the signal to noise ratio of the data increases (i.e., the amount of EEG noise present decreases).

3 The COV of amplitude parameters estimated using dipole modeling will increase as the "true" dipole generator becomes more eccentric, because the homogeneous sphere head model better approximates the head for eccentric dipoles (i.e., head model misspecification decreases for eccentric dipoles).

Three types of model misspecification were simulated during estimation of the variances; head model misspecification, time-varying amplitude function misspecification, and misspecification of the number of dipoles. I generated data in the 3-shell skull shape model using an averaged and filtered P50 evoked potential as a template for the time-varying amplitude function. Real averaged EEG "noise" was added to these simulated data to generate several simulated averages for each dipole configuration. Dipole modeling of these data sets using a homogeneous sphere model and

decaying sinusoid amplitude function misspecified both the head model and amplitude function. One or two dipoles were fit to data generated by two synchronous dipoles in order to simulate misspecification of the number of dipoles. The means, standard deviations, and coefficients of variation (COV) of the dipole amplitudes and amplitude ratios were computed.

Because of my interest in using the results of this chapter to understand chapter 2, I simulated the proposed generators of the auditory P50 evoked response. The generators of the auditory P50 have been widely debated in the literature [21, 110, 111, 112, 49, 113], and there is conflicting evidence suggesting bilateral generators in (a) the central nuclei of the thalamus, (b) hippocampus, or (c) auditory cortex. Therefore, I simulated dipoles in each of these locations, and investigated them singly and in synchronously active bilateral pairs.

4.2 Methods

Simulated evoked potentials were generated at 30 scalp electrodes, using a 3-shell skull shape model. The dipole locations and orientations used are listed in Table 4.1. These locations and orientations were estimated using the coordinates from a stereotaxic atlas of the human brain [114] and scaling to a head radius of 1. The electrode locations I used are listed in Table 4.2. These electrode locations correspond to those currently used to collect and analyze auditory P50 in George Fein's laboratory. These locations were chosen assuming a spherical head model, but the real skull shape used to generate the data does not have the same symmetry as a sphere. Because of the irregularities in the skull shape model, the electrode locations were not in these exact coordinates. The adjusted locations (relative to a spherical model) are listed in Tables 4.3. Figure 4.1 shows these electrode locations superimposed on the x-y plane. Although the generator dipole locations listed in Table 4.1 are exactly symmetric with respect to the center of the skull shape, because of the asymmetry of the head, the corresponding equivalent dipoles in a sphere will not be exactly symmetric.

The electrode weight function for the realistic skull model was generated

Table 4.1: Simulated Neural Generators

Dipole #	Neural Generator	Location			Orientation	
		θ_1	θ_2	θ_3	ϕ_1	ϕ_2
1	left nucleus centralis medialis	-0.04	0.13	0.07	20	45
2	right nucleus centralis medialis	-0.04	-0.13	0.07	20	-45
3	left hippocampus	-0.28	0.30	-0.02	30	-45
4	right hippocampus	-0.28	-0.30	-0.02	30	45
5	left auditory cortex	0.21	0.71	0.04	30	-90
6	right auditory cortex	0.21	-0.71	0.04	30	90

The locations are scaled by the head radius (and are thus unitless), where the direction of θ_1 is through the nasion, θ_2 is through the left ear, and θ_3 is through the vertex. The orientations are given in degrees where ϕ_1 is colatitude and ϕ_2 is longitude.

Table 4.2: Electrode Locations

Label	ψ_1	ψ_2	Label	ψ_1	ψ_2
Fz	36.00	0.00	FCz	18.00	0.00
Cz	0.00	0.00	Pz	36.00	180.00
Fp1	72.00	18.00	Fp2	72.00	-18.00
F3	49.44	40.70	F4	49.44	-40.70
F5	60.72	49.00	F6	60.72	-49.00
F7	72.00	54.00	F8	72.00	-54.00
C1	18.00	90.00	C2	18.00	-90.00
C3	36.00	90.00	C4	36.00	-90.00
T3	72.00	90.00	T4	72.00	-90.00
T5	72.00	126.00	T6	72.00	-126.00
P3	49.44	139.30	P4	49.44	-139.30
P5	60.72	131.00	P6	60.72	-131.00
FC3	40.00	61.00	FC4	40.00	-61.00
CP3	40.00	119.00	CP4	40.00	-119.00
O1	72.00	162.00	O2	72.00	-162.00

Electrode locations given in spherical coordinates, where all electrodes have a radius of 1.0 (scaled to the head radius), and ψ_1 and ψ_2 are colatitude and longitude.

Table 4.3: Electrode Locations: locations adjusted for skull shape

Label	ψ_1	ψ_2	Label	ψ_1	ψ_2
Fz	39.44	4.42	FCz	20.75	8.16
Cz	3.09	97.02	Pz	34.60	-174.37
Fp1	72.82	18.11	Fp2	72.81	-18.93
F3	51.62	41.77	F4	51.64	-42.16
F5	61.15	47.79	F6	61.13	-48.47
F7	71.67	53.48	F8	71.63	-54.68
C1	16.38	91.23	C2	16.83	-91.10
C3	36.70	91.11	C4	36.88	-91.19
T3	72.58	90.96	T4	72.69	-91.12
T5	75.88	126.77	T6	75.90	-124.93
P3	49.25	137.16	P4	49.40	-138.86
P5	63.97	132.32	P6	64.01	-130.79
FC3	39.36	59.37	FC4	39.44	-59.79
CP3	41.05	118.82	CP4	40.69	-121.34
O1	70.99	162.02	O2	71.16	-164.17

Electrode locations given in spherical coordinates, where all electrodes have a radius of 1.0 (scaled to the head radius), and ψ_1 and ψ_2 are colatitude and longitude.

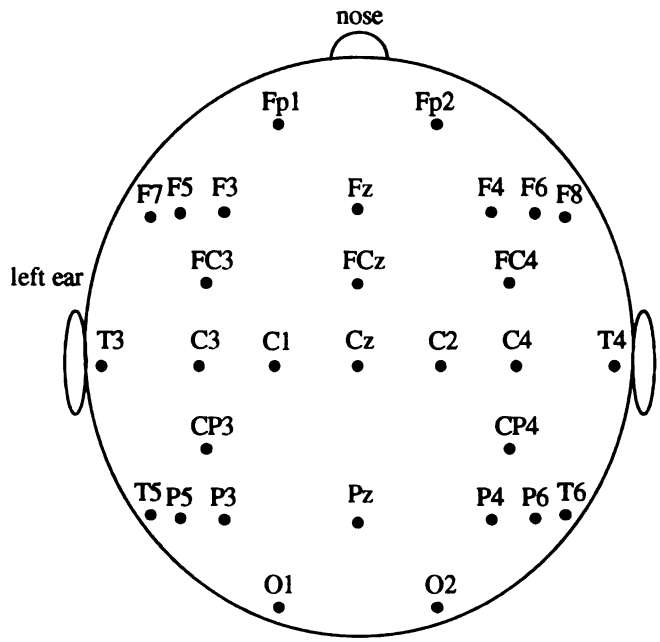

Figure 4.1: Planar projection of the electrode locations for simulations

using a boundary element model [115] based on a Computed Tomography (CT) scan of an adult human skull. The 3-shell skull shape model consisted of three concentric skulls. The radii and conductivities of the skull were the same as those used by Ary et al. [11]. The inner radii of the shells were determined in the following manner. A sphere was fit to all the nodes of the outer skull shape model, and the radius of this sphere was scaled to 1. In order to construct the skull shells, the skull shape model was scaled down such that the best-fitting spheres to the nodes had radii (inner to outer) of 0.8, 0.85, and 0.92. The conductivities of the shells were 1.0, 0.0125, and 1.0, respectively. A dipole source was simulated using a point dipole. The scalp potentials were computed at the locations listed in Table 4.3.

Several data sets were generated using these simulated dipoles. The data sets and the dipoles generating them are shown in Table 4.4. Each data set consisted of a pair of evoked potentials, corresponding to the conditioning and testing responses of the auditory P50 collected in a paired click paradigm. Two amplitude ratios were simulated for each data set, corresponding to normal P50 suppression (i.e., amplitude ratios between .25 and .50) and abnormal P50 suppression (i.e., amplitude

Table 4.4: Data Sets Simulated

Data Set #	Generator # used	Description
1	1	left nucleus centralis medialis
2	3	left hippocampus
3	5	left auditory cortex
4	1 and 2	bilateral thalamus
5	3 and 4	bilateral hippocampus
6	5 and 6	bilateral auditory cortex

ratios between .75 and 1.0). The simulated magnitude function was an averaged and digitally filtered P50 evoked potential recorded from Cz-left ear from a representative subject.

Real EEG noise from an auditory P50 evoked potential recording was added to each simulated data set. The EEG noise was collected at 30 scalp electrodes from subjects while they were listening to paired clicks at 60 dB SL. Noise was collected at a 2000 Hz sampling rate for 256 ms (512 data points), beginning 500 ms after the second click. Approximately 120 single trials (the same number of single trials in a typical P50 average) were collected from each of 2 normal hearing subjects. The noise trials were multiplied by an amplitude factor to create data with the desired signal to noise ratio (SNR). We used two values of the SNR: low (0.1) and high (0.5). The estimated SNR was defined as follows. Let $\hat{\sigma}_N^2$, $\hat{\sigma}_S^2$, and $\hat{\sigma}_V^2$ be unbiased estimators of the noise, signal, and total power.

$$\begin{aligned}
\hat{\sigma}_N^2 &= 1/[u(m-1)] \sum_j \sum_t [V_j(t) - \bar{V}(t)]^2 \\
\hat{\sigma}_S^2 &= (1/u) \sum_t \bar{V}^2(t) - (\hat{\sigma}_N^2/m) \\
\hat{\sigma}_V^2 &= 1/(mu) \sum_j \sum_t V_j^2(t)
\end{aligned}$$

where $\bar{V}(t) = (1/m)\Sigma_j V_j(t)$, m is the number of single trials, u is the number of time points, and $V_j(t)$ is the measured voltage at a single electrode for trial j at time t. The estimator of the SNR is then

$$\hat{SNR} = \frac{\hat{\sigma}_S^2}{\hat{\sigma}_N^2} = \frac{\hat{\sigma}_V^2 - \hat{\sigma}_N^2}{\hat{\sigma}_N^2} \tag{4.1}$$

The derivation of the SNR estimator and its asymptotic distribution are described in [116]. Examination of Equation 4.1 shows that this SNR estimate is based on the signal at a single electrode. The SNRs I used, 0.1 and 0.5, were defined at the vertex electrode (Cz). Therefore, electrodes that had higher maximal amplitude than Cz would have higher SNR, and electrodes with lower amplitude than Cz would have lower SNR.

A simulated data set was generated by first randomly choosing a sample of 200 simulated noise trials, and randomly choosing a set of 64 successive time points (32 ms, the approximate duration of P50 and the length of the P50 evoked potential used as a waveform template in the simulations) from each sampled trial. The sample of 200 noise trials was randomly chosen with replacement from the 120 single trials in each noise data set. Although the number of single trials in my noise data sets is small, this should not pose a problem. When sampling with replacement from a finite population of noise trials, two different random samples (of size 200) are independent (conditional on that finite population), just as are two random samples from an infinite population.

The scalp representation of the dipoles were then computed from the simulated amplitude waveform (recall that the simulated amplitude waveform was an averaged and filtered P50 evoked potential recorded from Cz-left ear) with the weighting functions generated in a skull shape model. The weighting functions were scaled by the conditioning amplitude parameter so that each simulated conditioning response had maximal amplitude of 4 μV at the vertex electrode. The scalings, or "true" values for the conditioning amplitude parameters, were 28.35, 36.17, 51.70, 14.18, 18.09, and 25.85 for Data Sets 1, 2, 3, 4, 5, and 6 (see Table 4.4), respectively. The "true" values for the testing amplitude parameters are simply the conditioning amplitude parameter multiplied by the C-T ratio. The noise trials were then added to the simulated data and averaged. Since the SNRs defined above are essentially *single trial*

Table 4.5: Combinations of SNR and C-T ratio for the Data Sets Simulated

	Normal C-T ratio	Schizophrenic C-T ratio
Low SNR	Data Sets 1-6	Data Sets 1-6
High SNR	Data Sets 1-6	Data Sets 1-6

SNRs, the resulting SNRs after averaging are approximately,

$$\text{low SNR} = 0.1\sqrt{200} = 1.41$$
$$\text{high SNR} = 0.5\sqrt{200} = 7.07$$

Figure 4.2 shows sample simulated data for the conditioning response at the high SNR. Data sets 1, 2, and 3 are superimposed (corresponding to generators 1, 3, and 5), and each plot represents data at a different electrode. Figure 4.3 shows data sets 4, 5, and 6 superimposed (corresponding to generators 1 and 2, 3 and 4, and 5 and 6 synchronously active). Figure 4.4 shows data generated by dipole 5 at the vertex electrode. The top plot shows the conditioning and testing responses at the high SNR, and the bottom plot shows the conditioning and testing responses at the low SNR.

Table 4.5 shows the combinations of SNR and C-T ratio simulated. There are four combinations of SNR and C-T ratio for each Data Set (each Data Set contains the conditioning and testing responses due to a specific generator or pair of generators, as detailed in Table 4.4). The SNR/C-T combinations are: low SNR, low C-T ratio; low SNR, high C-T ratio; high SNR, low C-T ratio; high SNR, high C-T ratio. Twenty simulated averages at each SNR/C-T ratio combination were created for each generator or generator pair and noise subject (i.e., 160 simulated EP averages for each generator or generator pair; 20 replications $\times$ 4 SNR/C-T ratio combinations $\times$ 2 noise subjects). There were 960 simulated auditory P50 conditioning-testing averages created (20 replications $\times$ 4 SNR/C-T ratio combinations $\times$ 6 P50 generator configurations $\times$ 2 noise subjects).

The dipole components model was then applied to each simulated average, using a decaying sinusoid time-varying magnitude function. The conditioning and

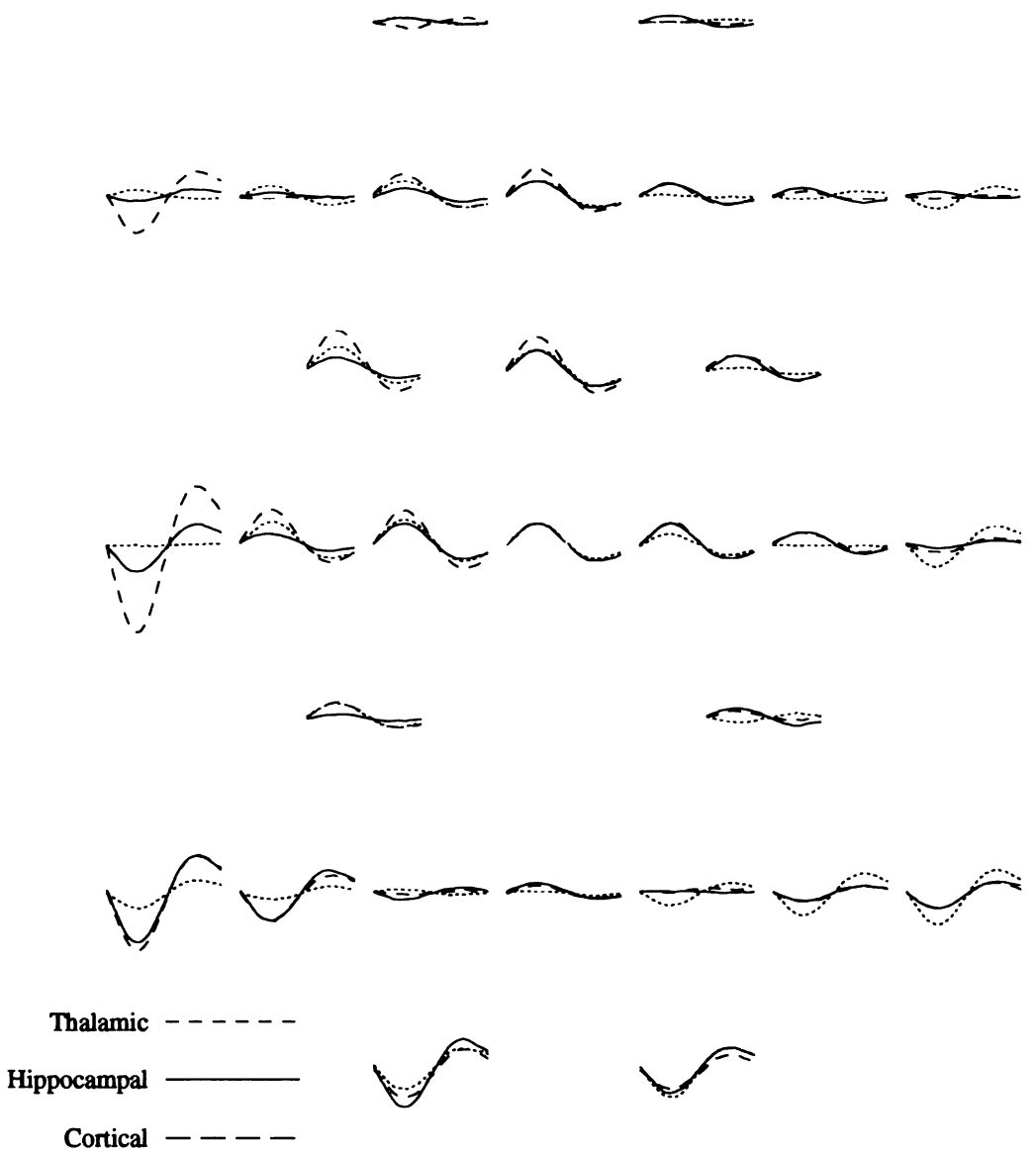

Figure 4.2: Simulated data sets for generators 1, 3, and 5
The conditioning (C) response for a simulated average generated by dipole 1 is shown by the dotted line, the C response generated by dipole 3 is shown by the solid line, and the C response generated by dipole 5 is shown by the dashed line. Each plot represents the signal as seen at a different electrode, and the plots are arranged to approximate the position of the corresponding electrode. All simulated averages are at the high SNR and are scaled so that the amplitude at the vertex is approximately 4 μV.

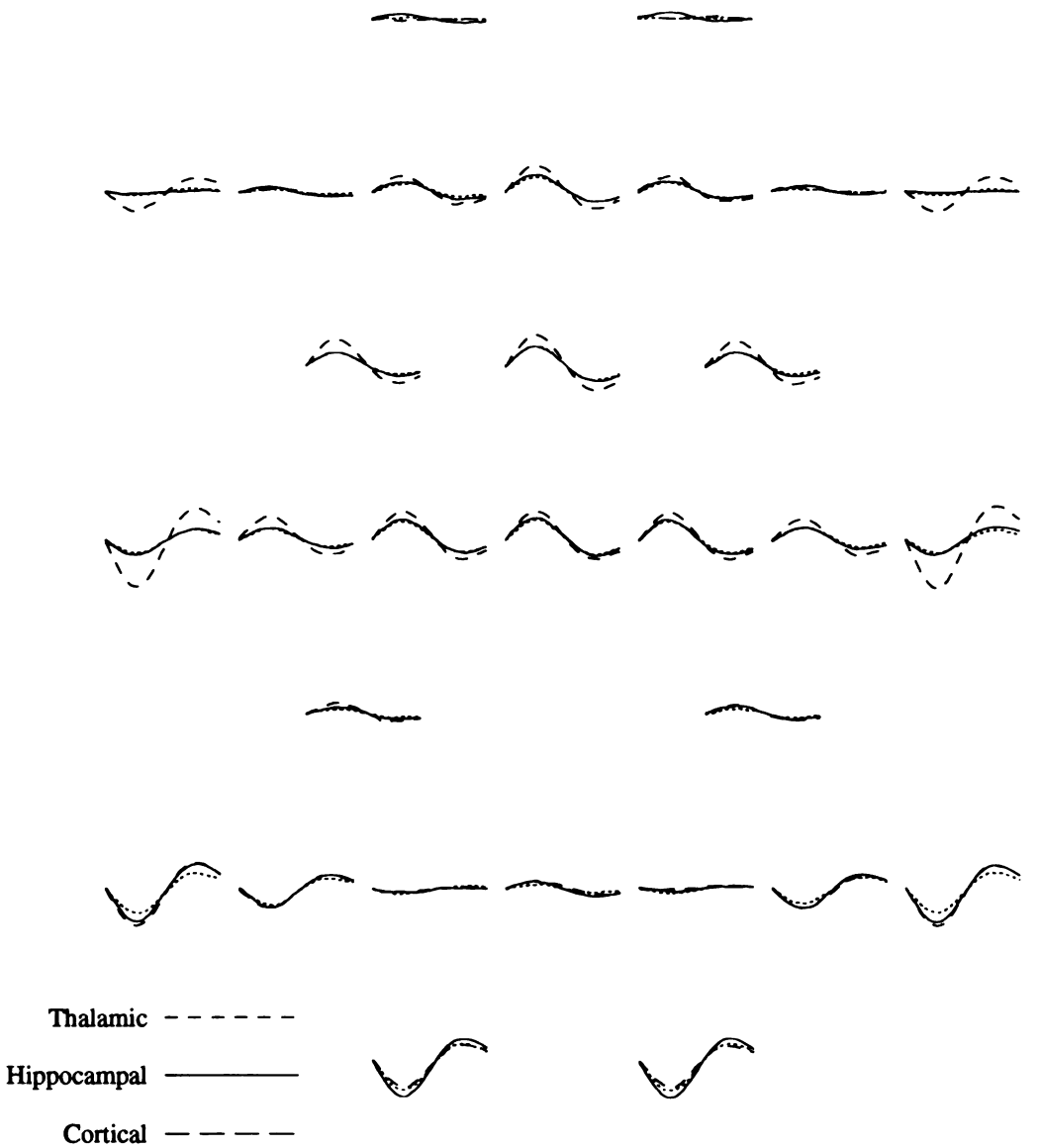

Figure 4.3: Simulated data sets for generators 1 & 2, 3 & 4, and 5 & 6
The conditioning (C) response for a simulated average generated by synchronously active dipoles 1 and 2 is shown by the dotted line, the C response generated by dipoles 3 and 4 is shown by the solid line, and the C response generated by dipoles 5 and 6 is shown by the dashed line. Each plot represents the signal as seen at a different electrode, and the plots are arranged to approximate the position of the corresponding electrode. All simulated averages are at the high SNR and are scaled so that the amplitude at the vertex is approximately 4 μV.

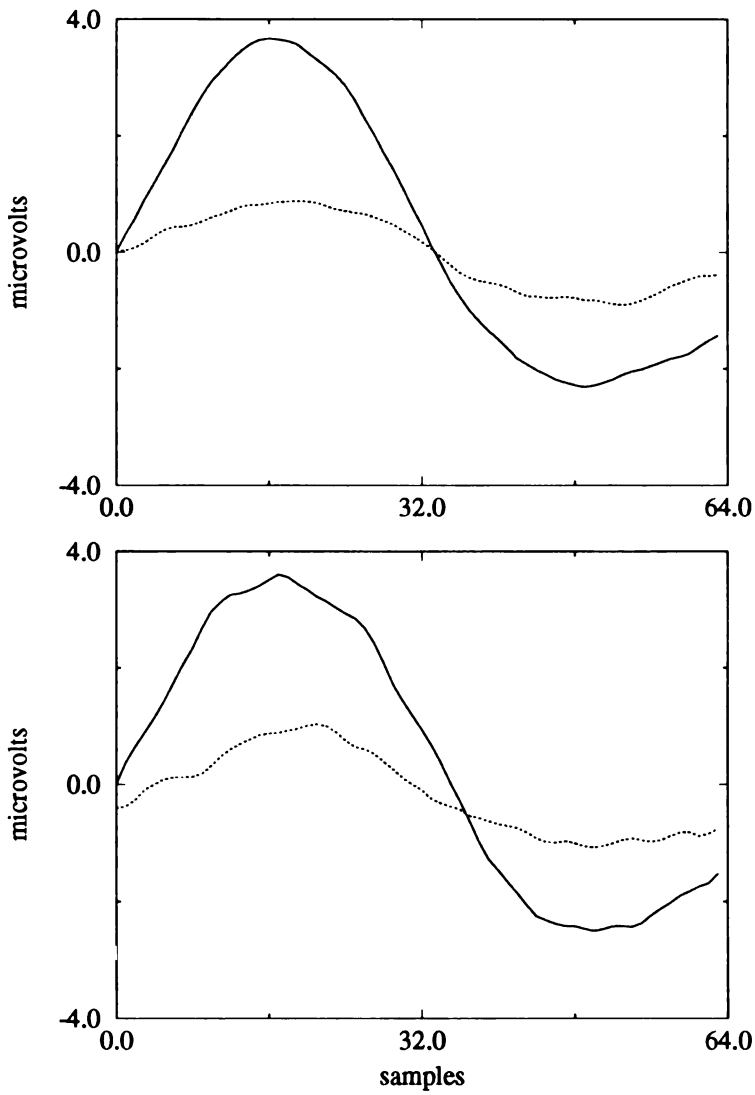

Figure 4.4: Conditioning and testing responses at high and low SNR
The top plot shows the conditioning and testing responses at the vertex for a simulated average generated by dipole 5 at the high SNR. The bottom plot shows the conditioning and testing responses at the vertex for a simulated average generated by dipole 5 at the low SNR. The conditioning response is shown by the solid line, and the testing response is shown by the dotted line. The two simulated averages shown in this figure were created from the same noise subject's data.

testing responses in each simulated average were fit simultaneously, and the responses were constrained to have the same generator location, orientation, and decaying sinusoid. The generators were allowed to vary in amplitude between the conditioning and testing responses (i.e., conditioning and testing amplitude parameters were fit).

The simulated averages corresponding to Data Sets 1-3 were fit with a single dipole. The simulated averages corresponding to Data Sets 4-6 were fit with a single dipole (misspecification of number of dipoles) and with two dipoles constrained to be bilateral and somewhat symmetric. For the single dipole case, the fitted dipole model was

$$\mathbf{V}_t^e = q_t^e \mathbf{f}(\boldsymbol{\theta}, \boldsymbol{\phi})$$

where

$$q_t^e = c^e \alpha sin[\frac{2\pi}{\lambda}(t-\tau)]exp[-\beta(t-\tau)]$$

and where $\mathbf{f}(\boldsymbol{\theta}, \boldsymbol{\phi})$ is defined for a homogeneous sphere head model as in Equation 1.9, e indexes the conditioning and testing experimental conditions, and I constrained $\alpha = 1$ so that the model was identifiable. For the two dipole case, the fitted dipole model was

$$\mathbf{V}_t^e = q_{1t}^e \mathbf{f}_1(\boldsymbol{\theta}_1, \boldsymbol{\phi}_1) + q_{2t}^e \mathbf{f}_2(\boldsymbol{\theta}_2, \boldsymbol{\phi}_2)$$

where

$$q_{jt}^e = c_j^e \alpha_j sin[\frac{2\pi}{\lambda_j}(t-\tau_j)]exp[-\beta_j(t-\tau_j)]$$

The bilateral and somewhat symmetric constraint required one dipole to be in the left hemisphere, and the other to be in the right hemisphere. This was accomplished by adding a penalty term to the scaled residual sum of squares (SRSS, defined in Section 1.3.3) during the fitting of the nonlinear parameters. The term was 0 when the generators were exactly bilaterally symmetric (in the sphere), and increased exponentially as the dipoles deviated from perfect symmetry. The two dipoles were also required to have similar colatitude and nearly opposite longitude, which was accomplished by adding a second penalty term. The term was 0 when the orientations of the generators perfectly satisfied the constraint, and increased

exponentially as the dipole orientations violated that constraint. The dipoles were also required to have similar time-varying moment functions. This constraint was achieved by adding a third penalty term to the SRSS. This term was 0 when the decaying sinusoid parameters (λ and τ, see Equation 1.11), were the same for both dipoles, and increased as the decaying sinusoid parameters diverged from each other. The penalties were defined as follows. Let *dist* be the physical "distance" in centimeters (assuming a 10 cm radius sphere) between the two dipoles after negating θ_{j2} of one of the dipoles (this is done to enforce the left-right hemisphere constraint), let *or* be the difference between the orientations, and let $tdiff$ be the difference between the time-varying moment functions. Letting ϕ_{jk} be the dipole orientation for dipole j, where k indexes colatitude or longitude, I can define ξ_{jd} for dipole j as follows (similar to Equation 1.10).

$$\begin{aligned} \xi_{j1} &= sin\phi_{j1}cos\phi_{j2} \\ \xi_{j2} &= sin\phi_{j1}sin\phi_{j2} \\ \xi_{j3} &= cos\phi_{j1} \end{aligned}$$

I then define *dist*, *or*, and $tdiff$ to be:

$$dist = 10\sqrt{(\theta_{11}-\theta_{21})^2+(\theta_{12}+\theta_{22})^2+(\theta_{13}-\theta_{23})^2}$$

$$or = 10\sqrt{(\xi_{11}-\xi_{21})^2+(\xi_{12}+\xi_{22})^2+(\xi_{13}-\xi_{23})^2}$$

$$tdiff = (\lambda_1-\lambda_2)+(\tau_1-\tau_2)$$

where θ_{jd} is the location parameter in direction d for dipole j. The bilaterally symmetric penalty *dpen*, the orientation penalty *orpen*, and the time function penalty *tpen* are defined as:

$$dpen = \frac{e^{dist}-1}{10^{1/(e^{dist}-1)}} \tag{4.2}$$

$$orpen = \frac{e^{or} - 1}{1000000^{1/(e^{or}-1)}} \tag{4.3}$$

$$tpen = \frac{e^{tdiff} - 1}{1000} \tag{4.4}$$

The sizes of the penalties added to the SRSS versus the size of *dist*, *or*, and *tdiff* are shown in Figure 4.5. These constraints are necessary when modeling data generated by somewhat symmetric dipoles whose orientations are such that the resulting topographical map is very similar to a single dipole map (see Figure 4.3). In preliminary studies when fitting two dipoles to such a map, when noise was present on the data, one dipole was fit centrally and explained most of the variance in the data. The other dipole location varied, but its contribution to the fit was to explain mostly noise. These penalty functions were developed so that in such a case, the two dipoles made more equal contributions to the fit and explained primarily signal, not noise. These penalty functions worked well in constraining solutions (i.e., the locations, orientation, and time-varying magnitude parameters were correctly estimated) when tested on simulated data where the dipoles were both perfectly symmetric and somewhat symmetric.

Dipole modeling was used to estimate the amplitude parameters for each of twenty replications (constructed using a single subject's noise data) of each generator or generator pair set at each SNR for both normal and abnormal (schizophrenic) suppression. C-T ratio estimates were computed by dividing the testing amplitude parameter estimate by the conditioning amplitude parameter estimate (C-T ratio $= c^2/c^1$). This process was repeated using the the second noise subject's data, in order to ensure that my results were not an anomaly of one subject's noise, but were consistent across noise data sets. In order to reduce and possibly eliminate the frequency of convergence to local minima, simulated annealing was used to estimate the nonlinear parameters (location, orientation, and decaying sinusoid) [73].

For each SNR, true C-T ratio, noise subject, and dipole model (one or two dipoles fit) combination, the means ($\bar{x}$), standard deviations (SD), and coefficients of variation (COV) were computed for the conditioning amplitude estimates, the

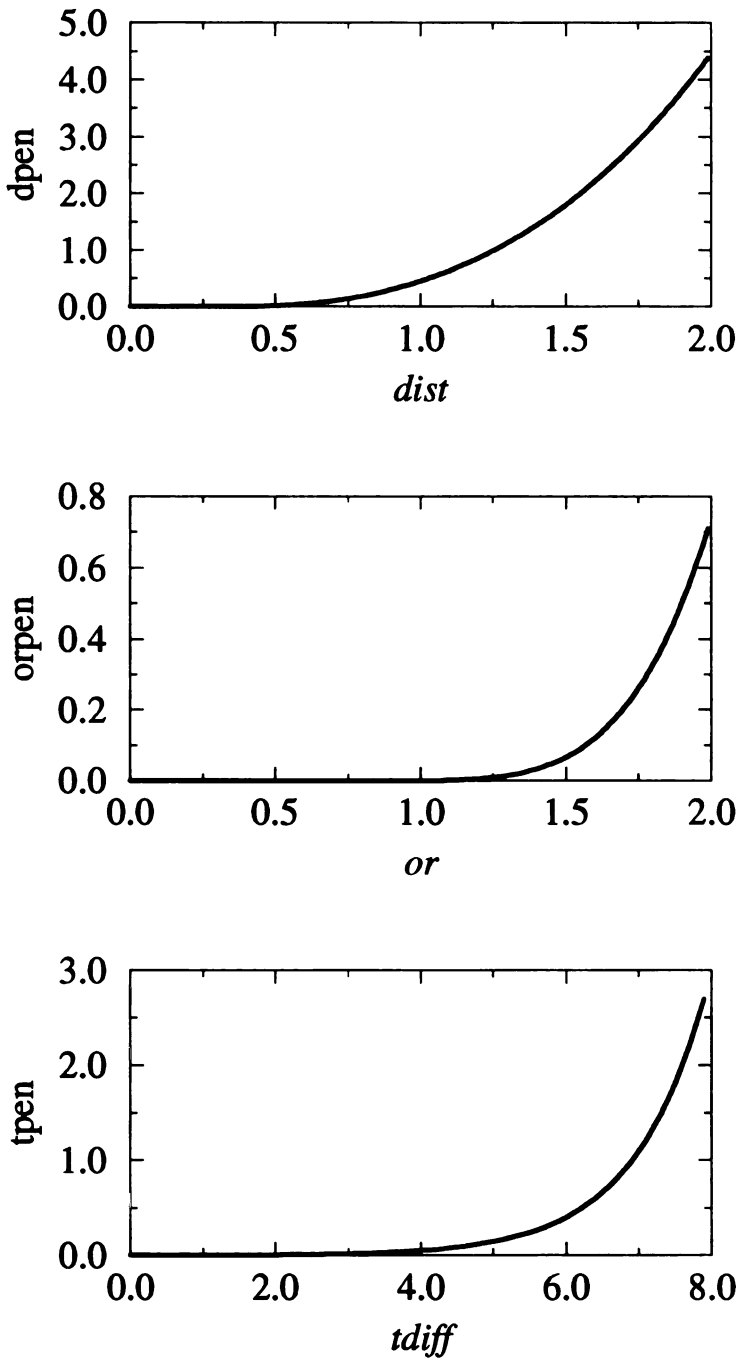

Figure 4.5: Penalty functions for the bilateral constraint
The top plot shows the penalty added to the SRSS as the variable *dist* increases. The middle plot shows the penalty as the variable *or* increases. The bottom plot shows the penalty as the variable $tdiff$ increases. When *dist* = 1, the dipoles are 1 cm (assuming a 10 cm head) from perfect symmetry. When *or* = 1.7, colatitude and longitude are both 7.5° off from perfect symmetry. When $tdiff = 4$, the decaying sinusoid parameters are 4 time points off from being the same.

testing amplitude estimates, and the C-T ratio estimates. The *COV* represents the magnitude of the *SD* as compared to the mean, and relatively larger *COV*s indicate relatively smaller variances as compared to the mean. For these simulations, the *COV* was computed because the variances of the amplitude parameters could not be directly compared to the variances of the derived amplitude ratios, due to the differences in the means (recall that I was interested in the relative variances because of the effect of variances on the intraclass correlation coefficient). For example, the mean conditioning amplitude parameter for Data Set 1 (thalamic dipole generator) was approximately 25, and the mean "normal" derived ratio was 0.25. In this example, the variance of the ratio is almost guaranteed to be smaller than the variance of the conditioning amplitude, and a direct comparison is meaningless. The *COV* scales the variances to their means, so that meaningful comparisons can be made. The *COV* was used to test the hypotheses stated at the beginning of the chapter.

Because the *COV* is a ratio of summary statistics, it is unlikely to be normally distributed. In fact, if the amplitude and amplitude ratio estimates were normally distributed, then the $COV/\sqrt{n}$ (where n is the number of samples) follows the t distribution with $n-1$ degrees of freedom [106]. Simple t-tests and analysis of variance assume a normal distribution, however, so these statistical methods cannot be used for hypothesis testing of *COV*s.

I used a randomization technique for hypothesis testing that does not require knowledge of the distribution of the *COV*. Let $\mathbf{COV}_a$ be a vector of *COV*s for group a, and let $\mathbf{COV}_b$ be a vector of *COV*s for group b. The hypotheses are $H_o : \mathbf{COV}_a - \mathbf{COV}_b = 0$ and $H_1 : \mathbf{COV}_a - \mathbf{COV}_b > 0$, i.e. the null hypothesis states that there is no difference in the *COV*s between groups, and the alternative hypothesis states that the *COV*s for group a are larger than the *COV*s for group b.

The hypotheses are tested as follows. Let

$$\delta_o = \frac{1}{N}\sum_{i=1}^{N}(COV_{ai} - COV_{bi}) \tag{4.5}$$

where δ_o is the mean observed difference between the group a and b *COV*s, COV_{ai} is the ith *COV* for group a, COV_{bi} is the ith *COV* for group b, and N is the number of observations in each group. Let $\mathbf{COV}_{r_1}$ and $\mathbf{COV}_{r_2}$ be random permutations of the

original $\mathbf{COV}_a$ and $\mathbf{COV}_b$, where an element of $\mathbf{COV}_a$ could be in either $\mathbf{COV}_{r_1}$ or $\mathbf{COV}_{r_2}$ (i.e., the groups are not preserved in the random permutation). Then let

$$\delta_r = \frac{1}{N}\sum_{i=1}^{N}(COV_{r_1 i} - COV_{r_2 i}) \tag{4.6}$$

where δ_r is the mean difference between the randomly permuted COV vectors, $COV_{r_1 i}$ is the ith element of $\mathbf{COV}_{r_1}$, $COV_{r_2 i}$ is the ith element of $\mathbf{COV}_{r_2}$, and N is the length of the randomly permuted vectors.

If there is truly a difference between groups, then $COV_{ai} - COV_{bi}$ should be positive for most i, and the sum in Equation 4.5 should be positive, resulting in a large positive δ_o. If there is not a difference between groups, then $COV_{ai} - COV_{bi}$ will take positive and negative values for different i, and the sum in Equation 4.5 will be close to zero. Because the randomly permuted vectors $\mathbf{COV}_{r_1}$ and $\mathbf{COV}_{r_2}$ do not preserve the groups, δ_r should always be close to zero. Therefore, if no difference exists between groups, δ_o will be greater than δ_r for some random permutations, and δ_o will be less than δ_r for other random permutations. If there is a difference between groups, δ_o will be greater than δ_r for most random permutations.

A p-value for this test is obtained by constructing many (I used 1000) random permutations of the original COV_{ai} and COV_{bi}, and comparing δ_o to δ_r. If δ_o is greater than δ_r for 995 of the permutations, then the p-value is 0.005 and the alternative hypothesis ($H_1 : \mathbf{COV}_a - \mathbf{COV}_b > 0$) is accepted. If δ_o is greater than δ_r for only 600 of the random permutations, then the p-value is 0.400 and the null hypothesis is accepted. In Section 4.3 (Results), $p < 0.001$ indicates that δ_o was greater than δ_r for all 1000 of the permutations, i.e. there was less than 1 chance in 1000 that $\delta_o < \delta_r$.

I studied the effect of SNR, C-T ratio, dipole eccentricity, and number of dipoles included in the fitting model. When testing the hypothesis that COVs computed from high SNR simulated averages were larger than COVs computed from low SNR simulated averages, the high SNR COVs were grouped into $\mathbf{COV}_a$ and the low SNR COVs were grouped into $\mathbf{COV}_b$. When the effect of C-T ratio was tested, all COVs estimated from simulated averages with "schizophrenic" suppression were grouped into $\mathbf{COV}_a$ and all COVs estimated from simulated averages with normal suppression were grouped into $\mathbf{COV}_b$. When the effect of dipole eccentricity was

tested, all COVs estimated from simulated averages generated by the cortical dipoles were grouped into $\mathbf{COV}_a$ and all COVs estimated from simulated averages generated by the thalamic dipoles were grouped into $\mathbf{COV}_b$ (similar comparisons were made between cortical and hippocampal generators, and hippocampal and thalamic generators). When the effect of number of dipoles was tested, all COVs estimated using a single dipole model to fit simulated averages generated by two dipoles were grouped into $\mathbf{COV}_a$ and all COVs estimated using a two dipole model to fit averages generated by two dipoles were grouped into $\mathbf{COV}_b$.

For the results reported in Section 4.3, if $p < 0.05$ I accepted the alternative hypothesis (i.e., there was a difference in COVs between groups). When many hypothesis tests are done, an adjustment of the significance level is suggested, in order to reduce the possibility of making a Type I error (i.e., rejecting the null hypothesis when it is true) [117]. I made no attempt to adjust the significance level in this dissertation. Because I did not adjust the significance level, and because my simulations only used noise data from two subjects, these simulations should be considered pilot work. Future simulations utilizing more noise subjects can then test whether the results reported in Section 4.3 are replicable.

4.3 Results

The dipole modeling results are presented in the tables below. Each table lists the SNR (recall that the SNR was measured at the vertex electrode, Cz), the simulated conditioning-testing ratio (CTR), the mean of the conditioning amplitude estimates ($\bar{x}_c$), the standard deviation of the conditioning amplitude estimates (SD_c), the coefficient of variation of the conditioning amplitude estimates (COV_c), and the mean, SD, and COV for the testing response amplitude and the amplitude ratio estimates ($\bar{x}_t$, SD_t, COV_t, $\bar{x}_r$, SD_r, and COV_r).

The results of the single generator data sets are shown in Tables 4.6-4.8. The results for the two generator data sets are shown in Tables 4.9-4.14. Tables 4.9-4.11 show the results when only a single dipole was fit to the two dipole data sets. Tables 4.12-4.14 show the results when two dipoles were fit to the two dipole data

Table 4.6: Data Set 1, Generator 1

EEG Noise Subject 1										
snr	ctr	$\bar{x}_c$	SD_c	COV_c	$\bar{x}_t$	SD_t	COV_t	$\bar{x}_r$	SD_r	COV_r
1.4	0.25	24.13	2.62	**9.19**	6.06	0.72	**8.45**	0.25	0.02	**14.14**
	1.00	27.05	6.05	**4.47**	27.18	6.41	**4.24**	1.00	0.03	**32.00**
7.1	0.25	26.03	16.33	**1.59**	6.49	3.95	**1.64**	0.25	0.01	**33.45**
	1.00	25.05	6.47	**3.87**	25.03	6.48	**3.86**	1.00	0.01	**90.72**
EEG Noise Subject 2										
snr	ctr	$\bar{x}_c$	SD_c	COV_c	$\bar{x}_t$	SD_t	COV_t	$\bar{x}_r$	SD_r	COV_r
1.4	0.45	24.86	1.87	**13.28**	24.86	0.88	**12.58**	0.44	0.02	**29.22**
	0.85	25.30	2.46	**10.31**	21.56	2.32	**9.28**	0.85	0.03	**33.13**
7.1	0.45	24.10	1.13	**21.26**	10.85	0.59	**18.44**	0.45	0.01	**44.60**
	0.85	23.98	1.19	**20.19**	20.43	1.04	**19.73**	0.85	0.01	**95.94**

sets. For the two dipole data sets, the results are shown for the first dipole, which corresponds to the fitted dipole which was in the left hemisphere, and the second dipole, which corresponds to the dipole fitted to the right hemisphere.

An examination of the results reveals several trends. As expected, there was no significant difference between the ratio COVs (COV_r) estimated using the first and second noise subject's data ($p = 0.581$). This shows that the results are not an anomaly of a single subject's noise, but are a replicable phenomenon.

The ratio COV (COV_r) was significantly greater than either the conditioning COV (COV_c) or the testing COV (COV_t) ($p < 0.001$ and $p < 0.001$, respectively). As the tables show, in nearly all cases the COV of the ratio was more than twice the COV of the conditioning or testing amplitudes. The only exceptions to this rule were Data Set 4 (bilateral thalamic dipoles) modeled by two dipoles (especially the low SNR simulations), and the low SNR, normal suppression runs for Data Set 6 (bilateral auditory cortex dipoles) modeled by two dipoles.

For Data Sets 4-6 (data sets generated by two dipoles), the COV_r estimated using a single dipole model were significantly greater than the COV_r estimated using a two dipole model ($p < 0.001$). This shows that when two generators were modeled by a single dipole (see Tables 4.9-4.11), the ratios were estimated accurately and

Table 4.7: Data Set 2, Generator 3

EEG Noise Subject 1										
snr	ctr	$\bar{x}_c$	SD_c	COV_c	$\bar{x}_t$	SD_t	COV_t	$\bar{x}_r$	SD_r	COV_r
1.4	0.25	58.18	57.14	**1.02**	15.22	18.89	**0.81**	0.25	0.03	**9.55**
	1.00	43.98	6.65	**6.62**	43.83	7.04	**6.22**	1.00	0.03	**39.78**
7.1	0.25	59.55	51.27	**1.16**	14.68	12.02	**1.22**	0.25	0.01	**32.00**
	1.00	54.77	29.82	**1.84**	55.13	30.57	**1.80**	1.00	0.01	**77.83**
EEG Noise Subject 2										
snr	ctr	$\bar{x}_c$	SD_c	COV_c	$\bar{x}_t$	SD_t	COV_t	$\bar{x}_r$	SD_r	COV_r
1.4	0.45	46.16	5.34	**8.64**	20.61	2.69	**7.65**	0.45	0.02	**18.75**
	0.85	44.59	4.56	**9.78**	38.07	3.93	**9.69**	0.85	0.02	**47.74**
7.1	0.45	44.55	1.97	**22.66**	19.95	0.92	**22.11**	0.45	0.01	**48.09**
	0.85	44.46	1.85	**24.05**	37.91	1.74	**21.81**	0.85	0.01	**97.47**

Table 4.8: Data Set 3, Generator 5

EEG Noise Subject 1										
snr	ctr	$\bar{x}_c$	SD_c	COV_c	$\bar{x}_t$	SD_t	COV_t	$\bar{x}_r$	SD_r	COV_r
1.4	0.25	43.35	12.13	**3.57**	10.78	2.80	**3.85**	0.25	0.02	**15.53**
	1.00	42.09	6.33	**6.65**	42.13	6.11	**6.90**	1.00	0.03	**38.49**
7.1	0.25	44.24	10.18	**4.35**	11.22	2.88	**3.90**	0.25	0.01	**26.39**
	1.00	43.00	5.91	**7.28**	43.09	5.94	**7.25**	1.00	0.01	**122.68**
EEG Noise Subject 2										
snr	ctr	$\bar{x}_c$	SD_c	COV_c	$\bar{x}_t$	SD_t	COV_t	$\bar{x}_r$	SD_r	COV_r
1.4	0.45	41.77	4.28	**9.77**	19.00	2.04	**9.29**	0.46	0.03	**16.55**
	0.85	40.65	4.93	**8.25**	34.60	3.98	**8.69**	0.85	0.02	**36.84**
7.1	0.45	42.52	2.64	**16.09**	19.12	1.24	**15.44**	0.45	0.01	**46.91**
	0.85	42.86	2.46	**17.40**	36.40	2.11	**17.26**	0.85	0.01	**83.59**

Table 4.9: Data Set 4, Generators 1 and 2 modeled by a single dipole

EEG Noise Subject 1										
snr	ctr	$\bar{x}_c$	SD_c	COV_c	$\bar{x}_t$	SD_t	COV_t	$\bar{x}_r$	SD_r	COV_r
1.4	0.25	24.45	2.97	**8.23**	6.19	0.98	**6.31**	0.25	0.02	**13.70**
	1.00	24.88	2.06	**12.07**	24.77	1.99	**12.42**	1.00	0.02	**41.59**
7.1	0.25	22.82	7.82	**2.92**	5.65	1.95	**2.90**	0.25	0.01	**30.56**
	1.00	24.66	0.97	**25.31**	24.59	0.94	**26.07**	1.00	0.01	**100.91**
EEG Noise Subject 2										
snr	ctr	$\bar{x}_c$	SD_c	COV_c	$\bar{x}_t$	SD_t	COV_t	$\bar{x}_r$	SD_r	COV_r
1.4	0.45	25.78	4.51	**5.72**	11.63	2.04	**5.70**	0.45	0.02	**23.57**
	0.85	26.22	4.26	**6.15**	22.08	3.58	**6.16**	0.84	0.03	**29.11**
7.1	0.45	24.66	1.49	**16.59**	11.11	0.54	**20.58**	0.45	0.01	**32.56**
	0.85	24.87	1.24	**20.13**	21.08	0.99	**21.29**	0.85	0.01	**57.85**

Table 4.10: Data Set 5, Generators 3 and 4 modeled by a single dipole

EEG Noise Subject 1										
snr	ctr	$\bar{x}_c$	SD_c	COV_c	$\bar{x}_t$	SD_t	COV_t	$\bar{x}_r$	SD_r	COV_r
1.4	0.25	73.18	15.62	**4.69**	18.44	4.28	**4.31**	0.25	0.01	**18.81**
	1.00	76.20	11.70	**6.51**	76.34	11.47	**6.66**	1.00	0.02	**45.70**
7.1	0.25	75.92	6.36	**11.93**	18.96	1.79	**10.58**	1.00	0.02	**41.59**
	1.00	74.04	4.67	**15.86**	73.85	4.53	**16.30**	1.00	0.01	**108.89**
EEG Noise Subject 2										
snr	ctr	$\bar{x}_c$	SD_c	COV_c	$\bar{x}_t$	SD_t	COV_t	$\bar{x}_r$	SD_r	COV_r
1.4	0.45	82.70	16.16	**5.12**	37.21	7.38	**5.04**	0.45	0.02	**24.71**
	0.85	78.43	14.80	**5.30**	66.43	12.13	**5.47**	0.85	0.03	**31.78**
7.1	0.45	73.41	6.41	**11.45**	32.61	2.70	**12.07**	0.44	0.01	**41.36**
	0.85	73.32	7.39	**9.92**	62.18	6.19	**10.05**	0.85	0.01	**68.49**

Table 4.11: Data Set 6, Generators 5 and 6 modeled by a single dipole

EEG Noise Subject 1										
snr	ctr	$\bar{x}_c$	SD_c	COV_c	$\bar{x}_t$	SD_t	COV_t	$\bar{x}_r$	SD_r	COV_r
1.4	0.25	182.59	23.43	**7.79**	45.66	7.18	**6.36**	0.25	0.02	**11.43**
	1.00	174.63	29.20	**5.98**	175.12	29.17	**6.00**	1.00	0.02	**50.94**
7.1	0.25	186.54	26.33	**7.09**	45.60	6.65	**6.86**	0.24	0.01	**33.32**
	1.00	190.31	13.06	**14.58**	189.78	13.19	**14.38**	1.00	0.01	**102.08**
EEG Noise Subject 2										
snr	ctr	$\bar{x}_c$	SD_c	COV_c	$\bar{x}_t$	SD_t	COV_t	$\bar{x}_r$	SD_r	COV_r
1.4	0.45	176.27	21.22	**8.31**	81.22	11.04	**7.36**	0.46	0.03	**18.39**
	0.85	183.30	19.58	**9.36**	159.07	19.57	**8.13**	0.87	0.03	**29.98**
7.1	0.45	192.43	7.73	**24.91**	86.73	3.49	**24.85**	0.45	0.01	**46.48**
	0.85	190.10	11.05	**17.20**	161.30	9.84	**16.39**	0.85	0.01	**82.29**

reliably, with high ratio COVs for all cases. In summary, when the true generators are suspected to be very close (such as bilateral thalamic generators), the data are noisy, and the dipole model is misspecified, better ratio estimates are obtained when a single dipole is modeled (compare Table 4.9 to Table 4.12).

The COVs (COV_r, COV_c, and COV_t) estimated at high SNR (recall that the SNR was computed at the vertex electrode, Cz) are significantly greater than the COVs estimated at low SNR ($p < 0.001$, $p < 0.001$, and $p < 0.001$, respectively). These results are not surprising. As the noise decreases the fits are less affected and the parameter estimates are more stable.

The COVs (COV_r, COV_c, and COV_t) estimated from the conditioning and testing responses for the "schizophrenic-like" P50 suppression (i.e., C-T ratios of 0.85 and 1.00) were significantly greater than the COVs estimated from the normal suppression (i.e., C-T ratios of 0.25 and 0.45) simulated data sets ($p < 0.001$, $p = 0.031$, and $p = 0.014$, respectively). In retrospect, this is not surprising. Since the conditioning and testing responses in the "schizophrenic-like" data sets are both large compared to the added EEG noise, these data sets have a larger effective SNR. The increased SNR, as discussed above, leads to increased COVs.

The ratio COVs (COV_r) estimated from data generated at eccentric dipole

Table 4.12: Data Set 4, Generators 1 and 2 modeled by two dipoles

EEG Noise Subject 1, Left Hemisphere Dipole										
snr	ctr	$\bar{x}_c$	SD_c	COV_c	$\bar{x}_t$	SD_t	COV_t	$\bar{x}_r$	SD_r	COV_r
1.4	0.25	13.78	3.11	**4.44**	3.00	1.78	**1.69**	0.23	0.14	**1.61**
	1.00	13.61	2.67	**5.10**	14.08	2.81	**5.02**	1.07	0.28	**3.84**
7.1	0.25	13.87	2.66	**5.22**	3.08	0.82	**3.79**	0.23	0.06	**3.64**
	1.00	12.23	0.61	**20.04**	11.98	0.76	**15.79**	0.98	0.07	**14.58**
EEG Noise Subject 2, Left Hemisphere Dipole										
snr	ctr	$\bar{x}_c$	SD_c	COV_c	$\bar{x}_t$	SD_t	COV_t	$\bar{x}_r$	SD_r	COV_r
1.4	0.45	12.89	3.18	**4.05**	7.02	2.97	**2.37**	0.58	0.31	**1.88**
	0.85	12.04	2.44	**4.94**	10.97	3.27	**3.35**	0.93	0.28	**3.36**
7.1	0.45	12.95	1.99	**6.49**	5.97	1.58	**3.79**	0.46	0.10	**4.69**
	0.85	13.05	2.40	**5.45**	11.16	3.87	**2.88**	0.82	0.24	**3.48**
EEG Noise Subject 1, Right Hemisphere Dipole										
snr	ctr	$\bar{x}_c$	SD_c	COV_c	$\bar{x}_t$	SD_t	COV_t	$\bar{x}_r$	SD_r	COV_r
1.4	0.25	9.26	1.84	**5.03**	2.72	1.32	**2.06**	0.31	0.14	**2.11**
	1.00	9.69	1.98	**4.90**	9.37	2.24	**4.18**	0.98	0.18	**5.30**
7.1	0.25	9.63	3.07	**3.14**	2.64	0.63	**4.18**	0.44	0.78	**0.55**
	1.00	10.33	0.84	**12.23**	10.51	1.03	**10.18**	1.02	0.08	**13.28**
EEG Noise Subject 2, Right Hemisphere Dipole										
snr	ctr	$\bar{x}_c$	SD_c	COV_c	$\bar{x}_t$	SD_t	COV_t	$\bar{x}_r$	SD_r	COV_r
1.4	0.45	13.16	14.08	**0.93**	4.71	4.63	**1.02**	0.40	0.22	**1.83**
	0.85	11.76	2.82	**4.17**	9.23	3.82	**2.42**	0.83	0.36	**2.27**
7.1	0.45	10.12	1.92	**5.27**	4.43	1.55	**2.87**	0.44	0.13	**3.39**
	0.85	10.03	2.63	**3.82**	8.63	4.19	**2.06**	0.83	0.23	**3.67**

Table 4.13: Data Set 5, Generators 3 and 4 modeled by two dipoles

EEG Noise Subject 1, Left Hemisphere Dipole										
snr	ctr	$\bar{x}_c$	SD_c	COV_c	$\bar{x}_t$	SD_t	COV_t	$\bar{x}_r$	SD_r	COV_r
1.4	0.25	24.77	17.54	**1.41**	6.27	4.19	**1.50**	0.26	0.06	**4.60**
	1.00	21.84	2.42	**9.01**	22.17	3.79	**5.85**	1.01	0.10	**10.32**
7.1	0.25	22.81	1.79	**12.76**	5.73	0.47	**12.28**	0.25	0.01	**24.94**
	1.00	22.58	1.08	**20.89**	22.48	1.01	**22.15**	1.00	0.01	**90.69**
EEG Noise Subject 2, Left Hemisphere Dipole										
snr	ctr	$\bar{x}_c$	SD_c	COV_c	$\bar{x}_t$	SD_t	COV_t	$\bar{x}_r$	SD_r	COV_r
1.4	0.45	33.62	24.41	**1.38**	12.90	4.09	**3.15**	0.44	0.09	**4.69**
	0.85	25.97	16.57	**1.57**	20.54	9.66	**2.13**	-0.53	5.93	**-0.09**
7.1	0.45	24.17	4.11	**5.88**	10.77	1.78	**6.04**	0.45	0.01	**43.08**
	0.85	23.37	2.28	**10.27**	19.81	1.86	**10.65**	0.85	0.01	**70.14**
EEG Noise Subject 1, Right Hemisphere Dipole										
snr	ctr	$\bar{x}_c$	SD_c	COV_c	$\bar{x}_t$	SD_t	COV_t	$\bar{x}_r$	SD_r	COV_r
1.4	0.25	19.54	18.76	**1.04**	4.84	4.51	**1.04**	0.25	0.06	**3.98**
	1.00	17.37	3.16	**5.50**	17.32	2.99	**5.80**	1.00	0.07	**14.00**
7.1	0.25	20.10	2.33	**8.61**	4.98	0.64	**7.79**	0.25	0.01	**21.87**
	1.00	20.19	1.31	**15.46**	20.19	1.22	**16.51**	1.00	0.01	**97.95**
EEG Noise Subject 2, Right Hemisphere Dipole										
snr	ctr	$\bar{x}_c$	SD_c	COV_c	$\bar{x}_t$	SD_t	COV_t	$\bar{x}_r$	SD_r	COV_r
1.4	0.45	21.41	13.71	**1.56**	12.70	10.30	**1.23**	0.26	0.89	**0.29**
	0.85	23.02	17.57	**1.31**	18.74	11.66	**1.61**	2.65	8.21	**0.32**
7.1	0.45	22.76	4.60	**4.95**	10.08	2.07	**4.87**	0.44	0.02	**28.38**
	0.85	22.06	2.64	**8.36**	18.71	2.28	**8.22**	0.85	0.01	**65.52**

Table 4.14: Data Set 6, Generators 5 and 6 modeled by two dipoles

EEG Noise Subject 1, Left Hemisphere Dipole										
snr	ctr	$\bar{x}_c$	SD_c	COV_c	$\bar{x}_t$	SD_t	COV_t	$\bar{x}_r$	SD_r	COV_r
1.4	0.25	21.56	2.45	**8.78**	5.58	0.99	**5.62**	0.26	0.04	**7.15**
	1.00	20.85	2.56	**8.13**	20.88	2.49	**8.37**	1.00	0.03	**31.98**
7.1	0.25	21.04	1.75	**12.06**	5.18	0.51	**10.19**	0.25	0.01	**16.60**
	1.00	21.47	1.29	**16.70**	21.42	1.18	**18.17**	1.00	0.02	**61.34**
EEG Noise Subject 2, Left Hemisphere Dipole										
snr	ctr	$\bar{x}_c$	SD_c	COV_c	$\bar{x}_t$	SD_t	COV_t	$\bar{x}_r$	SD_r	COV_r
1.4	0.45	20.53	2.34	**8.77**	9.29	0.86	**10.86**	0.45	0.03	**13.68**
	0.85	21.33	3.05	**6.99**	18.47	2.31	**7.98**	0.87	0.04	**20.88**
7.1	0.45	20.87	1.90	**10.97**	9.42	0.75	**12.60**	0.45	0.02	**22.70**
	0.85	20.98	1.59	**13.19**	17.83	1.23	**14.51**	0.85	0.02	**39.42**
EEG Noise Subject 1, Right Hemisphere Dipole										
snr	ctr	$\bar{x}_c$	SD_c	COV_c	$\bar{x}_t$	SD_t	COV_t	$\bar{x}_r$	SD_r	COV_r
1.4	0.25	18.74	2.27	**8.26**	4.51	0.80	**5.67**	0.24	0.03	**7.71**
	1.00	18.99	1.78	**10.64**	19.05	1.80	**10.59**	1.00	0.03	**38.25**
7.1	0.25	20.16	1.53	**13.20**	4.89	0.48	**10.12**	0.24	0.02	**14.90**
	1.00	19.98	1.38	**14.43**	19.92	1.45	**13.72**	1.00	0.02	**51.53**
EEG Noise Subject 2, Right Hemisphere Dipole										
snr	ctr	$\bar{x}_c$	SD_c	COV_c	$\bar{x}_t$	SD_t	COV_t	$\bar{x}_r$	SD_r	COV_r
1.4	0.45	19.93	2.73	**7.30**	1.68	5.52	**0.47**	0.47	0.05	**9.20**
	0.85	20.51	2.79	**7.35**	17.72	2.75	**6.44**	0.86	0.05	**18.15**
7.1	0.45	19.83	1.51	**13.15**	8.94	9.68	**13.24**	0.45	0.02	**21.46**
	0.85	19.23	1.22	**15.79**	16.29	0.92	**17.65**	0.85	0.02	**46.62**

locations were greater than the COV_r estimated from data generated at centric dipole locations. The COV_r estimated from data generated by the auditory cortical dipoles (Data Sets 3 and 6) were greater than the COV_r estimated from data generated by the thalamic dipoles (Data Sets 1 and 4) ($p = 0.039$). The COV_r estimated from data generated by the hippocampal dipoles (Data Sets 2 and 5) were greater than the COV_r estimated from the thalamic data ($p = 0.035$). There was no significant difference between the COV_r estimated from data generated by the cortical and hippocampal dipoles ($p = 0.544$). These results may be occurring for two reasons, described below.

Firstly, at eccentric dipole locations, the spherical head model is not a bad approximation to the true head [12]. Therefore, when Data Sets 2, 3, 5, and 6 are fit, the spherical model is less misspecified than when Data Sets 1 and 4 are fit using a spherical model. This may mean that the less misspecified model (because the data were generated with eccentric dipoles) has more stable amplitude estimates. Hypothesis testing of the conditioning and testing amplitude COVs, however, reveals that the eccentricity of the generators cannot fully explain the ratio COV results. The amplitude COVs (COV_c and COV_t) estimated from data generated by the auditory cortical dipoles (Data Sets 3 and 6) were greater than the COV_c and COV_t estimated from the thalamic dipoles (Data Sets 1 and 4, $p = 0.075$ and $p = 0.051$, respectively), although significance was not reached. The amplitude COVs (COV_c and COV_t) estimated from data generated by the hippocampal dipoles (Data Sets 2 and 5) were not greater than the COV_c and COV_t estimated from the thalamic data ($p = 0.668$ and $p = 0.465$, respectively). The amplitude COVs (COV_c and COV_t) estimated from data generated by the auditory cortical dipoles were greater than the COV_c and COV_t estimated from the hippocampal dipoles ($p = 0.027$ and $p = 0.056$).

The amplitude COV results complicate the interpretation of the ratio COV results, when eccentricity is varied. It appears that the decrease in model misspecification associated with eccentricity cannot fully account for the results. A second idea is that these results were obtained because eccentric dipoles are associated with increased SNR. Although all Data Sets were constructed to have the desired SNR and amplitude (4 μV) at the vertex (Cz) electrode, the amplitudes and SNR at the remaining electrodes varied for each generator configuration. Figures 4.2 and 4.3 show

that although all Data Sets were similar at the vertex electrode, they differed greatly at the lateral electrodes. Note that the cortically generated potentials had very large amplitude at the lateral electrodes in comparison to the thalamic and hippocampal potentials. The larger amplitude and resulting higher SNR at the lateral electrodes may contribute to the higher *COV*s for the averages generated by eccentric dipoles. Further research is necessary in order to determine the separate effects of decreasing model misspecification and increasing SNR on the amplitude and amplitude ratio estimates.

An unexpected finding was that the *COV*s for the conditioning and testing amplitudes for the two dipole data sets when two dipoles were fit are of the same magnitude as the *COV*s for the ratios (see Tables 4.12-4.14). The ratios are also slightly more biased than for the single dipole fits. There may be two reasons why this occurs. Firstly, it may be that when two dipoles are modeled the ratios cannot be reliably estimated for each dipole due to noise, model misspecification, or both. Secondly, it may be that the penalty functions used to enforce the bilateral constraint for two dipoles resulted in less variability in the estimated dipole parameters (location, orientation, and waveshape), in turn resulting in less variability in the estimated conditioning and testing amplitude parameters, and derived C-T ratio.

4.4 Discussion

The results of these simulations show that amplitude parameters estimated using dipole modeling are more variable than derived amplitude ratios in the face of certain types of model misspecification and EEG noise. These simulations also show that the derived amplitude ratios are accurately and reliably estimated. The fact that the amplitude parameter estimates became less variable as (1) the SNR was increased, (2) the C-T ratio was increased (i.e., increasing the effective SNR), and (3) the generators became more eccentric (i.e., less head model misspecification and/or increased SNR) suggests that the presence of model misspecification and noise lead to unreliable dipole modeling amplitude estimates.

These results imply that: (1) The P50 C-T *ratio* reliability results of Chap-

ter 2 will not be improved by improvements to the head model, although the absolute amplitude reliabilities *may* be improved, and (2) The P50 C-T ratio reliability may be improved by increasing the SNR of the original data (e.g., by monitoring subject arousal to eliminate drowsy responses, by eye-movement correcting the data, etc.). The proofs of Chapter 3 and these simulation results *only* apply to three special cases, however; when a single dipole is active, when dipoles are active with the same amplitude, or when multiple dipoles all have the same amplitude ratio. This thesis does not address the extent to which improvements to the head model will be necessary to address most multiple dipole modeling questions.

The results from data sets generated by two dipoles and fitted using two dipoles were particularly interesting. In these cases, the amplitude ratios were *more* variable than the absolute amplitudes when estimated from the low SNR data. For Data Set 4 (bilateral thalamic dipoles), the same was also true for the high SNR data. The generators of Data Set 4 were very closely spaced and centric, and the misspecified, noisy model simply did not perform well. Although the two dipole model performed better on Data Sets 5 and 6 (hippocampal and auditory cortex dipoles) than on Data Set 1, the single dipole model had higher COVs for all three of these data sets. In summary, in a misspecified model there is no advantage to using multiple dipoles if the ratio is the measurement of interest, and if the problem is one of the special cases noted above.

Data Sets 4-6 were generated by synchronously active bilateral dipoles. The proofs in Chapter 3 did not require synchrony of the multiple dipoles for unbiased ratio estimation. Although I did not simulate averages generated by multiple asynchronous dipoles (with the same amplitude parameters and/or amplitude ratio), the results of dipole modeling should be similar to the results from Data Sets 4-6. I would expect that when the dipoles had the same amplitude parameters (as described in Chapter 3, Section 3.2.3), fitting with a single dipole would result in higher ratio COVs than would fitting with two dipoles (same results as in Tables 4.9-4.11 as compared to Tables 4.12-4.14). I would further expect that when the dipoles had different amplitude parameters but the same amplitude ratios (as described in Chapter 3, Section 3.2.4), fitting with the correct number of dipoles would result in amplitude and

ratio *COV*s of about the same magnitude (same results as in Tables 4.12-4.14).

As noted in Section 4.2, the number of single trials in my noise data sets was small. As previously discussed, however, simulated averages generated from the noise data sets should still be independent of each other. The likely effect of these small noise data sets is to reduce the variability in the estimated dipole parameters (location, orientation, decaying sinusoid, and amplitudes). In other words, a larger noise data set would have generated simulated averages that were more variable across replications, leading to more variable estimated parameters. This means that the small conditioning and testing *COV*s were obtained *despite* using a small noise data set, and the use of a larger noise data set would have resulted in *even smaller COV*s.

There are two hypotheses as to why the amplitude ratios are less variable than the absolute amplitudes. One hypothesis was discussed at the end of Chapter 3. The interdependence of some of the random variables in a noisy dipole modeling ratio measurement (i.e., the numerator and denominator of the ratio are not independent of each other) may lead to a ratio with less variance than either the numerator or the denominator. The other hypothesis is that the global minimum in a misspecified dipole model is shallow (i.e., the global minimum is not "surrounded" by high, steep walls in the parameter surface) or surrounded by a "rough" surface (i.e., the parameter estimation surface is bumpy and many local minima are present), and the presence of noise on the data is likely to "shift" the global minimum. When the global minimum shifts, so do the estimated parameters (assuming that the nonlinear optimization routine finds the global minimum). As shown in Chapter 3, however, for special cases the amplitude ratio is correctly estimated *for any dipole location, orientation, and time-varying magnitude function.* Therefore (for the special cases studied), a shift in the global minimum will *not* affect the derived ratio, but only the estimated amplitudes.

Figures 4.6-4.8 show that the dipole parameter estimates varied due to the noise added to the simulated data. These figures show the parameter error norms over the 20 replications for each generator or generator pair, C-T ratio, and SNR. The parameters error norms were computed by taking the normalized difference between noisy and noise-free fits and computing the norm. Since I used simulated annealing to

estimate the dipole parameters, the variation in dipole fits was probably not because the nonlinear optimization algorithm converged to various local minima, but because the noise "shifted" the global minimum.

The error norms were computed as follows. Let $\mathbf{x}$ be the parameter vector (dipole location, orientation, decaying sinusoid parameters λ, τ, and β) fit with a misspecified model on noise-free data. Let $\mathbf{x}'$ be the parameters vector fit with a misspecified model on noisy data. Let $\boldsymbol{\Delta}$ be the normalized difference vector, where $\Delta_i = (x_i - x_i')/x_i$. The error norms plotted in the figures are $\| \boldsymbol{\Delta} \|_2 / k$ where k is the number of parameters (8 for single dipole problems, 16 for two dipole problems). The error norm is then 0.0 when the noisy and noise-free fits are the same, and increases as they differ. On the plots, each circle represents the error norm for one of the dipole fits. The x axis is labeled by which EEG Noise Subject was used to create the simulated data (Noise Subject 1 or Noise Subject 2) and by what C-T ratio and SNR were simulated (nl=normal suppression, low SNR; nh=normal suppression, high SNR; sl=schizophrenic suppression, low SNR; sh=schizophrenic suppression, high SNR).

The variation in parameters shown in the figures corresponds very well with the *COV*s observed for the amplitudes. In general, the parameters were less variable at high SNR as compared to low SNR, were less variable for schizophrenic vs. normal suppression, and were less variable for eccentric vs. centric dipoles.

The parameter error norms show that noise in a misspecified model leads to variable dipole location, orientation, and time-varying moment function estimates, which lead in turn to variable amplitude estimates. Although I cannot rule out the possibility that the C-T ratios were less variable because of the interdependence of the conditioning and testing amplitude parameters, the parameter error norms support the hypothesis that the amplitude parameter estimates are more variable because the presence of EEG noise shifts the global minimum of a misspecified dipole model. Additional research is needed to evaluate the separate effects of interdependence and EEG noise.

This chapter has demonstrated that dipole modeling can be used to reliably and accurately estimate amplitude ratios for a certain set of problems. Unfortunately, as a rule, ratios are not used clinically or in a research setting (notable exceptions to

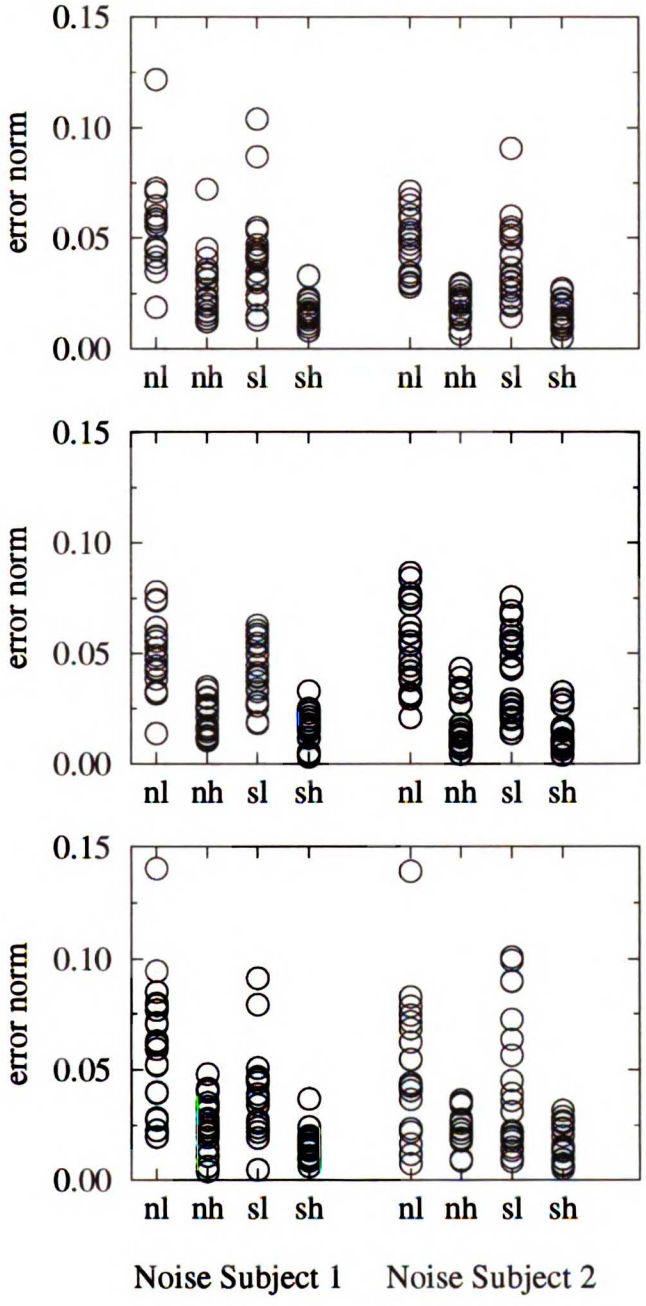

Figure 4.6: Parameter error norms for Data Sets 1-3
The error norms for Data Set 1 are shown in the top plot, the error norms for Data Set 2 are shown in the middle plot, and the error norms for Data Set 3 are shown in the bottom plot. The error norm is 0 when the noise free and noisy fits are the same. The key is n=normal suppression, s=schizophrenic suppression, h=high SNR, l=low SNR.

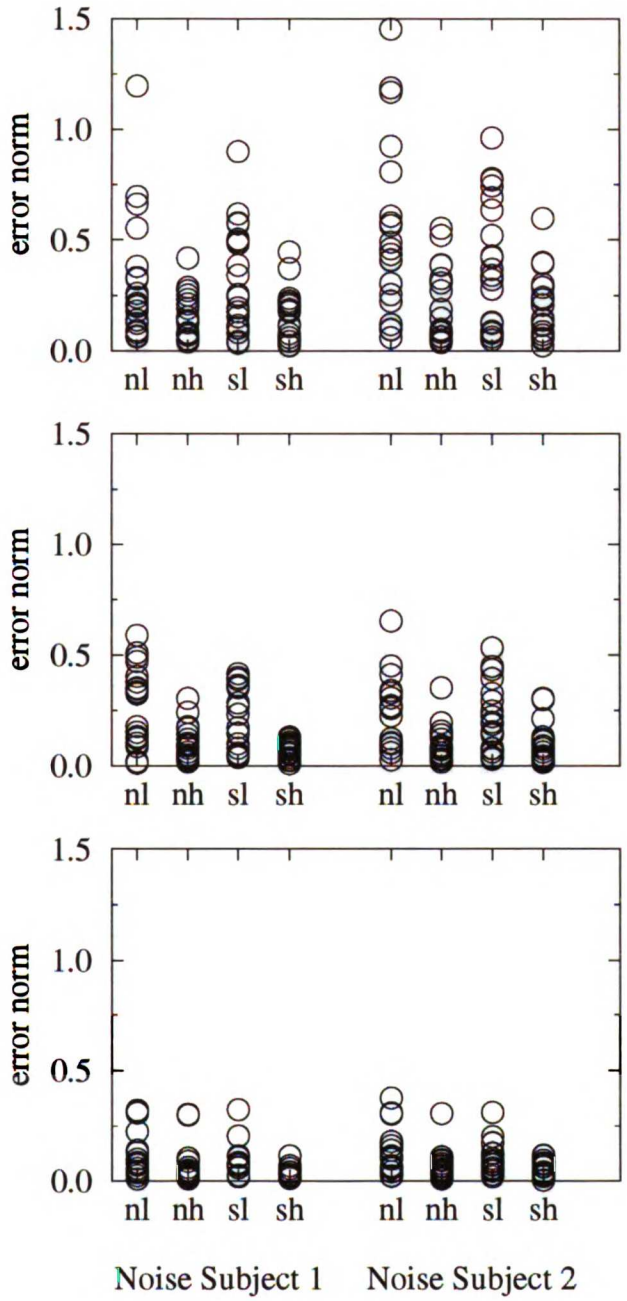

Figure 4.7: Parameter error norms for Data Sets 4-6, modeled by one dipole
The error norms for Data Set 4 are shown in the top plot, the error norms for Data Set 5 are shown in the middle plot, and the error norms for Data Set 6 are shown in the bottom plot. The error norm is 0 when the noise free and noisy fits are the same. The key is n=normal suppression, s=schizophrenic suppression, h=high SNR, l=low SNR. The error norm for one replication for Data Set 4, Noise Subject 1, nh, is plotted off the chart (error norm=35).

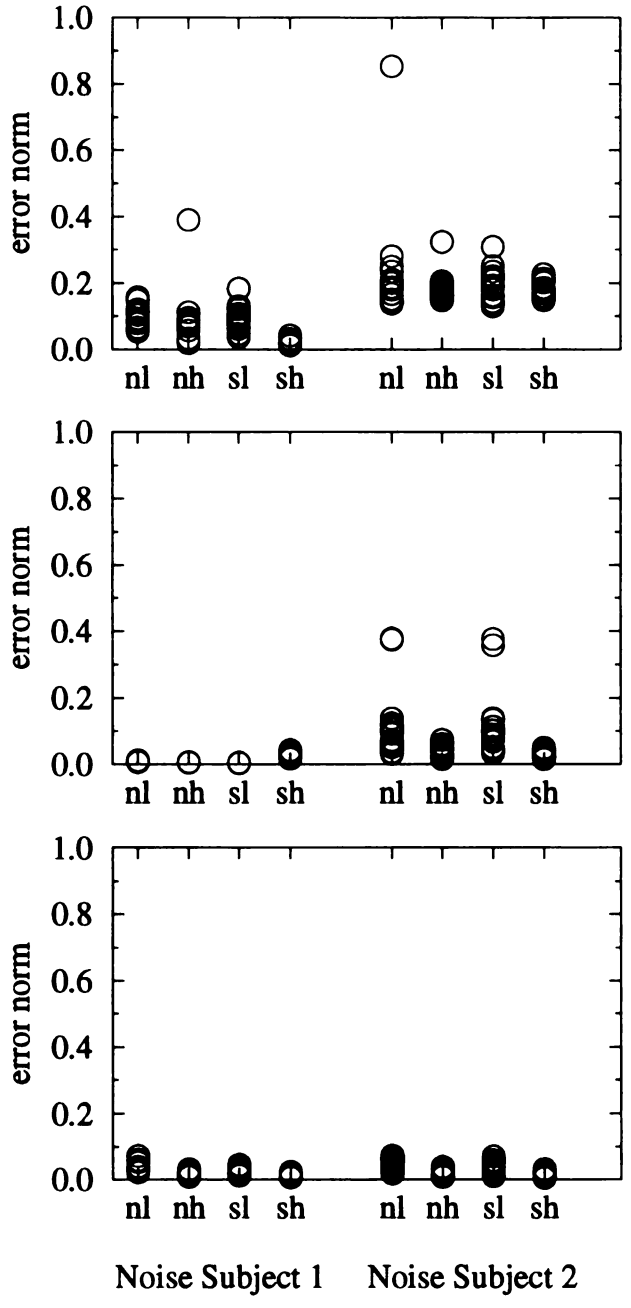

Figure 4.8: Parameter error norms for Data Sets 4-6, modeled by two dipoles The error norms for Data Set 4 are shown in the top plot, the error norms for Data Set 5 are shown in the middle plot, and the error norms for Data Set 6 are shown in the bottom plot. The error norm is 0 when the noise free and noisy fits are the same. The key is n=normal suppression, s=schizophrenic suppression, h=high SNR, l=low SNR.

this rule are the auditory P50 C-T ratio and the auditory brainstem response amplitude ratio of waves V-I). Reliable amplitude parameter estimates, however, would benefit both clinicians and researchers investigating a wide variety of EPs. To this end, I will discuss some possible ways to decrease the variability of amplitude parameter estimates.

The *COV* comparisons (between SNRs, C-T ratios, and generator eccentricity) clearly showed that the amplitude parameter estimates became less variable as the SNR was increased (recall that higher C-T ratios and eccentric generators also increased the effective SNR of the simulated averages). Though obvious, it is important to remember that no analysis method can substitute for a good signal to noise ratio.

The variation in the parameter error norms (see Figures 4.6-4.8) support the hypothesis that the global minimum in the misspecified dipole model is shallow or surrounded by a rough surface, such that the presence of noise "shifts" the global minimum. If this is the case, there are two ways in which more stable amplitude estimates could be achieved. The first is to improve the model and remove the misspecification. This approach would hopefully lead to a "steeper" global minimum which would be less affected by noise. This approach is very complicated and computationally intensive. The second approach is to eliminate the model, and this approach is motivated by the following idea. If the global minimum of the posed mathematical problem is "shifting" because of the presence of noise, *and* the nonlinear optimization algorithm finds the "shifted" global minimum (a likely occurrence, using simulated annealing), then the solution contains errors. In this chapter, the global minimum contains dipole location, orientation, and waveshape information, which is then used to compute the amplitude parameters (i.e., errors in the global minimum lead to errors in the amplitude parameters, but not to errors in the amplitude ratios, as discussed in Chapter 3). If the noisy, error-prone global minimum is the problem, then perhaps it should not be located, and the amplitude parameters should be estimated using some other method. In this chapter, eliminating the search for the global minimum means eliminating the estimation of the dipole location, orientation, and parametric waveshape–in other words, eliminating the model. The variable parameter error norms are evidence that

the global minimum is indeed shifting with the noise, so a multi-channel, model free amplitude estimation method should be considered.

The parameter error norms shed light on another observation. The *COV*s of the amplitudes in the two dipole problems were surprisingly good as compared to the *COV*s of the ratios. This may be due to the bilateral constraint used in fitting the two dipole problems. The bilateral constraint limited the solution space, and probably led to less variable dipole orientation, location, and waveshape estimates, which in turn led to less variable amplitude estimates. This can be seen in Figure 4.8. The parameter error norms for the two dipole problems are not as variable as the error norms for the one dipole problems, which were essentially unconstrained (they were constrained to stay inside the sphere). This result raises the possibility that adding location, orientation, or time-varying magnitude (i.e., waveshape) constraints could stabilize amplitude estimates.

This discussion has proposed three ways of stabilizing the absolute amplitude measurements: (1) reduce the misspecification in the dipole model, (2) implement constraints in the present crude model, and (3) implement a "model free" estimation method. The first method is computationally expensive and difficult to implement. The second requires prior knowledge about location, orientation, and time-varying magnitude function, which may not be available. The third method is attractive because of its simplicity, and is addressed in Chapter 5.

Chapter 5

Using Singular Value Decomposition for Amplitude and Amplitude Ratio Estimation

The results of Chapter 3 suggest that the ratios are accurately estimated because the effect of model misspecification "cancels" for ratios. The results of Chapter 4 show that amplitude ratios are accurately and reliably estimated in the presence of model misspecification and EEG noise, but amplitude parameters are not. These results led me to question whether the dipole model was necessary for improved amplitude and amplitude ratio estimation.

In this chapter I propose a "model-free" method for estimation of the covariate effects on amplitudes. This model-free method uses multiple channels of data but does not use the dipole model. This method is not completely model free, in the sense that I enforce a constraint that all channels of data must have a common "shape" (i.e., all channels have the same time varying magnitude, scaled by some amount across channels). I also enforce the constraint that each data set must have the same topographical distribution (scaled by some amount between data sets), although this topographical distribution does not have to fit the dipole model. These constraints are appropriate for the special cases in which amplitude ratios were estimated without bias, as discussed in Chapter 3. In review, these are the case of a single dipole

active, multiple dipoles with the same amplitude, and multiple dipoles with the same amplitude ratio (estimated across data sets).

The model-free method involves twice performing singular value decomposition (SVD) [104]–first on the original data sets, and second to the information from the first decomposition. This chapter will briefly review singular value decomposition, describe the SVD method, present the results when the SVD method is applied to simulated and real data, and discuss the relationship between this SVD method and principal components analysis.

Notation: I use bold-faced letters to indicate vectors, bold-faced script letters to indicate matrices, and use normal-faced italic letters to indicate scalars.

5.1 Singular Value Decomposition

The singular value decomposition (SVD) is a matrix factorization that has been used for image processing, determining the effective rank of a matrix, polar decomposition, and least squares problems [104]. Singular value decomposition will factor an $m \times n$ rectangular matrix $\mathcal{H}$ as

$$\mathcal{H} = \mathcal{U}\mathcal{W}\mathcal{Y}^T \tag{5.1}$$

where

$$\begin{aligned} \mathcal{W} &= \begin{bmatrix} S \\ 0 \end{bmatrix} \quad m > n \\ \mathcal{W} &= \mathcal{S} \quad m = n \\ \mathcal{W} &= \begin{bmatrix} \mathcal{S} & 0 \end{bmatrix} \quad m < n \end{aligned}$$

$\mathcal{U}$ is an $m \times m$ orthogonal matrix, $\mathcal{Y}$ is an $n \times n$ orthogonal matrix, and $\mathcal{S}$ is a $min(m,n) \times min(m,n)$ matrix of diagonal elements, $sv_1, sv_2, \ldots, sv_{min(m,n)}$ ordered such that

$$sv_1 \geq sv_2 \geq \ldots \geq sv_{min(m,n)} \geq 0$$

The first $min(m,n)$ columns of $\mathcal{U}$ are the left-hand singular vectors of $\mathcal{H}$, the diagonal elements of $\mathcal{S}$ are the singular values of $\mathcal{H}$, and the first $min(m,n)$ columns of $\mathcal{Y}$ are the right hand singular vectors of $\mathcal{H}$.

5.2 The SVD Method

Let $\mathcal{H}$ be a matrix composed of two data sets over a two time windows. Let n denote the number of electrodes or data channels, and let u denote the number of time points. The matrix $\mathcal{H}$ will then be of dimension $u \times 2n$, where the first n columns consist of data from the first data set, and the remaining n columns consist of data from the second data set. The matrix $\mathcal{H}$ can be written as:

$$\mathcal{H} = \begin{bmatrix} H_{11} & \dots & H_{1n} & H_{1(n+1)} & \dots & H_{1(2n)} \\ H_{21} & \dots & H_{2n} & H_{2(n+1)} & \dots & H_{2(2n)} \\ \vdots & \ddots & \vdots & \vdots & \ddots & \vdots \\ H_{u1} & \dots & H_{un} & H_{u(n+1)} & \dots & H_{u(2n)} \end{bmatrix}$$

When SVD is applied to $\mathcal{H}$, I get three matrices, and they are (assuming that $2n < u$):

$$\mathcal{U} = \begin{bmatrix} U_{11} & U_{12} & \dots & U_{1u} \\ U_{21} & U_{22} & \dots & U_{2u} \\ \vdots & \vdots & \ddots & \vdots \\ U_{u1} & U_{u2} & \dots & U_{uu} \end{bmatrix}$$

$$\mathcal{W} = \begin{bmatrix} sv_1 & 0 & \dots & 0 \\ 0 & sv_2 & 0 & 0 \\ \vdots & 0 & \ddots & \vdots \\ 0 & 0 & \dots & sv_n \\ 0 & 0 & \dots & 0 \\ \vdots & \vdots & \vdots & \vdots \\ 0 & 0 & \dots & 0 \end{bmatrix}$$

$$\mathcal{Y}^T = \begin{bmatrix} Y_{11} & \dots & Y_{n1} & Y_{(n+1)1} & \dots & Y_{(2n)1} \\ Y_{12} & \dots & Y_{n2} & Y_{(n+1)2} & \dots & Y_{(2n)2} \\ \vdots & \ddots & \vdots & \vdots & \ddots & \vdots \\ Y_{1(2n} & \dots & Y_{n(2n)} & Y_{(n+1)(2n)} & \dots & Y_{(2n)(2n)} \end{bmatrix}$$

I can think of $\mathcal{U}$ as the map from time points to some intermediate space, and $\mathcal{Y}^T$ as the map from that intermediate space into channels. When only a single

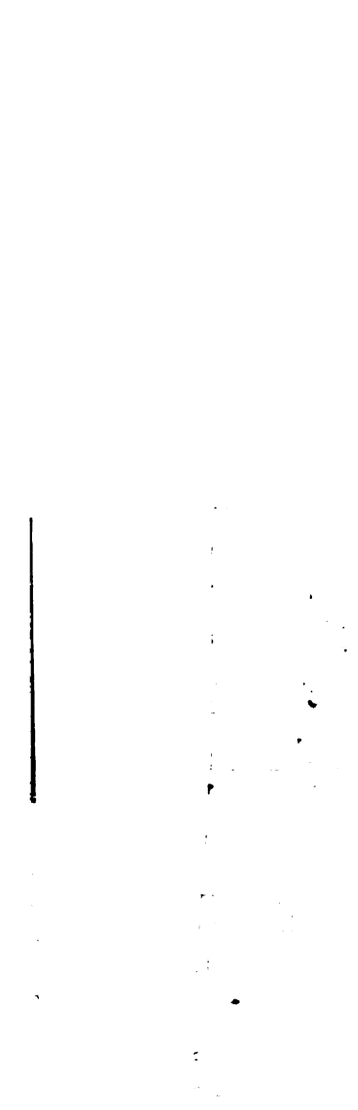

dipole is active or when two or more dipoles are simultaneously active with similar timecourses (e.g., when P50 is evoked by bilateral auditory stimulation), all electrode channels should have the same "shape" over time, and any differences in the shape across channels would be attributed to noise. In such a case, only the first singular value, sv_1, will be significantly different from 0, and I can set the remaining singular values to 0 and still achieve a very good approximation to the true data set $\mathcal{H}$. Only sv_1, the first right singular vector $\mathbf{U}_{\cdot 1}$, and the first left singular vector $\mathbf{Y}_{\cdot 1}$ contribute to the $\mathcal{H}'$ (the approximation to $\mathcal{H}$), as shown:

$$\mathcal{H}' = \begin{bmatrix} U_{11}sv_1Y_{11} & U_{11}sv_1Y_{21} & \dots & U_{11}sv_1Y_{(2n)1} \\ U_{21}sv_1Y_{11} & U_{11}sv_1Y_{21} & \dots & U_{21}sv_1Y_{(2n)1} \\ \vdots & \vdots & \ddots & \vdots \\ U_{u1}sv_1Y_{11} & U_{u1}sv_1Y_{21} & \dots & U_{u1}sv_1Y_{(2n)1} \end{bmatrix}$$

As can be seen from $\mathcal{H}'$, the first right singular vector $\mathbf{U}_{\cdot 1}$ is the common shape across all channels, and the first left singular vector $\mathbf{Y}_{\cdot 1}$ contains the electrode weightings.

Because I want to enforce a common topographical distribution, I must apply SVD a second time. To do so, I first arrange the first left singular vector $\mathbf{Y}_{\cdot 1}$ weighted by sv_1 into an $n \times 2$ matrix which I denote $\mathcal{E}$, as shown,

$$\mathcal{E} = sv_1 \begin{bmatrix} Y_{11} & Y_{(n+1)1} \\ Y_{21} & Y_{(n+2)1} \\ \vdots & \vdots \\ Y_{n1} & Y_{(2n)1} \end{bmatrix}$$

SVD is used to factor the matrix $\mathcal{E}$ into three matrices, as shown,

$$\mathcal{X}' = \begin{bmatrix} X'_{11} & X'_{12} & \dots & X'_{1n} \\ X'_{21} & X'_{22} & \dots & X'_{2n} \\ \vdots & \vdots & \ddots & \vdots \\ X'_{n1} & X'_{n2} & \dots & X'_{nn} \end{bmatrix}$$

$$\mathcal{W}' = \begin{bmatrix} sv'_1 & 0 \\ 0 & sv'_2 \end{bmatrix}$$

$$\mathcal{Y}'^{T} = \begin{bmatrix} Y'_{11} & Y'_{21} \\ Y'_{12} & Y'_{22} \end{bmatrix}$$

I can think of $\mathcal{X}'$ as the map from electrodes to some intermediate space, and $\mathcal{Y}'^{T}$ is the map from the intermediate space to data sets or replications. When a single dipole is active or two dipoles are active simultaneously with similar timecourses, only the first singular value sv'_1 will be significantly different from 0. The first right singular vector $\mathbf{X}'_{\cdot 1}$ is the "common" topographical distribution across data sets, and the first left singular vector $\mathbf{Y}'_{\cdot 1}$ contains the amplitude parameter estimates for the two data sets. The singular value sv'_1 is the common amplitude. I can write an approximation $\mathcal{E}'$ as,

$$\mathcal{E}' = \begin{bmatrix} X'_{11}sv'_1Y'_{11} & X'_{11}sv'_1Y'_{21} \\ X'_{21}sv'_1Y'_{11} & X'_{21}sv'_1Y'_{21} \\ \vdots & \vdots \\ X'_{n1}sv'_1Y'_{11} & X'_{n1}sv'_1Y'_{21} \end{bmatrix}$$

and by substituting all values, I can obtain the approximation to the original $\mathcal{H}$, as shown,

$$\mathcal{H}'' = \begin{bmatrix} U_{11}X'_{11}sv'_1Y'_{11} & \dots & U_{11}X'_{n1}sv'_1Y'_{11} & U_{11}X'_{11}sv'_1Y'_{21} & \dots & U_{11}X'_{n1}sv'_1Y'_{21} \\ U_{21}X'_{11}sv'_1Y'_{11} & \dots & U_{21}X'_{n1}sv'_1Y'_{11} & U_{21}X'_{11}sv'_1Y'_{21} & \dots & U_{21}X'_{n1}sv'_1Y'_{21} \\ \vdots & \ddots & \vdots & \vdots & \ddots & \vdots \\ U_{u1}X'_{11}sv'_1Y'_{11} & \dots & U_{u1}X'_{n1}sv'_1Y'_{11} & U_{u1}X'_{11}sv'_1Y'_{21} & \dots & U_{u1}X'_{n1}sv'_1Y'_{21} \end{bmatrix}$$

An examination of $\mathcal{H}''$ shows that $\mathbf{U}_{\cdot 1}$ is the common shape across all channels and data sets, $\mathbf{X}'_{\cdot 1}$ is the common topographical distribution across data sets, $\mathbf{Y}'_{\cdot 1}$ are the amplitude parameters which describe the covariate effects on amplitude across data sets, and sv'_1 is the common amplitude.

The advantage of the SVD method is that it is much faster and easier to use than dipole modeling because nonlinear optimization is not required. The constraints of common timecourse and common topographical distribution can also be easily enforced. The disadvantage is that it may fail for multiple dipoles overlapping in activation, and that covariate effects on latency cannot be estimated (unlike dipole

modeling, see Section 1.3.4 for details on estimation of the covariate effects on latency using dipole modeling).

In the next two sections I applied the SVD method to the simulated data from Chapter 4 and to the real auditory P50 data from Chapter 2, in order to test the following hypotheses:

1 The *COV*s of amplitude ratios estimated using the SVD method are not significantly different from the *COV*s of amplitude ratios estimated using dipole modeling.

2 The *COV*s of the estimates obtained using the SVD method will increase as the SNR and the C-T ratio increases, consistent with the dipole modeling results.

3 When the SVD method is applied to the real P50 data used in Chapter 2, an improvement in C-T ratio reliability over peak-picking will be achieved, comparable to the improvement achieved using dipole modeling.

5.3 Application to Simulated Data

The SVD method was applied to all data sets created in Chapter 4. To review, I generated data in a 3-shell skull shape model using an averaged and filtered P50 evoked potential as a template for the time-varying amplitude function. Real EEG "noise" was added to these simulated data to generate several simulated averages for each dipole configuration. I constructed data sets generated by single dipoles located in the central nuclei of the thalamus, the hippocampus, and the auditory cortex. I also constructed data sets generated by synchronously active bilateral thalamic, hippocampal, and auditory cortical dipoles. The locations and orientations used are shown in Table 4.1 and the data sets generated are shown in Table 4.4. Each simulated EP consisted of a pair of evoked potentials, corresponding to the conditioning and testing responses of the auditory P50 collected in a paired click paradigm. Two amplitude ratios were simulated for each generator or generator pair, corresponding to

normal P50 suppression (i.e., amplitude ratios between 0.25 and 0.50) and abnormal P50 suppression (i.e., amplitude ratios between 0.75 and 1.00). Real EEG noise was added to create simulated averages at high and low signal to noise ratios (SNRs). The data were generated at 30 electrode sites, as shown in Table 4.3. Twenty simulated averages for each generator or generator pair, C-T ratio, and SNR were created using a single subject's noise data. A second set of twenty replications of each generator or generator pair, C-T ratio, and SNR were created using a second subject's noise data, in order to ensure that any results were not an anomaly of the first subject's noise data.

The SVD method was applied to the conditioning and testing responses for each replication. Since 30 electrode locations were simulated, the first 30 columns of $\mathcal{H}$ corresponded to the conditioning average, and the last 30 columns of $\mathcal{H}$ corresponded to the testing average. The SVD method was then applied to $\mathcal{H}$ (i.e., SVD was used twice). For each replication, $sv_1' \cdot Y_{11}'$ was the conditioning amplitude estimate, $sv_1' \cdot Y_{21}'$ was the testing amplitude estimate, and Y_{21}'/Y_{11}' was the C-T ratio estimate.

The results of the SVD method are shown in Tables 5.1-5.6. These tables are arranged similarly to the tables in Chapter 4. Each table lists the SNR, the simulated conditioning-testing ratio (CTR), the mean of the conditioning amplitude estimate ($\bar{x}_c$), the standard deviation of the conditioning amplitude estimate (SD_c), the coefficient of variation of the conditioning amplitude estimate (COV_c), and the mean, SD, and COV for the testing response amplitude and the amplitude ratio estimates ($\bar{x}_t$, SD_t, COV_t, $\bar{x}_r$, SD_r, and COV_r).

The estimates obtained using the SVD method were compared to the estimates obtained using dipole modeling (compare Tables 4.6-4.11 to Tables 5.1-5.6). Because the SVD method cannot separate the activity of two synchronous generators, the first left singular vector is effectively the "best fit" of a single generator to the data contained in $\mathcal{H}$, even when the data were generated by two dipoles. This is similar to fitting a single dipole model to the data generated by two dipoles. Therefore, it is appropriate to compare the results of the SVD method to the results of the single dipole model. As described in Chapter 4, the randomization technique was used for hypothesis testing.

Table 5.1: Data Set 1, Generator 1 analyzed by the SVD Method

EEG Noise Subject 1										
snr	ctr	$\bar{x}_c$	SD_c	COV_c	$\bar{x}_t$	SD_t	COV_t	$\bar{x}_r$	SD_r	COV_r
1.4	0.25	53.69	0.87	**61.73**	13.47	0.90	**15.00**	0.25	0.02	**14.13**
	1.00	53.60	0.89	**60.06**	53.55	0.96	**55.70**	0.99	0.03	**38.58**
7.1	0.25	53.54	0.46	**116.71**	13.46	0.37	**35.96**	0.25	0.01	**36.19**
	1.00	53.52	0.46	**116.38**	53.48	0.29	**138.00**	1.00	0.01	**84.03**
EEG Noise Subject 2										
snr	ctr	$\bar{x}_c$	SD_c	COV_c	$\bar{x}_t$	SD_t	COV_t	$\bar{x}_r$	SD_r	COV_r
1.4	0.45	53.95	0.90	**60.22**	23.93	0.79	**30.37**	0.44	0.01	**29.80**
	0.85	53.89	0.89	**60.25**	45.87	1.02	**45.18**	0.85	0.03	**33.91**
7.1	0.45	55.55	0.48	**112.40**	24.11	0.47	**51.32**	0.45	0.01	**45.21**
	0.85	53.54	0.48	**112.15**	45.61	0.39	**116.01**	0.85	0.01	**94.76**

Table 5.2: Data Set 2, Generator 3 analyzed by the SVD Method

EEG Noise Subject 1										
snr	ctr	$\bar{x}_c$	SD_c	COV_c	$\bar{x}_t$	SD_t	COV_t	$\bar{x}_r$	SD_r	COV_r
1.4	0.25	62.28	0.94	**65.94**	15.26	1.18	**12.90**	0.25	0.02	**12.76**
	1.00	62.18	0.95	**65.54**	61.84	1.08	**57.05**	0.99	0.02	**44.47**
7.1	0.25	62.03	0.53	**116.89**	15.48	0.38	**40.22**	0.25	0.01	**42.40**
	1.00	62.02	0.53	**116.49**	62.07	0.31	**198.30**	1.00	0.01	**104.02**
EEG Noise Subject 2										
snr	ctr	$\bar{x}_c$	SD_c	COV_c	$\bar{x}_t$	SD_t	COV_t	$\bar{x}_r$	SD_r	COV_r
1.4	0.45	62.42	0.96	**64.90**	27.84	1.40	**19.93**	0.45	0.02	**19.42**
	0.85	62.36	0.97	**64.02**	53.21	0.95	**55.93**	0.85	0.02	**48.12**
7.1	0.45	61.85	0.36	**170.35**	27.70	0.52	**52.87**	0.45	0.01	**49.32**
	0.85	61.84	0.37	**168.32**	52.71	0.38	**137.13**	0.85	0.01	**101.14**

Table 5.3: Data Set 3, Generator 5 analyzed by the SVD Method

EEG Noise Subject 1										
snr	ctr	$\bar{x}_c$	SD_c	COV_c	$\bar{x}_t$	SD_t	COV_t	$\bar{x}_r$	SD_r	COV_r
1.4	0.25	90.13	1.76	**51.27**	22.60	1.32	**17.13**	0.25	0.02	**15.78**
	1.00	90.03	1.78	**50.56**	90.16	1.22	**73.78**	1.00	0.03	**39.78**
7.1	0.25	89.95	0.44	**205.46**	22.68	0.62	**36.744**	0.25	0.01	**34.69**
	1.00	89.93	0.44	**206.26**	90.10	0.55	**162.78**	1.00	0.01	**133.69**
EEG Noise Subject 2										
snr	ctr	$\bar{x}_c$	SD_c	COV_c	$\bar{x}_t$	SD_t	COV_t	$\bar{x}_r$	SD_r	COV_r
1.4	0.45	89.94	1.95	**46.15**	40.03	2.04	**20.06**	0.46	0.03	**17.33**
	0.85	89.88	1.96	**45.95**	76.57	1.58	**48.58**	0.85	0.02	**38.29**
7.1	0.45	90.18	0.78	**116.26**	40.55	0.76	**53.55**	0.45	0.01	**46.50**
	0.85	90.17	0.78	**116.08**	76.57	0.56	**136.05**	0.85	0.01	**86.30**

Table 5.4: Data Set 4, Generators 1 and 2 analyzed by the SVD Method

EEG Noise Subject 1										
snr	ctr	$\bar{x}_c$	SD_c	COV_c	$\bar{x}_t$	SD_t	COV_t	$\bar{x}_r$	SD_r	COV_r
1.4	0.25	46.97	0.92	**50.90**	11.84	0.95	**12.50**	0.25	0.02	**13.67**
	1.0	46.90	0.92	**50.93**	46.73	0.90	**51.92**	1.00	0.02	**41.17**
7.1	0.25	46.92	0.32	**145.13**	11.62	0.34	**33.92**	0.25	0.01	**30.47**
	1.00	46.90	0.32	**147.85**	46.76	0.41	**114.35**	1.00	0.01	**100.46**
EEG Noise Subject 2										
snr	ctr	$\bar{x}_c$	SD_c	COV_c	$\bar{x}_t$	SD_t	COV_t	$\bar{x}_r$	SD_r	COV_r
1.4	0.45	46.87	0.87	**53.96**	21.14	0.81	**26.03**	0.45	0.02	**23.47**
	0.85	46.80	0.88	**53.02**	39.44	1.15	**34.22**	0.84	0.03	**28.47**
7.1	0.45	46.86	0.63	**74.58**	21.14	0.45	**46.53**	0.45	0.01	**32.85**
	0.85	46.85	0.63	**74.82**	39.71	0.48	**83.15**	0.85	0.01	**59.02**

Table 5.5: Data Set 5, Generators 3 and 4 analyzed by the SVD Method

EEG Noise Subject 1										
snr	ctr	$\bar{x}_c$	SD_c	COV_c	$\bar{x}_t$	SD_t	COV_t	$\bar{x}_r$	SD_r	COV_r
1.4	0.25	58.08	1.06	**54.77**	14.58	0.81	**18.11**	0.25	0.01	**18.81**
	1.00	57.99	1.07	**54.08**	58.18	0.71	**82.00**	1.00	0.02	**47.11**
7.1	0.25	57.86	0.43	**133.74**	14.44	0.52	**27.62**	0.25	0.01	**26.80**
	1.00	57.85	0.43	**133.68**	57.71	0.33	**174.72**	1.00	0.01	**115.66**
EEG Noise Subject 2										
snr	ctr	$\bar{x}_c$	SD_c	COV_c	$\bar{x}_t$	SD_t	COV_t	$\bar{x}_r$	SD_r	COV_r
1.4	0.45	58.17	0.77	**75.93**	26.18	0.85	**30.93**	0.45	0.02	**26.30**
	0.85	58.09	0.76	**76.29**	49.28	1.20	**41.19**	0.85	0.03	**33.56**
7.1	0.45	58.03	0.56	**103.66**	25.79	0.47	**54.34**	0.44	0.01	**43.13**
	0.85	58.02	0.56	**103.83**	49.21	0.48	**102.78**	0.85	0.01	**71.07**

Table 5.6: Data Set 6, Generators 5 and 6 analyzed by the SVD Method

EEG Noise Subject 1										
snr	ctr	$\bar{x}_c$	SD_c	COV_c	$\bar{x}_t$	SD_t	COV_t	$\bar{x}_r$	SD_r	COV_r
1.4	0.25	79.00	1.18	**67.11**	19.70	1.47	**13.36**	0.25	0.02	**12.86**
	1.00	78.89	1.19	**66.13**	79.05	1.25	**63.22**	1.00	0.02	**54.96**
7.1	0.25	79.42	0.41	**195.50**	19.43	0.53	**36.49**	0.24	0.01	**37.97**
	1.00	79.40	0.40	**197.36**	79.20	0.63	**126.51**	1.00	0.01	**133.75**
EEG Noise Subject 2										
snr	ctr	$\bar{x}_c$	SD_c	COV_c	$\bar{x}_t$	SD_t	COV_t	$\bar{x}_r$	SD_r	COV_r
1.4	0.45	79.09	1.19	**66.38**	36.40	1.73	**21.03**	0.46	0.02	**20.77**
	0.85	79.00	1.20	**65.95**	68.34	2.05	**33.28**	0.87	0.03	**31.58**
7.1	0.45	79.47	0.58	**136.88**	35.91	0.61	**58.96**	0.45	0.01	**54.50**
	0.85	79.46	0.58	**136.17**	67.46	0.65	**103.61**	0.85	0.01	**102.08**

As expected, there was no significant difference between the ratio COVs (COV_r) estimated using the first and second noise subject's data ($p = 0.671$). This shows that the results are not an anomaly of a single subject's noise, but are a replicable phenomenon.

The COVs for the amplitudes (COV_c and COV_t) estimated using the SVD method were significantly greater than the amplitude COVs estimated using dipole modeling ($p < 0.001$ and $p < 0.001$, respectively). There was no significant difference between the ratio COVs (COV_r) estimated using the SVD method and dipole modeling ($p = 0.304$). The tables show that the COVs for the conditioning and testing responses are *much* improved over dipole modeling. The COVs for the ratio estimates are usually on the order of the COV of the testing amplitudes. The COVs for the ratios are generally a little larger than the dipole modeling ratio COVs, and is reflected in the trendy p-value ($p = 0.304$, as reported above).

Hypothesis testing reveals that the COVs for the conditioning amplitude (COV_c) is significantly larger than the COVs for the ratio (COV_r) ($p < 0.001$), and the COVs for the testing amplitude are generally a little larger than the COVs for the ratios, as reflected in the trendy ($p = 0.052$) p-value. These results (i.e., the estimated amplitude ratios are *more* variable than the estimated amplitude parameters) would be expected theoretically if the numerator and denominator of the ratio (i.e., the testing and conditioning amplitude estimates, respectively) were independent. The high ratio COVs estimated using the SVD method are therefore not due to the interdependence of the conditioning and testing amplitude estimates. Further research is necessary in order to evaluate the effect of multiple data channels and multiple time points on the variability of amplitude ratios estimated using the SVD method.

The COVs (COV_r, COV_c, and COV_t) significantly increased as the SNR was increased ($p < 0.001$, $p < 0.001$, and $p < 0.001$, respectively). The COVs for the testing amplitudes and the ratios (COV_t and COV_c) significantly increased as the C-T ratio increased ($p < 0.001$ and $p < 0.001$, respectively), but the COVs for the conditioning amplitudes (COV_c) were unaffected by increases in the C-T ratio ($p = 0.531$). In retrospect, the C-T ratio results make sense. When the data sets

were constructed, the different C-T ratios were achieved by altering the amplitude of the testing response while leaving the conditioning response amplitude constant. An examination of Tables 5.1-5.6 shows that $\bar{x}_c$ is very stable within each data set (i.e., within each table) as the C-T ratio is varied, and therefore no difference in COV_c estimated at different C-T ratios should be expected. It is important to realize that this was *not* the case for dipole modeling. When dipole modeling was used, estimation of data sets with different C-T ratios affected both the conditioning and testing amplitude estimates.

There were no significant differences between the ratio COVs (COV_r) estimated from data sets generated by centric vs. eccentric dipoles. The COV_r estimated using data generated by cortical dipoles (Data Sets 3 and 6) were not greater than the COV_r estimated using data generated by hippocampal (Data Sets 2 and 5) or thalamic (Data Sets 1 and 4) dipoles ($p = 0.419$ and $p = 0.198$, respectively). In addition, the COV_r estimated using data generated by hippocampal dipoles were not greater than the COV_r estimated using data generated by thalamic dipoles ($p = 0.257$). These results indicate that the SVD method works as well on centric generators as it does on eccentric generators.

The simulated data were generated by either a single dipole or synchronously active bilateral dipoles. For these data sets, the first singular value obtained from the SVD is *much* larger than the second singular value. The average ratio of the first and second singular values (sv_1/sv_2) from the first application of SVD (i.e., the SVD application that constrains all electrodes to have the same "shape" over time) was 12.75 for all high SNR data sets, and 5.71 for all low SNR data sets. The average ratio of the first and second singular values (sv'_1/sv'_2) from the second application of SVD (i.e., the SVD application that constrains all data sets to have the same topography over the scalp) was 31.37 for all high SNR data sets, and 19.11 for all low SNR data sets. The results show that (1) EEG noise affects the ability of SVD to find what is "common" between all columns (compare 12.75 to 5.71 and 31.37 to 19.11), and (2) EEG noise has a greater effect on the estimation of the common "shape" over time than on the estimation of the common "topography" over the scalp (compare 31.37 to 12.75 and 19.11 to 5.71).

I can conclude that the SVD is better than dipole modeling in terms of reliably estimating absolute amplitudes, and as good as dipole modeling in terms of reliably estimating amplitude ratios, when the data are generated by a single dipole or by two synchronously active dipoles. In the next section I applied the SVD method to the P50 data analyzed in Chapter 2.

5.4 Application to Real P50 Data

I applied the SVD method to the real P50 data analyzed in Chapter 2. In summary, the data from Chapter 2 consisted of 6 replications of P50 collected in a conditioning-testing paradigm for 12 normal hearing subjects. Data were collected from 14 scalp electrodes (see Figure 2.1). Similar to that chapter, I first bandpass filtered the averaged P50 data, then selected a time window within the average in order to analyze only the section of the average response where P50 was prominent. Because Chapter 2 had shown that subject 17 did not have a valid P50 response (and was not included in the dipole modeling reliability computation), subject 17 was not included in the SVD analysis, either. Chapter 2 had also shown that electrodes F7 and F8 were noisy and affected the dipole fit, and so were discarded from the dipole modeling analysis. Because of this, F7 and F8 were not included in the SVD analysis either.

When 12 electrode channels were included in the SVD analysis, the reliability of the C-T ratio estimated using the SVD method (as measured by the ICC on 11 subjects) was $r = 0.45$. As reported in Chapter 2, the reliability of the C-T ratio estimated using peak-picking on 11 subjects was $r = 0.37$. The average ratio of the first and second singular values (sv_1/sv_2) over all 66 data sets (11 subjects $\times$ 6 replications per subject) was 1.76. This singular value ratio is *much* lower than those obtained when the simulated data were analyzed, and its low value indicated that more than one singular value (and therefore more than one right- and left-hand singular vector) must be retained in order to approximate the original $\mathcal{H}$. This very low singular value ratio led me to suspect that time-locked activity overlapping P50 was present at some channels, which was problematic since the SVD method cannot

separate the P50 from other time-locked activity.

There are three types of electrical activity present in an evoked potential average: (1) electrical activity generated by the brain in response to the stimulus that is of interest to the experimenter ("signal"), (2) electrical activity generated by various sources (brain, muscle, amplifiers, etc.) that is not related to the stimulus ("noise"), (3) electrical activity generated by the brain in response to the stimulus that is not of interest to the experimenter ("unwanted signal"). The effect of noise can usually be reduced by better experimental methods (use of a fixation point to reduce eye movements, requiring the subject to keep their eyes open in order to reduce the presence of spontaneous alpha waves, etc.) and/or by averaging many single trials. Unwanted signal is more difficult, because it is time-locked to the stimulus and will not average out. If the unwanted signal is composed of different frequencies that the signal, filtering can reduce the effect of unwanted signal (i.e., bandpass digital filtering used in Chapter 2 reduced the contribution of N100 on the P50). The presence of unwanted signal in an EP average leads to poor performance of the SVD method, so I used prior knowledge of auditory P50 in order to eliminate channels with unwanted signal.

The channels which would most likely exhibit time-locked activity overlapping P50 were Fp1 and Fp2 (due to possible eye-movement contamination, [118]), and T3 and T4 (possible overlapping presence of Tp41, best recorded at T3 and T4, [119]). By eliminating the Fp1, Fp2, T3, and T4 electrodes, I was able to reliably estimate the C-T ratios using the SVD method. The ICC of the C-T ratio estimated using the SVD method on 8 electrode channels over 11 subjects was $r = 0.66$, as compared to $r = 0.63$ for the C-T ratio estimated using dipole modeling. Recall that the ICC of the C-T ratio estimated using peak picking (on 11 subjects) was $r = 0.37$.

The average ratio of the first and second singular values (sv_1/sv_2) over all 66 data sets using only 8 electrodes was 2.76. This is still lower than that obtained when the low SNR simulated data were analyzed (compare 2.76 to 5.71). In addition (borrowing a concept from principal components analysis), when using 8 electrodes, the quantity $sv_1^2/\sum_i^{16} sv_i^2$ was 0.78 (for principal components, this gives the proportion of variance explained by the first principal component–the SVD method has no such

statistical framework, but it is still a useful measure of the "strength" of the first singular vectors). When the SVD method was applied to the high and low SNR simulated data, the same quantity was 0.99 and 0.95, respectively. Although the increase in the ICC argues that the discrepancies in these quantities (0.99 or 0.95 vs. 0.78) between the real and simulated data is due to a lower SNR for the real data, further research is necessary in order to rule out the presence of time-locked overlapping activity in P50 recorded at these electrodes.

5.5 Discussion

The simulation results show that the SVD method reliably estimates amplitudes and amplitude ratios (i.e., high COVs). In addition, the SVD method accurately estimates amplitude ratios (nearly zero bias). The SVD method is superior to dipole modeling in terms of reliable estimation of amplitude, and is comparable to dipole modeling for reliable estimation of amplitude ratios. Because the SVD method is simpler and faster than dipole modeling, there is no reason to use dipole modeling when amplitudes and ratios are the only parameters of interest, and when the data are generated by a single dipole or multiple synchronous dipoles.

The SVD method is closely related to principal components analysis (PCA). Principal components analysis decomposes a square, positive-definite, symmetric matrix $\mathcal{X}$ into $\mathcal{Q}\mathcal{A}\mathcal{Q}^T$, where $\mathcal{Q}$ is an orthogonal square matrix with the same dimension as $\mathcal{X}$, and $\mathcal{A}$ is a diagonal square matrix with the same dimension as $\mathcal{X}$. The matrix $\mathcal{Q}$ is the matrix of eigenvectors of $\mathcal{X}$ (where the eigenvectors $\mathbf{Q}_1, \mathbf{Q}_2, \ldots, \mathbf{Q}_{2n}$ are the columns of $\mathcal{Q}$), and associated with each eigenvector is the eigenvalue λ_i^2, where λ_i are the elements along the diagonal of $\mathcal{A}$, arranged in decreasing order.

Principal components can be applied to a variety of square, positive definite symmetric matrices constructed from original EP data. As an example, consider the matrix of cross-correlations between the data waveforms. Given an original data matrix $\mathcal{H}$, with u rows (corresponding to u time points) and $2n$ columns (corresponding to two data sets recorded on n electrodes), let H_{ki} correspond to the element in the kth row and ith column of $\mathcal{H}$. Each element in the cross-correlation matrix is defined

as follows:

$$R_{ij} = \frac{1}{u} \sum_{k=1}^{u} H_{ki} H_{kj} \tag{5.2}$$

where R_{ij} is the cross-correlation between the ith and jth electrodes, computed over time. The matrix of cross-correlations $\mathcal{R}$ can be easily computed as

$$\mathcal{R} = \frac{1}{u} \mathcal{H}^T \mathcal{H} \tag{5.3}$$

For positive definite matrices the SVD matrix factorization is identical to $\mathcal{Q}\mathcal{\Lambda}\mathcal{Q}^T$, so SVD can be applied to matrix $\mathcal{R}$. The columns of $\mathcal{Q}$ are the principal component loadings, and describe how the columns of $\mathcal{H}$ (i.e., the original channels of data) are linearly combined to create the principal component scores. The principal component scores are given by $\mathcal{HQ}$. The first column of $\mathcal{HQ}$ corresponds to the principal component scores for the first principal component loading vector, and the value of $\lambda_i^2 / \sum_{k=1}^{2n} \lambda_k^2$ gives the proportion of variation explained by the ith principal component.

If only a single dipole generated the data, or if the data were generated by multiple dipoles simultaneously active with the same time-varying magnitude function, then only the first eigenvalue would be significant in the PCA analysis. The first column of $\mathcal{HQ}$ would be analogous to the first left-hand singular vector (when the SVD method is applied to $\mathcal{H}$), and the first eigenvector ($\mathbf{Q}_1$) would be analogous to the first right-hand singular vector. The first eigenvector ($\mathbf{Q}_1$) is of length $2n$, and can be arranged into an $n \times 2$ matrix $\mathcal{E}$, where the first column of $\mathcal{E}$ is composed of the first n elements of $\mathbf{Q}_1$, and the second column of $\mathcal{E}$ is composed of the second n elements of $\mathbf{Q}_1$. The matrix of cross-correlations of $\mathcal{E}$ can be computed and factored into $\mathcal{Q}'\mathcal{\Lambda}'\mathcal{Q}'^T$. The first principal component loading vector of $\mathcal{E}$ (i.e., $\mathcal{Q}'_1$) should contain the estimates of the covariate effects on amplitude analogous to those found using the SVD method, and the first diagonal element of $\mathcal{\Lambda}'$ should contain a common amplitude estimate for the original data. The diagonal elements of $\mathcal{\Lambda}'$ will not generally be the same as those of $\mathcal{W}'$ from the SVD method, but this is a scaling issue.

As described, PCA can be used to estimate amplitudes and amplitude ratios. Because PCA is only for square, positive definite symmetric matrices, the com-

putation of the matrix of cross-correlations (or some other pre-processing step for constructing a square, positive definite, symmetric matrix) is required in order to estimate the amplitudes and amplitude ratios using PCA. The SVD method can be used on the original, usually non-square matrices. This is a computational advantage. The SVD method is also simple and more intuitive (it is a simple decomposition of the original data matrix into its principal directions).

The SVD method is limited to certain types of problems, however. In this chapter, the SVD method was tested on single dipole simulated data, and on two dipole data where the two dipoles had the same amplitude, time-varying magnitude function, and amplitude ratio. It is not clear how the SVD method will perform on multiple dipole data sets where the dipoles do not share amplitudes, time-varying magnitude functions, or amplitude ratios. Because of the relationship between the SVD method and PCA, it is likely that the SVD method will be inappropriate for the same types of data sets on which PCA failed (i.e., multiple asynchronous generators overlapping in time). Until the SVD method is tested on such data sets, the SVD method can only be applied to a small number of evoked potentials. At this time the SVD method will be useful in studying short-latency exogenous evoked potentials where prior knowledge of anatomy ensures that the constraints are met.

For multiple dipole problems, it is likely that more than one singular value will be greater than zero. It is not clear how the SVD method would work if more than one singular value were retained. This is an avenue for further research.

The SVD amplitude ratios were slightly biased at the low SNR. When the SVD method is applied to real data, it will be important to use data collection and processing methods that will increase the SNR. For instance, it will be important to eye-movement correct data and monitor pre-stimulus EEG in order to reject relatively noisy trials.

The application of the SVD method to real auditory P50 showed that the inclusion of channels at which other time-locked activity was present severely degraded the performance of the method. The SVD method does not use a model for the common "shape" of the evoked potential (across electrodes) or for the common topographical distribution (over replications). The Dipole Components Model (DCM)

models both the shape and the topographical distribution. Because of this, the DCM can "separate" the signal from other electrical activity in the average. If the electrical activity (noise or unwanted signal) does not fit the model (over time *or* over space), the DCM can "weight" (i.e., discount the contributions of) the affected electrodes appropriately. The SVD method cannot separate signal from other electrical activity (especially not electrical activity correlated between electrode channels). Although better data collection and processing methods can help to decrease noise or to exclude noisy channels of data, it is a more difficult task to exclude electrodes because of the presence other time-locked activity. Reduction of both random noise and unwanted signal are required for successful application of the SVD method.

It may be possible to exclude channels that exhibit other time-locked activity if a template of the desired signal can be obtained (perhaps a very clean average of several thousand single trials). The template and each channel of data can be cross-correlated. A small value of the cross-correlation would indicate that the template and the data channel are not similar, other activity is present at that channel, and that that channel should be excluded. A large value of the cross-correlation indicates that the template and the data channel are a good match, and that channel should be included in the analysis. This method could be used to exclude partially overlapping time-locked activity. This method, however, would fail if the time-locked activity were completely overlapped and of the same shape (i.e. changing in the same way over time) as the signal of interest. In such a case, dipole modeling should still do better than the SVD method, because dipole modeling can enforce the topographical constraint, which can help to separate such overlapping activity from the signal of interest.

Using prior knowledge of the auditory P50, I was able to exclude channels that degraded performance of the SVD method. I excluded channels that previous investigators had shown to be artifacted (with eye movement or muscle activity), and channels that I knew were recommended for recording the earlier and overlapping Tp41 potential. I also knew that there was likely to be other brain activity at the same latency of auditory P50, simply because of the latency of the response. The primary auditory cortical response has not been recorded at the scalp, but probably

occurs within 15 ms of an auditory stimulus [40, 39]. By the latency of the auditory P50 (approximately 50 ms after the stimulus), many areas of the brain are likely to be responding in some way to the stimulus. Prior knowledge will not always be available, however, which limits the application of the SVD method.

As stated earler, the SVD method is only guaranteed to work if the data are generated by a single dipole or simultaneously active dipoles with the same time-varying activity. It is difficult to determine which evoked potentials fit into this special class. It may be possible to use dipole modeling on a subset of data in order to determine if a single dipole model fits the data well. If a single dipole model works, then it is likely that the SVD method can be used to analyze the rest of the data.

Prior knowledge of the distribution of the evoked potential should be used to decide what montage should be used to collect data if the SVD method is to be used. Unlike dipole modeling, where electrodes are placed all over the head (in an attempt to sample the topographical distribution), the SVD method will work best when only those electrodes with high SNR are included. For the SVD method, it makes more sense to cluster the electrodes where the potential of interest is best measured. Dipole modeling might also be useful for determining the best data collection montage when the SVD method will be used to analyze the data. Dipole modeling of the data can show where the electric field should be large. Electrodes can be clustered in this area, and large SNR recordings should be obtained.

The SVD method should be tested on other data sets, but this chapter shows that the SVD method is superior to dipole modeling for amplitude and ratio estimation, and can be used to reliably estimate the auditory P50 conditioning-testing ratio.

Chapter 6

Summary and Conclusions

This dissertation has shown several things: (1) dipole modeling can be used to increase the reliability of the auditory P50 conditioning-testing ratio over peak picking, (2) dipole modeling cannot presently be used to reliably estimate absolute amplitudes, (3) dipole model misspecification will not bias amplitude ratio measurements when a single dipole is active or when multiple dipoles are active with the same amplitude or amplitude ratio, (4) in the presence of model misspecification and noise, dipole modeling amplitude ratios are much less variable than absolute amplitudes (implying that amplitude ratios are more reliable than absolute amplitudes), and (5) the SVD method is superior to dipole modeling when only a single generator or synchronously active multiple generators are active, no other time-locked activity is present in the EP average, and amplitude and ratios are the only parameters of interest.

Chapter 2 showed that dipole modeling could be used to increase the reliability of the auditory P50 C-T ratio over peak picking. A control experiment in Chapter 2 indicated that the increase in reliability could not be attributed to the pooling of noise across multiple data sets. But because Chapter 2 also showed that dipole modeling led to unreliable conditioning and testing amplitude measurements, the increase in reliability apparently could not be attributed to the use of multiple channels of data. I proposed that the presence of model misspecification and noise influenced the reliability results.

Chapter 3 used the theory of least squares fitting to show that in certain cases, amplitude ratios estimated using the Dipole Components Model (DCM) were unbiased even when the dipole model was misspecified. The model misspecifications considered were head model, time-varying magnitude function, and number of dipoles. The cases in which these misspecifications had no effect on the ratios were: (1) single dipole active (no effect of head model or time-varying moment function misspecification on ratio estimation), (2) multiple dipoles active when all amplitudes are the same (no effect of head model, time-varying magnitude function, or number of dipoles misspecification on ratio estimation), and (3) multiple dipoles active when all amplitude *ratios* are the same across data sets (no effect of head model or time-varying magnitude function misspecification on ratio estimation).

Chapter 4 added noise to simulated data and investigated the performance of dipole modeling when both model misspecification and noise were present. The results of this chapter showed that amplitude ratios were more reliable amplitudes when estimated using dipole modeling. This chapter also showed that when noise was present in a misspecified model, the nonlinearly estimated dipole parameters were variable, possibly indicating that the global minimum "shifted" in the presence of noise. This observation suggested that the use of a noisy misspecified model was introducing variability into the estimated amplitudes, and led to the proposal of a SVD method for estimating amplitudes and ratios.

Chapter 5 proposed a model-free method using singular value decomposition (SVD) for estimating amplitudes and ratios, and tested the SVD method on the simulated data from Chapter 4. The SVD method performed well on the simulated data, and estimated reliable amplitudes and accurate and reliable ratios. The SVD method used multiple channels and no model, and the increase in reliability for the amplitudes over dipole modeling indicated that the noisy misspecified dipole model was introducing variability into the absolute amplitudes. When the SVD method was applied to the real auditory P50 data of Chapter 2, the reliability of the C-T ratios estimating using 12 channels of data was not increased over the peak-picking C-T ratio reliability. By using prior knowledge of the brain electrical activity at 50 ms and knowledge of the artifacts typically present in a P50 recording, I was able to

exclude electrodes that degraded the estimation of the covariate effects on amplitude. When only 8 channels of data were used to estimate the C-T ratio using the SVD method, an increase in reliability comparable to that of dipole modeling was achieved.

These results are impressive, but are only valid for restricted cases. As noted above, these results have so far only been shown for three special cases. Dipole modeling ratios will certainly be biased in most multiple dipole models, and the reliability of these ratio estimates has not yet been studied. It is unclear at this time if dipole modeling will lead to reliability increases for multiple dipole models. The SVD method has not been tested on most multiple dipole problems either, and at this time should only be applied to a limited number of evoked potentials.

Because of the limitations of both a misspecified dipole model and the SVD method in addressing multiple dipole problems, neither method can adequately deal with auditory C-T ratio estimation when P50 is overlapped with the preceding P30. At the present time, the only solution for dealing with P30/P50 overlap is to reduce the model misspecification in the dipole model (i.e., improved head shape model, improved time-varying magnitude functions, etc.).

All results in this dissertation are limited to estimation of covariate effects on amplitude. Estimation of covariate effects on latency is a more complicated problem, because latency parameters do not enter the estimation problem as a multiplicative variable. Latency parameters cannot be estimated using singular value decomposition, and enter into the dipole model as a nonlinear parameter. There are many evoked potential experiments in which latency changes are expected between subjects or experimental conditions, so reliable and accurate estimation of covariate effects on latency is important. Perhaps the SVD method can be part of a two-step process for estimating covariate effects on amplitude and latency. Some technique could be used to estimate latency effects and to subsequently "align" the data sets before SVD is used to estimate the the amplitude effects. This is an area for further research.

Another limitation of *both* the dipole model and the SVD method is the constraint that the time-varying magnitude function and the topography between channels must be *exactly* the same between data sets. This rigid constraint is somewhat unrealistic, especially if the data sets were collected from different subjects.

It would be more realistic if slight differences in the topography and time function were allowed, and the relaxation of these constraints may also lead to improved estimation. Such slight differences can be easily implemented using dipole modeling. Penalty functions were developed in Chapter 4 in order to enforce the bilateral constraint. Similar penalty functions can be developed in order to allow small variation in dipole location, orientation, and time-varying function between data sets. No penalty would be added if the dipole parameters were the same between data sets, a small penalty would be added for small differences in the parameters. The penalty would increase exponentially as the differences in location, orientation, and time function increased. Variation in the waveshape and topography across data sets is not allowed using the SVD method.

Because of the limitations of the SVD method, there may only be a few evoked potentials for which SVD can be used for unbiased ratio estimation. However, because ratio measurements are not common in most EP work, the SVD method may be more useful as a multiple channel, multiple time point amplitude estimation method. It is well known that peak-picking amplitude estimates are unreliable, largely because single time points at single channels are very sensitive to noise. The SVD method may be a way of measuring the amplitude over multiple channels and time points, and may be a way of reducing the effect of noise on amplitude measurements. The resultant amplitude would have no physical meaning, but would only be a number for comparison relative to other SVD-derived amplitudes.

Dipole modeling requires a large number of electrodes (it is generally accepted that at a minimum one channel of data is necessary for each nonlinear parameter estimated). The SVD method, on the other hand, has no such limitation. Theoretically, the SVD method can be used to measure amplitudes for two data sets using a single channel of data (the $\mathcal{H}$ matrix would be of dimension $u \times 2$, where u is the number of time points). This makes the SVD method attractive to clinicians, who typically do not have the time or equipment for measuring 16 or 32 channels of data. The SVD method could be a quick clinical test for measuring amplitudes on small (in terms of electrodes) data sets.

In summary, this dissertation has led to improved understanding of how

model misspecification and noise affect the bias and variance of dipole modeling estimates. In addition, this dissertation proposes a new SVD method which promises to simplify and improve the analysis of short-latency, exogenous evoked potentials.

Bibliography

[1] R.N. Kavanagh, T.M. Darcey, D. Lehmann, and D. Fender. Evaluation of methods for three-dimensional localization of electrical sources in the human brain. *IEEE Transactions on Biomedical Engineering*, BME-25(5):421–429, 1978.

[2] A. Achim, F. Richer, and J.M. Saint-Hilaire. Methods for separating temporally overlapping sources of neuroelectric data. *Brain Topography*, 1(1):22–28, 1988.

[3] J.C. De Munck. The estimation of time varying dipole on the basis of evoked potentials. *Electroencephalography and Clinical Neurophysiology*, 77:156–160, 1990.

[4] B. He, T. Musha, Y. Okamoto, S. Homma, Y. Nakajima, and T. Sato. Electric dipole tracing in the brain by means of the boundary element method and its accuracy. *IEEE Transactions on Biomedical Engineering*, BME-34(6):406–414, 1987.

[5] C.J. Henderson, S.R. Butler, and A. Glass. The localization of equivalent dipoles of EEG sources by the application of electrical field theory. *Electroencephalography and Clinical Neurophysiology*, 39:117–130, 1975.

[6] S. Homma, Y. Nakajima, T. Musha, Y. Okamoto, and B. He. Dipole-tracing method applied to human brain potentials. *Journal of Neuroscience Methods*, 21:195–200, 1987.

[7] M. Scherg and D. Von Cramon. Evoked dipole source potentials of the human auditory cortex. *Electroencephalography and Clinical Neurophysiology*, 65:344–360, 1986.

[8] M.R. Schneider. A multistage process for computing virtual dipolar sources of EEG discharges from surface information. *IEEE Transactions on Biomedical Engineering*, BME-19(1):1–12, 1972.

[9] R.D. Sidman, V. Giambalvo, R. Allison, and P. Bergey. A method for localization of sources of human cerebral potentials evoked by sensory stimuli. *Sensory Processes*, 2:116–129, 1978.

[10] B. Turetsky, J. Raz, and G. Fein. Representation of multi-channel evoked potential data using a dipole components model of intracranial generators: application to the auditory P300. *Electroencephalography and Clinical Neurophysiology*, 76:540–556, 1990.

[11] J.P. Ary, S.A. Klein, and D.H. Fender. Location of sources of evoked scalp potentials: Corrections for skull and scalp thicknesses. *IEEE Transactions on Biomedical Engineering*, BME-28(6):447–452, 1981.

[12] B. He and T. Musha. Effects of cavities on EEG dipole localization and their relations with surface electrode positions. *International Journal of Biomedical Computing*, 24(4):269–282, 1989.

[13] T. Musha and S. Homma. Do optimal dipoles obtained by the dipole tracing method always suggest true source locations? *Brain Topography*, 3(1):143–150, 1990.

[14] D. Fletcher, D. Jewett, Z. Zhang, and A. Amir. The effect of skull shape on single and multiple dipole source localizations. In *Proceedings of the 15th Annual International Conference of the IEEE Engineering in Medicine and Biology Society*, pages 1469–1470, 1993.

[15] Z. Zhang and D.L. Jewett. Insidious errors in dipole localization parameters at a single time-point due to model misspecification of number of shells. *Electroencephalography and Clinical Neurophysiology*, 88:1–11, 1993.

[16] H. Davis, T. Mast, M. Yoshie, and S. Zerlin. The slow response of the human cortex to auditory stimuli: recovery process. *Electroencephalography and Clinical Neurophysiology*, 21:105–113, 1966.

[17] H. Fruhstorfer, P. Soveri, and T. Jarvilehto. Short-term habituation of auditory evoked response in man. *Electroencephalography and Clinical Neurophysiology*, 28:153–161, 1970.

[18] R. Freedman, L.E. Adler, M.C. Waldo, E. Pachtman, and R. Franks. Neurophysiological evidence for a defect in inhibitory pathways in schizophrenia: comparison of medicated and drug-free patients. *Biological Psychiatry*, 18:537–551, 1983.

[19] R. Freedman, L.E. Adler, G.A. Gerhardt, M. Waldo, N. Baker, G.M. Rose, C. Drebing, H. Nagamoto, P. Bickford-Wimer, and R. Franks. Neurobiological studies of sensory gating in schizophrenia. *Schizophrenia Bulletin*, 13:669–678, 1987.

[20] R. Freedman, L.E. Adler, and M. Waldo. Gating of the auditory evoked potential in children and adults. *Psychophysiology*, 24(2):223–227, 1987.

[21] L.E. Adler, K. Pang, G. Gerhardt, and G.M. Rose. Modulation of the gating of auditory evoked potentials by norepinephrine: pharmacological evidence obtained using a selective neurotoxin. *Biological Psychiatry*, 24:179–190, 1988.

[22] L.E. Adler, G.A. Gerhardt, R. Franks, N. Baker, H. Nagamoto, C. Drebing, and R. Freedman. Sensory physiology and catecholamines in schizophrenia and mania. *Psychiatry Research*, 31:297–309, 1990.

[23] N.N. Boutros, J. Overall, and B. Zouridakis. Test-retest reliability of the P50 mid-latency auditory evoked response. *Psychiatry Research*, 29:181–192, 1991.

[24] N. Kathmann and R.R. Engel. Sensory gating in normals and schizophrenics: a failure to find strong P50 suppression in normals. *Biological Psychiatry*, 27:1216–1226, 1990.

[25] D.L. Jewett and J.S. Williston. Auditory evoked far-fields averaged from the scalp in humans. *Brain*, 94:681–696, 1971.

[26] J.E. Desmedt and G. Cheron. Central somatosensory conduction in man: neural generators and interpeak latencies of the far-field components recorded from neck and right or left scalp and earlobes. *Electroencephalography and Clinical Neurophysiology*, 50:382–403, 1980.

[27] I. Hashimoto. Somatosensory evoked potentials from the human brain-stem: origins of short latency potentials. *Electroencephalography and Clinical Neurophysiology*, 57:221–227, 1984.

[28] J.E. Desmedt and G. Cheron. Non-cephalic reference recording of early somatosensory potentials to finger stimulation in adult or aging normal man: differentiation of widespread N18 and contralateral N20 from the prerolandic P22 and N30 components. *Electroencephalography and Clinical Neurophysiology*, 52:553–570, 1981.

[29] T. Allison, G. McCarthy, C.C. Wood, T.M. Darcey, Spencer D.D., and P.D. Williamson. Human cortical potentials evoked by stimulation of the median nerve. I. cytoarchitectonic areas generating short-latency activity. *Journal of Neurophysiology*, 62(3):694–710, 1989.

[30] S.A. Hillyard and T.W. Picton. Electrophysiology of cognition. In J.M. Brookhart and V.B. Mountcastle, editors, *The Nervous System*, volume 5 of *Handbook of Physiology*, pages 519–584. Williams & Wilkins, Baltimore, MD, 1987.

[31] R. Spehlmann. *Evoked Potential primer: Visual, auditory, and somatosensory evoked potentials in clinical diagnosis.* Butterworth, Boston, 1985.

[32] K. Chiappa. *Evoked Potentials in Clinical Medicine.* Raven Press, New York, second edition, 1990.

[33] C.D. Yingling and J.N. Gardi. Intraoperative monitoring of facial and cochlear nerves during acoustic neuroma surgery. *Otolaryngologic Clinics of North America*, 25:413–448, 1992.

[34] J.B. Green, L. Flagg, D.M. Freed, and J.D. Schwankhaus. The middle latency auditory evoked potentials may be abnormal in dementia. *Neurology*, 42(May):1034–1036, 1992.

[35] D.M. Psatta and M. Matei. Incidence of brain stem auditory evoked potential amplitude disorders in oto-neurologic pathology. *Rev Roum Med Neurol Psychiat*, 25:145–160, 1987.

[36] A. Starr and L.J. Achor. Auditory brain stem responses in neurological disease. *Archives of Neurology*, 32:761–768, 1975.

[37] M.C. Waldo, L.E. Adler, and R. Freedman. Defects in auditory sensory gating and their apparent compensation in relatives of schizophrenics. *Schizophrenia Research*, 1:19–24, 1988.

[38] G.E. Chatrian, M.C. Petersen, and J.A. Lazarte. Responses to clicks from the human brain: some depth electrographic observations. *Electroencephalography and Clinical Neurophysiology*, 12:479–489, 1960.

[39] G.G. Celesia. Organization of auditory cortical areas in man. *Brain*, 99:403–414, 1976.

[40] W.R. Goff, T. Allison, W. Lyons, T.C. Fisher, and R. Conte. Origins of short latency auditory evoked potentials in man. In JE Desmedt, editor, *Auditory Evoked Potentials in Man. Psychopharmacology Correlates of EPs*, volume 2, pages 30–44. Karger, Basel, 1977.

[41] C.C. Wood, D.D. Spencer, T. Allison, G. McCarthy, P.D. Williamson, and W.R. Goff. Localization of human sensorimotor cortex during surgery by cortical

surface recording of somatosensory evoked potentials. *Journal of Neurosurgery*, 68:99–111, 1988.

[42] T. Allison, G. McCarthy, C.C. Wood, P.D. Williamson, and D.D. Spencer. Human cortical potentials evoked by stimulation of the median nerve. II. cytoarchitectonic areas generating long-latency activity. *Journal of Neurophysiology*, 62(3):711–721, 1989.

[43] B. Crespi, A. Mandelli, and G. Minoli. Short-latency somatosensory-evoked potentials in patients with acute focal vascular lesions of the supratentorial somesthesic pathways. *Acta Neurologica Scandinavia*, 65:274–279, 1982.

[44] B. Jabbari, S.C. Vance, M.G. Harper, A.M. Salazar, M.A. Smutok, and D. Amin. Clinical and radiological correlates of somatosensory evoked potentials in the late phase of head injury: a study of 500 vietnam veterans. *Electroencephalography and Clinical Neurophysiology*, 67:289–297, 1987.

[45] P. Kileny, D. Paccioretti, and A.F. Wilson. Effects of cortical lesions on middle-latency auditory evoked responses (MLR). *Electroencephalography and Clinical Neurophysiology*, 66:108–120, 1987.

[46] D.L. Woods, C.C. Clayworth, R.T. Knight, G.V. Simpson, and M.A. Naeser. Generators of middle- and long-latency auditory evoked potentials: implications from studies of patients with bitemporal lesions. *Electroencephalography and Clinical Neurophysiology*, 68:132–148, 1987.

[47] R.T. Knight, D. Scabini, D.L. Woods, and C. Clayworth. The effects of lesions of superior temporal gyrus and inferior parietal lobe on temporal and vertex components of the human aep. *Electroencephalography and Clinical Neurophysiology*, 70:499–509, 1988.

[48] J.E. Desmedt, T.H. Nguyen, and M. Bourguet. Bit-mapped color imaging of human evoked potentials with reference to the N20, P27 and N30 somatosensory responses. *Electroencephalography and Clinical Neurophysiology*, 68:1–19, 1987.

[49] M. Reite, P. Teale, J. Zimmerman, K. Davis, and J. Whalen. Source location of a 50 msec latency auditory evoked field component. *Electroencephalography and Clinical Neurophysiology*, 70:490–498, 1988.

[50] M.P. Deiber, V. Ibañez, C. Fischer, F. Perrin, and F. Mauguière. Sequential mapping favours the hypothesis of distinct generators for Na and Pa middle latency auditory evoked potentials. *Electroencephalography and Clinical Neurophysiology*, 71:187–197, 1988.

[51] M. Scherg and D. Von Cramon. A new interpretation of the generators of BAEP wave I-V: Results of a spatio-temporal dipole model. *Electroencephalography and Clinical Neurophysiology*, 62:290–299, 1985.

[52] J. Raz, B. Turetsky, and G. Fein. Frequency domain estimation of the parameters of human brain electrical dipoles. *Journal of the American Statistical Association*, 87(1):69–77, 1992.

[53] D.F. Stegeman, A. Van Oosterom, and E.J. Colon. Far-field evoked potential components induced by a propagating generator: computational evidence. *Electroencephalography and Clinical Neurophysiology*, 67:176–187, 1987.

[54] D.L. Deupree and D.L. Jewett. Far-field potentials due to action potentials traversing curved nerves, reaching cut nerve ends, and crossing boundaries between cylindrical volumes. *Electroencephalography and Clinical Neurophysiology*, 70:355–362, 1988.

[55] D.L. Jewett and D.L. Deupree. Far-field potentials recorded from action potentials and from a tripole in a hemicylindrical volume. *Electroencephalography and Clinical Neurophysiology*, 72:439–449, 1989.

[56] D.L. Jewett, D.L. Deupree, and D. Bommannan. Far-field potentials generated by action potentials of isolated frog sciatic nerves in a spherical volume. *Electroencephalography and Clinical Neurophysiology*, 75:105–117, 1990.

[57] C.C. Wood. Generators of evoked potentials. In SR Butler AM Halliday and R Paul, editors, *A Textbook of Clinical Neurophysiology.* Wiley and Sons, 1987.

[58] P.L. Nunez. *Electric Fields of the Brain.* Oxford University Press, New York, 1981.

[59] B. Rockstroh, T. Elbert, A. Canavan, W. Lutzenberger, and N. Birbaumer. *Slow Cortical Potentials and Behaviour.* Urban and Schwarzenberg, Baltimore, 1989.

[60] R. Plonsey. The active fiber in a volume conductor. *IEEE Transactions on Biomedical Engineering*, 21:371–381, 1974.

[61] R.P. Feynman, R.B. Leighton, and M. Sands. *The Feynman lectures on physics.* Addison-Wesley, Reading, MA, 1963-65.

[62] D.A. Brody, F.H. Terry, and R.E. Ideker. Eccentric dipole in a spherical medium: generalized expression for surface potenials. *IEEE Transactions on Biomedical Engineering*, BME-20:141–143, 1973.

[63] M. Scherg. Fundamentals of dipole source potential analysis. In M. Hoke F. Grandori and G.L. Romani, editors, *Auditory Evoked Magnetic Fields and Potentials*, volume 6, pages 40–69. Karger, Basel, 1990.

[64] J. Raz, C. Biggins, B. Turetsky, and G. Fein. Frequency domain dipole localization: Extensions of the method and applications to auditory and visual evoked potentials. *IEEE Transactions on Biomedical Engineering*, 40(9):909–918, 1993.

[65] J. Raz, V. Cardenas, and D. Fletcher. Frequency domain estimation of covariate effects in multichannel brain evoked potential data. *Biometrics*, in press, 1994.

[66] W.H. Press, S.A. Teukolsky, W.T. Vetterling, and B.P. Flannery. *Numerical Recipes in C: The Art of Scientific Computing.* Cambridge University Press, New York, NY, second edition, 1992.

[67] J.J. Dongarra. *LINPACK User's Guide.* Society for Industrial and Applied Mathematics, Philadelphia, 1979.

[68] IMSL Library Reference Manual. IMSL Inc., Houston TX, eighth edition, 1980.

[69] NAG Fortran Library Manual Mark 15. NAG Central Office, Downers Grove IL, 1991.

[70] T. Oostendorp and A. van Oosterom. Decoupling linear and non-linear parameters in bioelectric source estimation. In *Proceedings of the 15th Annual International Conference of the IEEE Engineering in Medicine and Biology Society*, pages 1478–1479, 1993.

[71] D.H. Fender. Source localization of brain electrical activity. In A.S. Gevins and A. Rèmond, editors, *Methods of Analysis of Brain Electrical and Magnetic Signals*, volume 1, pages 355–403. Elsevier Science Publisher B.V. (Biomedical Division), revised series edition, 1987.

[72] M. Scherg and T.W. Picton. Separation and identification of event-related potential components by brain electric source analysis. *Electroencephalography and Clinical Neurophysiology*, Suppl. 1991(42):24–37, 1991.

[73] J. Gerson, V. Cardenas, and G. Fein. Equivalent dipole parameter estimation using simulated annealing. *Electroencephalography and Clinical Neurophysiology*, 92:161–168, 1994.

[74] J.A. Nelder and R. Mead. A simplex method for function minimization. *Computer Journal*, 7:308–313, 1965.

[75] S. Kirkpatrick, C.D. Gelatt, Jr., and M.P. Vecchi. Optimization by simulated annealing. *Science*, 220(4598):671–680, 1983.

[76] S. Geman and D. Geman. Stochastic relaxation, Gibbs distribution, and the Bayesian restoration of images. *IEEE Transactions on Pattern Analysis and Machine Intelligence*, 6(6):721–741, 1984.

[77] A. Corana, M. Marchesi, C. Martini, and S. Ridella. Minimizing multimodal functions of continuous variables with the "simulated annealing" algorithm. *ACM Transactions on Mathematical Software*, 3(13):262–280, 1987.

[78] B. Kosko. *Neural Networks for Signal Processing.* Prentiss Hall, Englewood Cliffs, NJ, 1992.

[79] N. Metropolis, A. Rosenbluth, M. Rosenbluth, A. Teller, and E. Teller. Equations of state calculations by fast computing machines. *Journal of Chemical Physics*, 21:1087–1092, 1953.

[80] E. Donchin. A multivariate approach to the analysis of average evoked potentials. *IEEE Transactions on Biomedical Engineering*, BME-13:131–139, 1966.

[81] J.E. Jackson. *A User's Guide to Principal Components.* John Wiley & Sons, Inc., New York, 1991.

[82] C.C. Wood and G. McCarthy. Principal component analysis of event-related potentials: Simulation studies demonstrate misallocation of variance across components. *Electroencephalography and Clinical Neurophysiology*, 59:249–260, 1984.

[83] J. Möcks and R. Verleger. Principal component analysis of event-related potentials: A note on misallocation of variance. *Electroencephalography and Clinical Neurophysiology*, 65:393–398, 1986.

[84] J. Cohen and P. Cohen. *Applied Multiple Regression/Correlation Analysis for the Behavioral Sciences.* Lawrence Erlbaum Associates, Publishers, Hillsdale, NJ, second edition, 1983.

[85] P. Shrout and J. Fleiss. Intraclass correlation: uses in assessing rater reliability. *Psychological Bulletin*, 86:420–428, 1979.

[86] J.L. Palmer and L. Broemeling. A comparison of Bayes and maximum likelihood estimation of the intraclass correlation coefficient. *Commun. Statist.-Theory Meth.*, 19:953–975, 1990.

[87] A. Donner and M. Eliasziw. Sample size requirements for reliability studies. *Statistics in Medicine*, 6:441–448, 1987.

[88] R. Erwin and J.S. Buchwald. Midlatency auditory evoked responses: differential effects of sleep in the human. *Electroencephalography and Clinical Neurophysiology*, 65:383–392, 1986.

[89] R.J. Erwin and J.S. Buchwald. Midlatency auditory evoked responses: differential recovery cycle characteristics. *Electroencephalography and Clinical Neurophysiology*, 64:417–423, 1986.

[90] H.T. Nagamoto, L.E. Adler, M.C. Waldo, and R. Freedman. Sensory gating in schizophrenics and normal controls: Effects of changing stimulation interval. *Biological Psychiatry*, 25:549–561, 1989.

[91] M.C. Waldo and R. Freedman. Gating of auditory evoked responses in normal college students. *Psychiatry Research*, 19:223–239, 1986.

[92] R.C. Geary. The frequency distribution of the quotient of two normal variates. *Journal of the Royal Statistical Society*, 93:442–446, 1930.

[93] G. Marsaglia. Ratios of normal variables and ratios of sums of uniform variables. *Journal of the American Statistical Association*, 60:193–204, 1965.

[94] M. Kendall and A. Stuart. *The Advanced Theory of Statistics.* Macmillan, New York, NY, fourth edition, 1977.

[95] T. Sand. Statistical properties of ABR amplitudes and latencies. *Scand Audiol*, 19:131–137, 1990.

[96] K. Jerger, C. Biggins, and G. Fein. P50 suppression is not affected by attentional manipulation. *Biological Psychiatry*, 31:365–377, 1992.

[97] T. Suzuki, M. Hirabayashi, and K. Kobayashi. Effects of analog and digital filtering on auditory middle latency responses in adults and young children. *Ann Otol Rhinol Laryngol*, 93:267–270, 1984.

[98] M. Scherg and P. Berg. Use of prior knowledge in brain electromagnetic source analysis. *Brain Topography*, 4:143–150, 1991.

[99] T. Yokoyama, H. Ryu, K. Uemura, T. Miuamaoto, and Y. Imamura. Study of the constant wave form of ML-AEP in humans. *Electroencephalography and Clinical Neurophysiology*, 67:372–378, 1987.

[100] H.T. Nagamoto, L.E. Adler, M.C. Waldo, J. Griffith, and R. Freedman. Gating of auditory response in schizophrenics and normal controls: Effects of recording site and stimulation interval on the P50 wave. *Schizophrenia Research*, 4:31–40, 1991.

[101] N. Boutros, T. Rustin, and G. Zouridakis. Cocaine use and the P50 auditory evoked response. In *Proceedings of the Society of Biological Psychiatry*, pages 346–347, San Francisco, CA, 1993.

[102] L.E. Adler, L.J. Hoffer, J. Griffith, M.C. Waldo, and R. Freedman. Normalization by nicotine of deficient auditory sensory gating in the relatives of schizophrenics. *Biological Psychiatry*, 32(7):607–616, 1992.

[103] L.E. Adler, L.D. Hoffer, A. Wiser, and R. Freedman. Normalization of auditory physiology by cigarette smoking in schizophrenic patients. *American Journal of Psychiatry*, 150:1856–1861, 1993.

[104] G. Strang. *Linear Algebra and its Applications.* Harcourt, Brace, Jovanovich, San Diego, third edition, 1988.

[105] V. Cardenas, J. Gerson, and G. Fein. The reliability of P50 suppression as measured by the conditioning/testing ratio is vastly improved by dipole modeling. *Biological Psychiatry*, 33(5):335–344, 1993.

[106] R.V. Hogg and E.A. Tanis. *Probability and Statistical Inference.* Macmillan Publishing Company, New York, NY, third edition, 1988.

[107] V.V. Khlobystov and V.K. Zadiraka. Distribution density of scalar product of gaussian vectors. *Cybernetics*, 8:477–481, 1972.

[108] J. Spanier and K.B. Oldham. *An Atlas of Functions.* Hemisphere Publishing Corporation, Washington, 1987.

[109] N.L. Johnson and S. Kotz. *Distributions in Statistics: Continuous Univariate Distributions-2.* Houghton Mifflin Company, Boston, 1970.

[110] L.E. Adler and M.C. Waldo. Counterpoint: A sensory gating-hippocampal model of schizophrenia. *Schizophrenia Bulletin*, 17(1):19–24, 1991.

[111] J.S. Buchwald, C. Hinman, R.J. Norman, C.M. Huang, and K.A. Brown. Middle- and long-latency auditory evoked responses recorded from the vertex of normal and chronically lesioned cats. *Brain Research*, 205:91–109, 1981.

[112] J.S. Buchwald, E.H. Rubinstein, J. Schwafel, and R.J. Strandburg. Midlatency auditory evoked responses: Differential effects of a cholinergic agonist and antagonist. *Electroencephalography and Clinical Neurophysiology*, 80:303–309, 1991.

[113] M. Scherg, R. Hari, and M. Hämäläinen. Frequency-specific sources of the auditory N19-P30-P50 response detected by a multiple source analysis of evoked magnetic fields and potentials. In S.J. Williamson, editor, *Advances in Biomagnetism.* Plenum Press, New York, New York, 1989.

[114] G. Schaltenbrand and W. Wahren. *Atlas for stereotaxy of the human brain, with an accompanying guide.* G. Thieme, Stuttgart, 2nd edition, 1991.

[115] C.A. Brebbia and J. Dominguez. *Boundary Elements: An Introductory Course.* McGraw-Hill, New York, 1989.

[116] J. Raz, B. Turetsky, and G. Fein. Confidence intervals for the signal-to-noise ratio when a signal embedded in noise is observed over repeated trials. *IEEE Transactions on Biomedical Engineering*, 35(8):646–649, 1988.

[117] S. Shott. *Statistics for Health Professionals.* W.B. Saunders Company, Philadelphia, 1990.

[118] T. Gasser, L. Sroka, and J. Möcks. The transfer of EOG activity into the EEG for eyes open and closed. *Electroencephalography and Clinical Neurophysiology*, 61:181–193, 1985.

[119] M.M. Cohen. Coronal topography of the middle latency auditory evoked potentials (MLAEPs) in man. *Electroencephalography and Clinical Neurophysiology*, 53:231–236, 1982.